ACCSCIENCE PUBLISHING

Advances in

Radiotherapy & Nuclear Medicine

ISSN: 3060-8554 (Print)
ISSN: 2972-4392 (Online)
Volume 1 · Issue 2
October 2023

ACCSCIENCE PUBLISHING

Advances in Radiotherapy & Nuclear Medicine

Print ISSN: 3060-8554
Online ISSN: 2972-4392

Advances in Radiotherapy & Nuclear Medicine is a peer-reviewed and open-access journal that aims to publish and disseminate novel research in the breadth of radiation oncology, physics, and biology.

The journal aims to advance our understanding in the radiotherapy and provide a platform to oncologists and physicians to showcase their findings in original fundamental and clinical research as well as to present new ideas that highlight the changes in the radiation oncological clinical practice.

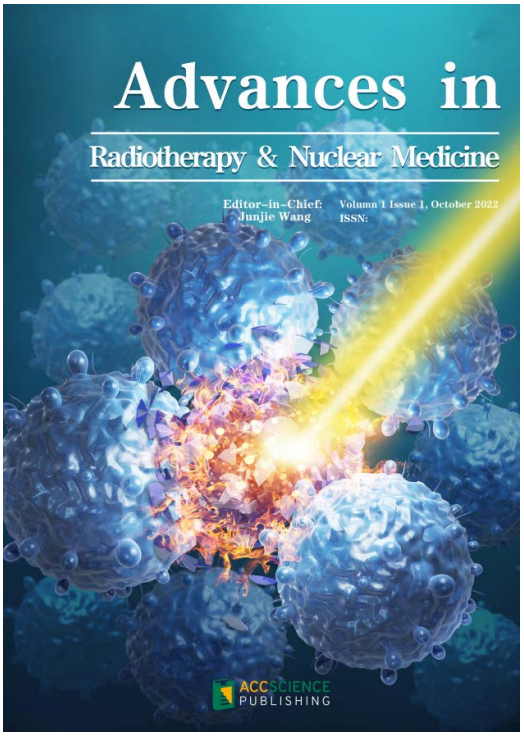

About the Publisher

AccScience Publishing is a publishing company based in Singapore. We publish a range of high-quality, open-access, peer-reviewed journals and books from a broad spectrum of disciplines.

Contact Us

Managing Editor
arnm.office@accscience.sg

AccScience Publishing
8 Burn Road, #15-03 Trivex, Singapore 369977.

Volume 1 • Issue 2 • October 2023
ISSN 3060-8554 (print) ISSN 2972-4392 (online)

Advances in Radiotherapy & Nuclear Medicine

ACCSCIENCE PUBLISHING

Access Science Without Barriers

ADVANCES IN RADIOTHERAPY & NUCLEAR MEDICINE

ISSN: 3060-8554 (print)
ISSN: 2972-4392 (online)

Editorial and Production Credits

Publisher: AccScience Publishing
Managing Editor: Freda Wang
Production Editor: Ian Wong
Journal Development Editor: Felicia Wang
Special Issue Commissioning Editor: Felicia Wang
Article Layout and Typeset: Sinjore Technologies (India)

For all advertising queries, contact arnm.office@accscience.sg.

Supplementary file

Supplementary files of articles can be obtained at https://accscience.com/journal/ARNM/1/2.

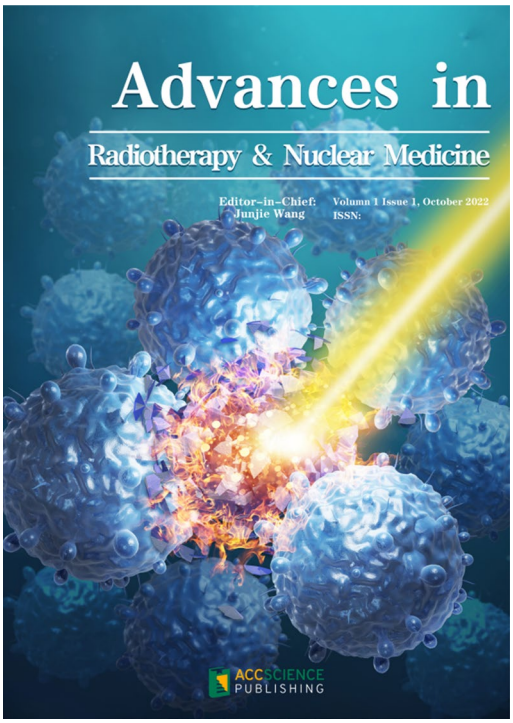

Advances in Radiotherapy & Nuclear Medicine

Editorial Board

ACCSCIENCE PUBLISHING

Volume 1 | Issue 2 | October 2023 |

Advances in Radiotherapy & Nuclear Medicine

https://accscience.com/journal/ARNM

CONTENTS

ACCSCIENCE PUBLISHING

Advances in Radiotherapy & Nuclear Medicine

EDITORIAL

Advances in Radiotherapy and Nuclear Medicine (*ARNM*): Leading the charge in oncological innovation

Tsair-Fwu Lee[1,2,3]*

[1]Medical Physics and Informatics Laboratory of Electronics Engineering, National Kaohsiung University of Science and Technology, Kaohsiung, Taiwan

[2]Graduate Institute of Clinical Medicine, Kaohsiung Medical University, Kaohsiung, Taiwan

[3]Department of Medical Imaging and Radiological Sciences, Kaohsiung Medical University, Kaohsiung, Taiwan

An excellent journal focusing on cancer topics is an instrumental element in enhancing innovation in cancer research. Given the dynamic landscape of cancer treatment, the *Advances in Radiotherapy & Nuclear Medicine (ARNM)* provides an indispensable resource, steering the course of research and clinical practices in radiation oncology, physics, and biology. This peer-reviewed, open-access journal transcends its role as a mere repository of knowledge; instead, it acts as a pioneering force propelling the medical community toward groundbreaking discoveries and innovative treatments in the relentless battle against cancer.

In alignment with our goal of bridging the chasm between research and clinical application, *ARNM* is unmatched in its commitment to advancing our understanding of radiotherapy. It functions as a critical platform for oncologists, physicians, and researchers, creating an ecosystem where novel ideas and research findings in both fundamental and clinical research are not merely shared but rigorously scrutinized and honed. This melding of theory with practice is vital for translating complex research into tangible, patient-centric benefits.

ARNM has a comprehensive and multifaceted scope, encompassing a wide array of radiation oncology topics:

(i) Conventional radiotherapy: The journal highlights advancements in traditional radiotherapy, affirming its ongoing relevance in modern clinical practice.

(ii) Stereotactic body radiation therapy and brachytherapy: *ARNM* delves deeply into these targeted therapy forms, emblematic of precision in cancer treatment[1].

(iii) Boron neutron capture therapy and particle therapy: The journal explores these innovative treatments, showcasing their potential to provide more effective, less invasive options for patients[2].

(iv) Targeted and immunotherapy (TI): By discussing the latest developments in TI, *ARNM* emphasizes the critical role of personalized medicine in oncology.

(v) Combined modality therapy (CMT): The journal's coverage of CMT, including heat therapy, electric field therapy, and nursing technology, reflects its dedication to holistic treatment approaches[3].

(vi) Radiation biology and radiation physics: *ARNM* offers fundamental insights into underlying principles of radiotherapy, essential for fostering innovation.

(vii) Innovative radiation technology, positron emission tomography, radiopharmaceuticals, and single-photon emission computed tomography: The journal remains at the vanguard of technological advancements, providing crucial insights into these progressive techniques[4].

***Corresponding author:**
Tsair-Fwu Lee
(tflee@nkust.edu.tw)

Citation: Lee T, 2023, *Advances in Radiotherapy and Nuclear Medicine* (*ARNM*): Leading the charge in oncological innovation. *Adv Radiother Nucl Med,* 1(2): 2615
https://doi.org/10.36922/arnm.2615

Received: January 2, 2024

Published Online: January 10, 2024

(viii) Molecular imaging and radionuclide therapy (MI & RT): *ARNM*'s focus on MI & RT opens new realms in understanding and combating cancer at the molecular level[5].

To expand our readership, we will continue to diversify the scope of *ARNM* and publish research and review articles in various relevant fields. These esteemed works include clinical radiotherapy, combined modality treatment, translational studies, epidemiological outcomes, imaging, dosimetry, and radiation therapy planning. Moreover, the journal extends its scope to experimental work in radiobiology, chemobiology, hyperthermia, tumor biology, data science in radiation oncology, and the physics aspects pertinent to oncology. This diverse content ensures that ARNM covers a vast spectrum of interest areas in radiation oncology, offering readers a holistic view of the field.

It is our aim to establish *ARNM* as an impetus behind the impending change in clinical practice: *ARNM* is more than just a journal; it is a catalyst for transformation, consistently introducing new ideas and perspectives that revolutionize radiation oncological clinical practice. Its dedication to disseminating novel research empowers professionals to stay at the forefront of the field, ensuring that patient care is always informed by the latest and most efficacious strategies.

ARNM stands as a budding testament to the unyielding pursuit of excellence in oncological care. Its influential role in shaping the future of cancer treatment is undeniable, offering hope and new horizons in the journey toward conquering cancer. As *ARNM* continues to illuminate the path forward, it reaffirms the medical community's dedication to saving lives and improving the quality of life for cancer patients worldwide.

With its extensive coverage and commitment to innovation, *ARNM* not only educates but also inspires the medical community. It serves as a vital tool for professionals looking to expand their knowledge and improve patient outcomes in the rapidly evolving field of cancer treatment.

Conflict of interest

The author declares no conflict of interest.

References

1. Levin-Epstein R, Cook RR, Wong JK, *et al.*, 2020, Prostate-specific antigen kinetics and biochemical control following stereotactic body radiation therapy, high dose rate brachytherapy, and low dose rate brachytherapy: A multi-institutional analysis of 3502 patients. *Radiother Oncol*, 151: 26–32.

   https://doi.org/10.1016/j.radonc.2020.07.014

2. Qi P, Chen Q, Tu D, *et al.*, 2020, The potential role of borophene as a radiosensitizer in boron neutron capture therapy (BNCT) and particle therapy (PT). *Biomater Sci*, 8: 2778–2785.

   https://doi.org/10.1039/D0BM00318B

3. Jhawar SR, Rivera-Núñez Z, Drachtman R, *et al.*, 2019, Association of combined modality therapy vs chemotherapy alone with overall survival in early-stage pediatric Hodgkin lymphoma. *JAMA Oncol*, 5: 689–695.

   https://doi.org/10.1001/jamaoncol.2018.5911

4. Sachpekidis C, Goldschmidt H, Dimitrakopoulou-Strauss A, 2019, Positron emission tomography (PET) radiopharmaceuticals in multiple myeloma. *Molecules*, 25: 134.

   https://doi.org/10.3390/molecules25010134

5. Taïeb D, Jha A, Treglia G, *et al.*, 2019, Molecular imaging and radionuclide therapy of pheochromocytoma and paraganglioma in the era of genomic characterization of disease subgroups. *Endocr Relat Cancer*, 26: R627–R652.

   https://doi.org/10.1530/ERC-19-0165

ACCSCIENCE PUBLISHING

Advances in Radiotherapy & Nuclear Medicine

REVIEW ARTICLE

Advancements and challenges in interstitial brachytherapy using iodine-125 seeds

Liting Xiong†, Yuhan Yang†, Mengyuan Li, Ping Jiang*, Chunxiao Li*, and Junjie Wang*

Department of Radiation Oncology, Peking University Third Hospital, Institute of Medical Technology, Peking University Health Science Center, Beijing, China

Abstract

Radiation therapy has been used for over a century in the treatment of tumors, with interstitial tissue treatment using radioactive seeds playing a key role in this approach. Iodine-125 (I-125) seeds are the most commonly used radioactive sealed source for permanent interstitial brachytherapy. In recent decades, significant advancements have been made in the field of interstitial radiation therapy. The development of three-dimensional (3D)-printed personalized templates, treatment planning systems, and robot-assisted systems have significantly improved the accuracy of I-125 brachytherapy. This review summarizes the advances in technology, radiobiology, physics, and immunology of I-125 brachytherapy. These advancements have improved the accuracy of dose delivery and increased the effectiveness of I-125 interstitial brachytherapy. In particular, the utilization of 3D-printed personalized templates has allowed for customized treatment planning and more precise dose delivery. Robot-assisted systems have also made significant contributions by assisting in the precise placement of radioactive seeds during treatment. However, several challenges persist within the field of interstitial I-125 brachytherapy. One of the current issues is the difficulty in accurately predicting the biological response to radiation therapy in individual patients. Addressing this challenge represents an important area for further research, as it has the potential to improve treatment outcomes and minimize side effects. In addition, there is a need for more research into the utilization of immunotherapy in conjunction with interstitial brachytherapy, as this combination has demonstrated promise in preclinical studies. Overall, this review provides a comprehensive overview of the advances and challenges associated with interstitial brachytherapy using I-125 seeds. These advancements offer a theoretical basis for achieving precise and remote medical care in brachytherapy. As technology continues to evolve, it is likely that interstitial brachytherapy will emerge as an even more effective treatment option for cancer patients.

Keywords: Iodine-125; Brachytherapy; Advancements

†These authors contributed equally to this work.

***Corresponding authors:**
Junjie Wang
(junjiewang_edu@sina.cn)
Chunxiao Li
(chunxiaoli@pku.edu.cn)
Ping Jiang
(jiangping@bjmu.edu.cn)

Citation: Xiong L, Yang Y, Li M, *et al*., 2023, Advancements and challenges in interstitial brachytherapy using iodine-125 seeds. *Adv Radiother Nucl Med,* 1(2): 0914
https://doi.org/10.36922/arnm.0914

Received: May 6, 2023

Accepted: August 21, 2023

Published Online: October 3, 2023

1. Introduction

Interstitial brachytherapy using radioactive seeds for the treatment of tumors at a close distance has a history spanning over a century. The term "brachytherapy," referring to the direct implantation of encapsulated radioactive isotopes into tumor tissue with

continuous radiation release to kill tumor cells, was first proposed by Pierre Curie in 1901[1]. Radiation therapy is categorized into different dose rates, including high dose rate (HDR) (>12 Gy/h), medium dose rate (2 – 12 Gy/h), low dose rate (LDR) (0.4 – 2 Gy/h), and ultra-LDR (<0.4 Gy/h)[2]. Among these categories, iodine-125 (I-125) is the most widely used radioactive sealed source for permanent interstitial brachytherapy. I-125 seeds have a half-life of 60 days and emit photons with an energy level of 27 keV[3]. In 1983, Professor Holm of Denmark invented transperineal I-125 seed implantation, developing a standardized procedure for treating prostate cancer with transrectal ultrasound guidance. This innovative approach ultimately demonstrated therapeutic efficacy comparable to external radiation therapy and surgery, earning its inclusion in the NCCN Guidelines for prostate cancer[4].

In the past two decades, in addition to its established use in prostate cancer, studies have demonstrated the feasibility and safety of I-125 brachytherapy in the treatment of head and neck, thoracic, abdominal, pelvic, and spinal tumors, including both primary and metastatic tumors[5-9]. Recent years have witnessed significant changes in the application of brachytherapy, driven by technological advancements. However, our understanding of the radiation biology mechanisms underlying brachytherapy remains limited, with existing data primarily focused on dose rate effects. I-125 brachytherapy stands out for its capacity to provide extremely high doses within the treatment area, a feat unattainable with external beam radiation therapy (EBRT). Moreover, it offers the additional benefit of minimizing irradiation to surrounding healthy tissue by rapidly reducing the dose outside the target lesion. To ensure the effectiveness of radiation therapy, precise dose delivery is crucial. The introduction of 3D-printed individualized templates, treatment planning systems, and robot-assisted systems has greatly enhanced the accuracy of dose delivery.

At present, with the assistance of 3D-printed individualized templates, CT-guided brachytherapy has achieved a good match of dose verification between post-operative and preoperative planning. There is no significant difference in multiple dosimetric indicators between pre-operative planning and post-operative dose verification, demonstrating an accuracy improvement exceeding 90%. Post-operative seed migration poses a potential risk, leading to adverse clinical outcomes and complications, such as pulmonary or cardiac particle embolism. The use of stranded I-125 seeds can also reduce the occurrence of seed migration following implantation. In tumor treatment, immunotherapy is gaining increasing importance, and brachytherapy's unique ability to deliver concentrated radiation with limited low-dose heterogeneity to surrounding tissue can enhance the effect of immunotherapy (Figure 1).

2. Technological development

For many years, ultrasound has been the preferred image guidance method for I-125 seeds brachytherapy in prostate cancer. However, for other types of tumors, ultrasound imaging suffers from low resolution. Consequently, over the past two decades, there has been a growing shift toward the use of computed tomography (CT)-guided and magnetic resonance imaging (MRI)-guided imaging modalities for I-125 brachytherapy. CT-guided I-125 brachytherapy offers three advantages, including enhanced target visualization, real-time monitoring of needle arrangements, and 3D digital image reconstruction. For cases of recurrent head-and-neck cancer, a previous study has shown promising results, with 1- and 2-year local control (LC) rates of 47.8% and 36.4% (median LC time of 10 months) and 1- and 2-year overall survival (OS) rates of 41.3% and 32.2% (median OS time of 8 months). Notably, the absence of adverse events was associated with improved LC[10]. In the context of portal vein tumor embolism in hepatocellular carcinoma (HCC), CT-guided I-125 brachytherapy achieved an LC rate of 78.9% and a median OS time of 14.5 months, with no reported serious adverse events[11].

The safety and efficacy of CT-guided I-125 seed brachytherapy have been well-established for treating recurrent head-and-neck cancer and portal vein tumor embolism in HCC. Due to the superior visibility of the prostate gland and capsule in MRI compared to CT and ultrasound, MRI has been implemented into the prostate I-125 brachytherapy[12,13]. Moreover, MRI offers excellent visualization of normal tissue, and its incorporation into prostate I-125 brachytherapy holds the potential to enhance dose assessment and limit radiation exposure to organs at risk[12,14]. A study on MRI-guided I-125 interstitial brachytherapy for HCC reported complete response in 22 lesions (33.8%), partial response in 24 lesions (36.9%), stable disease in 9 lesions (13.8%), and progressive disease (PD) in 10 lesions (15.4%)[15]. MRI-guided I-125 interstitial brachytherapy for HCC is technically feasible and effective.

The introduction of 3D-printed personalized templates has significantly improved the accuracy of I-125 interstitial brachytherapy. In 2012, Huang *et al.* innovatively introduced 3D printing into I-125 brachytherapy for head and neck tumors, effectively reducing needle layout errors. Subsequently, this innovative technique was extended to treat chest, abdominal, and pelvic tumors in 2015[16]. These 3D-printed templates contain essential information, such as body surface characteristics, localization markers, and

a simulated needle pathway within the treatment area (Figure 2). The treatment procedure includes preoperative planning, individualized 3D-printed template design and production, needle placement, I-125 seed implantation, and post-operative dosimetry verification, as illustrated in Figure 3. For 3D-printed personalized template-guided I-125 interstitial brachytherapy in immobilized malignant tumors, a study demonstrated that the mean D90, V90, V100, V150, and seed number showed no significant difference between pre-operation and post-operation values ($P > 0.05$) (the pre-operation vs. post-operation values were 94.96 ± 16.43% Gy vs. 91.97 ± 17.54% Gy,

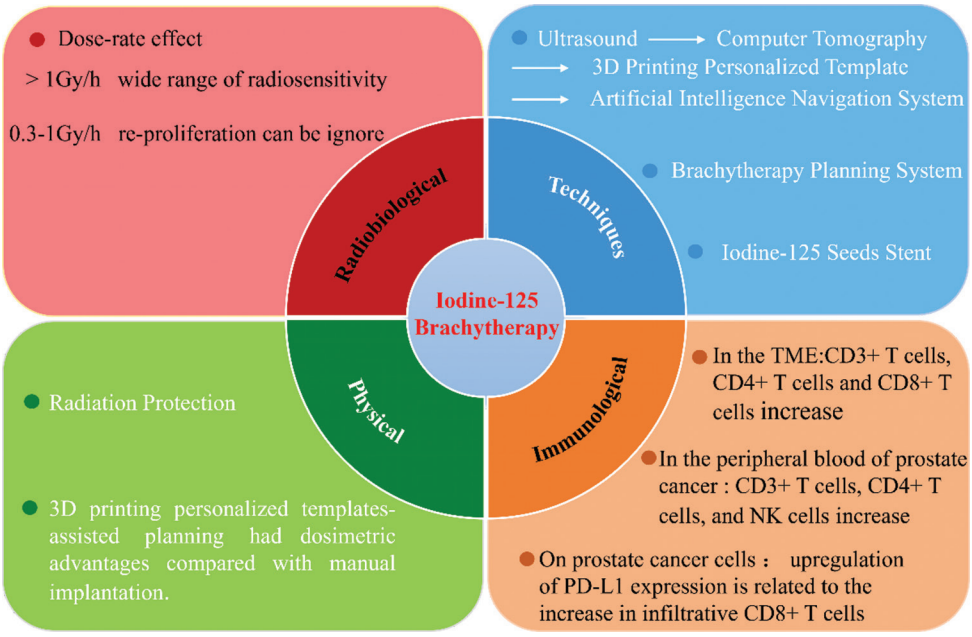

Figure 1. Summary of the progress of iodine-125 brachytherapy in several important fields. NK cells: Natural killer cells; TME: Tumor microenvironment.

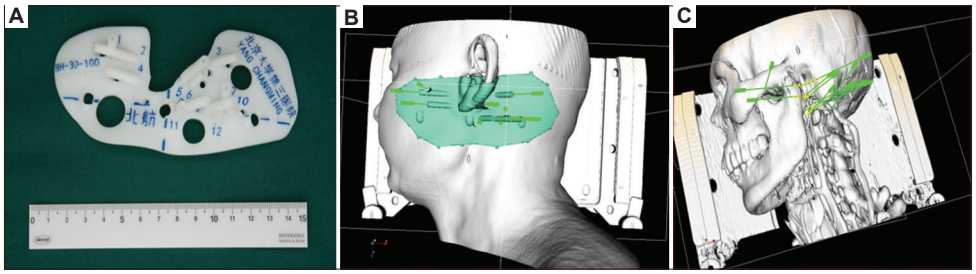

Figure 2. (A) 3D-printed template. (B) Three-dimensional reconstruction of a printed template. (C) The simulated needle pathway of the treatment area.

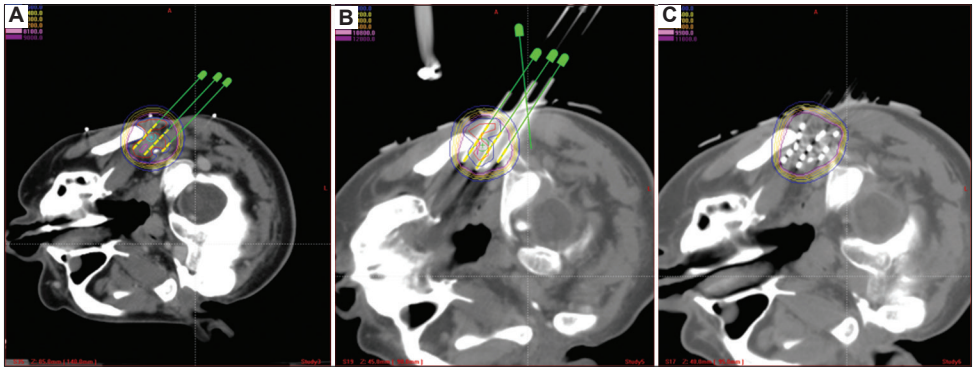

Figure 3. (A-C) The workflow of 3D-printed personalized template-assisted CT-guidance I-125 brachytherapy.

94.64 ± 1.43% vs. 93.35 ± 2.45%, 91.21 ± 1.59% vs. 89.35 ± 3.21%, 65.01 ± 5.78% vs. 63.40 ± 6.36%, and 46.67 ± 21.87% vs. 46.60 ± 22.85%, respectively)[17]. This indicates that 3D-printed personalized templates can provide better repeatability in the treatment of immobilized malignant tumors, facilitating the achievement of dose parameters outlined in the pre-operative plan. Moreover, the study showed a mean needle entrance deviation of 0.090 cm (95% confidence interval: 0.081 – 0.098) and consistent intraoperative needle depth and angle with the planned values in patients with recurrent/metastatic head-and-neck cancer, demonstrating the improved accuracy of 3D-printed personalized template-guided I-125 interstitial brachytherapy for recurrent/metastatic head-and-neck cancer[18]. This approach has the potential to become a standardized and easily reproducible procedure in the future. The utilization of fiducial markers can further enhance this process by linking the pretreatment plan with real-time operations[19,20].

While accurate needle layout is achieved, the movement of prelocalized seeds from their predesigned positions remains a challenge when using loose seeds. This movement, known as seed migration, is often a consequence of the changing tumor volume and microenvironment due to the necrosis and apoptosis of the tumor cells driven by I-125 radiation. This can result in suboptimal dosimetry due to seed migration or seed loss[21]. In addition to impacting dosimetry, seed migration can lead to adverse clinical outcomes and complications, including pulmonary or cardiac seed embolism[22]. To accurately quantify local seed migration during the 30-day period following I-125 brachytherapy, assess seed loss/migration, and identify the locations from which seeds have migrated, researchers conducted an analysis of seed displacement in 62 patients who underwent brachytherapy using stranded I-125 seeds. The analysis revealed that local seed migration and loss were minimal and mainly occurred near the inferior-lateral sides of the prostate[23]. One strategy to overcome seed migration and enhance retention is the use of stranded seeds. Several clinical trials have developed custom-linked seeds for intraoperative use in prostate cancer treatment. Compared to loose seeds, stranded seeds exhibit a reduced risk of migration, and there is also lower biochemical evidence of disease[24-26].

Robot-assisted systems have been widely studied and applied in various surgical fields[27-29]. Recent developments in the applications of robotics in the field of prostate I-125 brachytherapy are paving the way for a potentially fully automated prostate brachytherapy surgery. Current surgical robotics can be categorized into four levels of automation[30]:

i. Fully manual insertion, where surgery proceeds without any robotics assistance
ii. Manual-assisted steering, in which robotics provide sensor feedback to the surgeon
iii. Semi-automated steering, requiring surgeon-in-loop control
iv. Fully automated steering surgery, where no surgeon assistance is necessary.

The main approaches for controlling needle insertion involve pushing the needle into the tissue and rotating it around its shaft to control the direction. Manual-assisted steering mainly offers additional information about the inner needle and tissue without direct intervention. The surgeon can decide whether to follow calculated recommendations based on their surgical experience.

The assisted system can be categorized into visual devices and haptic device systems. Seifabadi *et al.* first proposed a teleoperation needle steering system that utilize MRI and a needle with a tracking coil[31]. The high-resolution images provided by MRI, along with its high precision, garner significant attention from researchers[30]. However, this system did not address the challenge of real-time imaging, which remains a limitation in most current MRI devices. In semi-automated steering systems, the needle's rotation or lateral movement is controlled, but the surgeon still maintains a dominant position in the control loop. Salcudean *et al.* proposed a four-degree freedom robot for prostate brachytherapy[32], which allowed the surgeon to retain control over the insertion procedure while benefiting from robotic accuracy. This approach also mitigated ethical concerns related to responsibility. Fully automated steering robotics perform all insertion and rotation actions according to specified insertion points and target locations, thereby reducing the risk of damage to normal tissue. However, the use of a fully automated surgical system raises serious ethical questions. Therefore, most fully automated steering systems currently exist only in laboratory settings.

3. Radiobiology in the context of radiation therapy

I-125 decays through the emission of a cascade of Auger electrons, depositing energy within the tissue over a mean path length well below 10 μm. This results in a high linear energy transfer (LET) ranging from 4 to 26 keV/μm[33]. When I-125 seeds are deposited in close proximity to the cell nucleus, this high LET of I-125 contributes to a significant radiobiological effect, which could increase the fraction of lethal DNA damage and limit the impact of hypoxia and cell cycle dynamics on destroying cancer cells[34]. Much of the data concerning brachytherapy

radiobiology and dose prescription rules, such as the Paris system, has been obtained using low-dose-rate irradiation (dose rates ranging from 40 to 100 cGy/h). Radiation-induced cell damage leading to cell death included potentially lethal and sublethal damages.

The radiobiological mechanisms of brachytherapy were poorly understood, with available data mainly focused on dose-rate effects[35]. In brachytherapy, where dose rates typically range from 0.3 Gy/h to 1 Gy/min, DNA repair is an important parameter in determining cell lethality. Isoeffect dose-response curves published in the 1980s demonstrated the dose-rate effect: A physical dose of 60 Gy delivered at 1 cGy/min (0.6 Gy/h) was radiobiologically equivalent to a total dose of 30 Gy delivered at 10 cGy/min (6 Gy/h)[36]. Measurements of sublethal damage indicated a concomitant increase in dose rate and residual double-stranded DNA breaks at the same total dose, resulting in a decrease in the surviving fraction in clonogenic assays[37]. The negative effect of decreasing dose rates on LC was also observed in a cohort of 340 breast cancer patients receiving brachytherapy increments. Patients with dose rates of 0.3 – 0.4 Gy/h experienced 31% of local recurrences, whereas those with dose rates of 0.8 – 0.9 Gy/h had no local recurrences[38]. Thus, while low-dose-rate brachytherapy offers advantages, it also has limitations in terms of the therapeutic index.

I-125 brachytherapy, a form of continuous LDR brachytherapy, relies on the radioactivity of I-125 seeds. At a dose rate of 1 Gy/h, its efficacy is equivalent to that of 2 Gy fractionated radiotherapy. Human tumor cell lines exhibit a wide range of radiosensitivity to LDR brachytherapy at 1 Gy/h. This variability may arise from clustered ionizing events causing DNA damage or damage to hyper-sensitive genomic regions[39]. A study compared clonogenic survival in 27 human tumor cell lines with varying genotypes after exposure to LDR or HDR irradiation. The study also assessed susceptibility to LDR-induced redistribution in the cell cycle in eight of these cell lines. The results indicate that the radiosensitivity of human tumor cells to both LDR and HDR irradiation is genotype-dependent[40], and cell radiosensitivity varies across different cell cycle phases[41]. For I-125 brachytherapy in gastric tumor xenografts, increased apoptosis within tumors was reported, along with G2/M cell arrests. This was accompanied by an increase in intratumor expression of vascular endothelial growth factor and nuclear factor-kappa B in tumor neovessels[42]. Furthermore, compared to 6 MV X-rays with a dose rate of 4 Gy/min, I-125 brachytherapy with a dose rate of 2.77 cGy/h demonstrated more effective induction of cell apoptosis and G2/M cell cycle arrest in colon cancer cells[43].

Repopulation is a phenomenon that impacts rapidly proliferating normal tissues and tumors, serving as a compensatory mechanism for radiation-induced cell death. The linear-quadratic model is primarily focused on cell death, where the dose-effect relationship is linear at low doses due to directly lethal damage and becomes quadratic at higher doses due to sublethal damage. However, when examining the radiobiology of brachytherapy specifically, the role of proliferation is generally minimal, except in cases involving treatments lasting several weeks, as seen with I-125 seed permanent implants. Therefore, I-125 seeds may not be suitable for rapidly proliferating tumors with high α/β values[44]. The level of tumor hypoxia exhibits an inverse correlation with the probability of tumor control. Hypoxic tumors can be identified through perfusion MRI and specific tracers, and their presence can be correlated with histological findings (hypoxia-inducible factor-1 expression), tumor genomic analysis, and prognosis[45]. In low-dose-rate treatments spanning several days, the contribution of reoxygenation is minimal.

The biological effective dose (BED) is a measure of the biological effect of radiation[46]. BED enables the comparison of different irradiation regimens. One study introduces a method to use BED for comparing and integrating dose data from both EBRT and interstitial I-125 brachytherapy components in the treatment of prostate cancer. This involves converting the dose distributions of conformal EBRT and conventional interstitial I-125 brachytherapy into the common "language" of BED distributions, facilitating the comparison and integration of radiation treatment plans for prostate cancer[47]. In the context of I-125 brachytherapy with conventional doses, the relative biological effect is 1.4, and the dose rate is approximately 0.07 Gy/h. This profile appears to be more suitable for treating radiosensitive tumors with long doubling times and rapid shrinkage[48,49]. Therefore, the optimal application of I-125 brachytherapy may depend on selecting tumors that are relatively radiosensitive and where late responses are dose-limited in anatomical sites[50]. It is worth noting that an increasing number of studies are reporting equivalent efficacy between HDR and LDR brachytherapy. In cases of fast-growing tumors, HDR brachytherapy might offer more advantages than LDR brachytherapy due to enhanced cellular repair capacity[51-53].

4. Physics of I-125 brachytherapy

Brachytherapy implementation hinges on several critical factors, including the application of specialized dosimetric systems to calculate treatment duration and dosage, the calibration of radioactive sources, and the monitoring of seed positioning for geometric accuracy.

Brachytherapy offers several advantages compared to EBRT, including superior dose localization within the target volume, enhanced sparing of normal tissue, and cost-effectiveness. Guidelines for brachytherapy dosimetry and source calibration have been established by organizations such as the American Association of Physicists in Medicine (AAPM) and the Groupe Européen de Curiethérapie-European Society for Radiotherapy and Oncology. These guidelines, as exemplified in the AAPM Task Group 43 report, recommend specific dose parameters, including D90>100%, V100>90%~95%, and V150<50%~60%[19,54]. A comparative study evaluated the dosimetric parameters of I-125 brachytherapy for lung cancer between intraoperative and pre-operative planning, revealing the superiority of intraoperative planning. Intraoperative planning demonstrated significantly higher V100, V150, and V200 values compared to pre-operative planning[55]. In addition, intraoperative planning exhibited improved coverage, conformity, and quality indices, along with reduced dose uniformity indices compared to pre-operative planning[55].

Ensuring accurate dose delivery is crucial for therapeutic efficacy in radiotherapy. A key component for accurate dose delivery with brachytherapy sources is the ability to determine the absolute radiation output at a reference point. For photon sources, this is usually achieved by correlating the radiation output to air-Kerma strength (SK) in the U.S. and reference air-kerma rate in Europe. A primary calibration standard for low-energy LDR I-125 brachytherapy sources was developed at the National Bureau of Standards (the former name for NIST) in 1984 by Loftus, using the Ritz free air ionization chamber[56]. However, discrepancies in source measurements arose, with the 1999 value for a given I-125 source differing from the 1998 standard by 3%. Subsequently, all source models underwent reevaluation in 2000, revealing discrepancies ranging from 2% to 7% in 1999. To address these variations, the AAPM mandates that brachytherapy source manufacturers annually compare their in-house standard to the NIST standard for low-energy sources and, every 2 years, with a primary standards dosimetry laboratory-traceable standard for high-energy sources[57,58].

The Task Group 56 report provides guidelines for quality control and quality assurance in brachytherapy procedures[59]. Detailed information on the use of robotics in brachytherapy for source delivery can be found in the TG-192 report[60]. However, when it comes to the dosimetric requirements of innovative brachytherapy devices or the implementation of new clinical applications, there is a limited availability of guidelines. Therefore, the role of medical physicists becomes even more critical in the clinical implementation and evaluation of innovative brachytherapy devices and applications. With the introduction of 3D printing, studies have indicated that there is comparability between the dosimetric parameters of pre-operative and post-operative planning for D90, V100, and V200 in 3D printing-guided I-125 brachytherapy for recurrent high-grade gliomas[61].

When comparing I-125 LDR brachytherapy to HDR brachytherapy for prostate cancer, a randomized trial suggested that the D90, V100, and V150 values of the LDR brachytherapy group were significantly higher than those of the HDR brachytherapy group. In addition, the urethral D10, D30, and rectal D10 values of the LDR brachytherapy group were significantly higher than those of the HDR brachytherapy group[62]. Therefore, while both I-125 LDR brachytherapy and HDR brachytherapy can offer effective dose coverage, I-125 brachytherapy tends to result in slightly higher doses to the urethra and rectum, potentially contributing to the occurrence of genitourinary and gastrointestinal toxicity in LDR brachytherapy. In addition, a retrospective analysis of 25 patients with pancreatic cancer indicated that 3D-printed personalized templates-assisted I-125 brachytherapy provided dosimetric advantages in terms of V100 when compared to manual implantation. In essence, current brachytherapy, guided by CT scans and assisted by 3D-printed personalized templates, has achieved a perfect match between post-operative dose verification and pre-operative planning. The pre-operative planning and post-operative dose verification demonstrated no significant difference in multiple dosimetric parameters, with accuracy improved by over 90%. The incorporation of 3D-printed personalized templates proves beneficial in achieving individualized treatment and reducing dependence on operator experience.

In recent years, several scholars have explored the application of single photon emission CT/CT for detecting the radioactive concentration distribution following particle implantation and utilizing it to evaluate the therapeutic effect. This novel approach warrants further investigation[63,64]. It is worth noting that, in contrast to HDR brachytherapy, I-125 brachytherapy has some drawbacks, such as potential radiation exposure to clinical personnel during the procedure and subsequent exposure to patients' family members and the general public. Nonetheless, studies have indicated that the radiation dose carried by patients after prostate cancer particle implantation is minimal, approaching levels observed in the general population. Apart from some limitations, like prolonged child-carrying restrictions, patients can generally lead a normal daily life without significant disruption[65].

5. Immunological aspects of I-125 brachytherapy

In vitro and clinical studies have confirmed the synergistic effect between radiation-induced tumor "*in situ*" vaccine effect and the remodeling of the immune microenvironment when combined with immune checkpoint inhibitor therapy across various tumor types[66,67]. When combined with immunotherapy, the objective of radiotherapy extends beyond local tumor control. It aims to maximize the body's anti-tumor immune response, serving as an adjuvant that produces synergistic effects alongside immunotherapy[68].

The changes in the local tumor immune microenvironment (TIME) and the consequent changes in systemic immune status following I-125 close-range therapy for post-operative local tumors remain unclear. In contrast to EBRT, I-125 brachytherapy offers the advantage of high conformity, enabling the delivery of high doses to the target area while minimizing damage to the surrounding normal tissues. This protection extends to radiosensitive lymphoid immune cells in normal tissues, safeguarding them from radiation.

At present, several relevant studies have focused on prostate cancer. Following I-125 brachytherapy for prostate cancer, there is a significant increase in the density of CD3+, CD4+, and CD8+ T cells within the tumor microenvironment. More importantly, the expression rate of PD-1+ T cells also shows a significant increase compared to pre-seed implantation levels. In one study, eight patients who were PD-1 negative before treatment became positive after undergoing brachytherapy, and the density of infiltrating PD-1+ T cells increased significantly. Therefore, I-125 brachytherapy can induce the generation of the tumor antigen-specific PD-1+CD8+ T cells, recruiting them into the tumor microenvironment. In addition, the study found that after I-125 brachytherapy, the number of CD3+ T cells, CD4+ T cells, and natural killer cells in the peripheral blood of prostate cancer patients increased significantly. Although the number of CD8+ T cells did not exhibit a significant change, the CD4/CD8 ratio increased significantly.

At present, the role of radiotherapy in promoting the infiltration of CD8+ T cells into tumor lesions is widely recognized, suggesting the recruitment of tumor antigen-specific CD8+ T cells into the tumor microenvironment[69]. Following I-125 brachytherapy, there is a significant increase in PD-L1 expression on prostate cancer cells. This increase in PD-L1 expression is associated with the infiltrating CD8+ T cells in the tumor microenvironment, particularly those secreting interferon (IFN)-γ, which promotes PD-L1 expression on tumor cells. As a result, the upregulation of PD-L1 expression at this stage reflects the immune response driven by infiltrating CD8+ T cells secreting IFN-γ. Consequently, PD-L1 expression on tumor cells during this phase should not solely be interpreted as an indication of immune suppression within the TIME. Instead, it signifies the promotion of the tumor immune response by CD8+ T cells due to radiotherapy. Taken together, these observations suggest a correlation between the upregulation of PD-L1 expression on tumor cells after I-125 brachytherapy and the heightened presence of infiltrating CD8+ T cells. This mechanism, which promotes the upregulation of PD-L1 expression on tumor cells, essentially represents a negative feedback mechanism regulating the body's immune response. Unfortunately, tumors exploit this mechanism as a tool to develop adaptive immune tolerance. Therefore, several studies propose that PD-L1 expression on tumor cells can be used as a marker for the emergence of adaptive immune resistance following the infiltration of tumor antigen-specific T lymphocytes[70,71].

At the same time, when comparing the expression of pSTAT1 before and after treatment (pSTAT1 being the downstream product resulting from the combination of IFN and its receptor), it was found that individuals who responded effectively to PD-1/PD-L1 blockade treatment exhibited markedly increased pSTAT1 expression before and after treatment, in contrast to those who did not respond to treatment. This finding suggests that individuals who responded effectively to PD-1/PD-L1 blockade treatment display elevated levels of both IFN-γ and PD-L1 expression. Hence, it implies that IFN-γ plays a role in promoting the expression of PD-L1.

Combining insights from previous studies, a significant increase in CD4+ T cell expression was observed in both peripheral blood and the tumor microenvironment following I-125 brachytherapy for prostate cancer. Notably, CD4+ T cell expression within the tumor microenvironment was significantly higher than that of CD8+ T cells. CD4+ T cells exert their anti-tumor immune function through various mechanisms, including direct tumor immune effects by regulating the expression of perforin and granzyme, indirect modulation of the tumor microenvironment to coordinate anti-tumor immunity, and their role in immunotherapy[72]. The generation of CD8+ memory T lymphocytes relies on the assistance of CD4+ T cells. Studies have indicated that, even when PD-1/PD-L1 blockade therapy is ineffective, CD4+ T cells can re-exert the anti-tumor immune response of CD8+ T cells[73]. In a mouse model of prostate cancer, where radiation therapy was combined with immunotherapy, a notable increase in tumor-specific CD4+ T cells

occurred. Specifically, the majority of these cells were of Th1 subtype, while only a small proportion represented prostate cancer-specific Th2 and Th17 subtypes. Th1 cells, the main subtype of CD4+ T cells, play a pivotal role in the tumor immune response[74]. They accomplish this by secreting cytokines such as IFN-γ and tumor necrosis factor-α, which have the ability to eliminate tumor cells and, consequently, contribute to anti-tumor immune responses[75]. T-bet, a characteristic transcription factor located on the surface of Th1 cells, is responsible for regulating their differentiation, maturation, and the secretion of these cytokines[76].

A study investigated the changes in the distribution of tumor-infiltrating T lymphocytes in prostate cancer patients, both before and after radical prostatectomy, particularly focusing on cases of biochemical recurrence. The findings revealed a substantial increase in the infiltration of CD8+, PD-1+, and Foxp3+ T cells compared to pre-surgery levels when biochemical recurrence was observed. Among these, Treg cells, an important subset of CD4+ T lymphocytes known for their immunosuppressive activity, play a significant role in inhibiting the anti-tumor immune response[76]. The transcription factor Foxp3 is specific to Treg cells and regulates their differentiation and maturation[77]. Furthermore, it was observed that the increased presence of PD-1+ and Foxp3+ T cells was negatively correlated with patient prognosis. The study suggested that this phenomenon may be attributed to genetic mutations occurring during tumor relapse, which result in the induction of new tumor antigens and a subsequent immune response. The increased expression of PD-1+ T cells in the tumor after the activation of tumor-specific T lymphocytes is considered a manifestation of immune escape[78].

After prostate cancer brachytherapy, the immunostimulatory effect on the tumor diminishes as the radioactivity of implanted particles decreases. While a substantial number of CD4+ and CD8+ T cells continue to infiltrate the tumor, the expression of PD-1+ T cells remains low, indicating a reduction in the presence of tumor antigen-specific T cells. Moreover, in alignment with the concept of tumor immune editing, it was observed that as prostate cancer relapses and progresses, the expression of PD-1+ T cells gradually decreases, indicating a gradual weakening of the tumor-specific immune response. This phenomenon aligns with the characteristics of tumor immune evasion[79]. In light of these observations, it is postulated that the immune microenvironment within prostate cancer tumors undergoes dynamic changes following I-125 brachytherapy. This suggests the existence of a specific time frame during which combining I-125 brachytherapy with PD-1/PD-L1 blockade therapy for prostate cancer could be particularly effective[80,81].

A recurring observation across these studies involves the detection of potential remote immune activation through peripheral blood analysis, situated away from the primary tumor. In addition, these investigations have further identified compensatory immune suppression signals following brachytherapy. This suppression manifests in various forms, including the upregulation of Tregs and the activation of well-established immune checkpoints such as PD-L1. The emergence of immune suppression subsequent to radiation exposure has previously been described in the context of *in vitro* beam radiation. This phenomenon may also constitute a limiting factor within the realm of I-125 brachytherapy. Overall, these data lend support to the notion of combining I-125 brachytherapy with immunotherapy. Such a combination holds the potential not only to improve localized tumor elimination but also to enhance distant anti-tumor immune responses.

6. Discussion and perspective

Reflecting on the evolution of interstitial I-125 brachytherapy, the pursuit of precision in brachytherapy has consistently remained a common goal of medical professionals and scholars in this field. As imaging technology has continuously advanced, it has provided clinicians with a visual "eye," progressively expanding the scope of applications for I-125 brachytherapy. Concurrently, the continuous optimization of this "vision" has enhanced the accuracy of I-125 brachytherapy.

On the one hand, the development of I-125 brachytherapy has been dose-oriented, focusing on achieving greater accuracy in irradiation dosage delivery. This dedication to enhancing accuracy has been exemplified by the introduction of 3D-printed personalized templates, treatment planning systems, and robot-assisted systems. These innovations collectively contribute to a more accurate dose delivery. Predicting future developments, including new products, their potential applications, and the challenges they may introduce, poses a considerable challenge. Therefore, the competence of medical physicists becomes increasingly vital when it comes to the clinical implementation and evaluation of innovative brachytherapy devices and applications. The sensitivity of various tumor tissues to radiotherapy in I-125 brachytherapy varies. However, apart from prostate cancer, determining the optimal radiation dose for other tumors remains an ongoing challenge. While there have been several editions of consensus proposing recommended dose ranges for different tumor types, many of these recommendations

are primarily based on expert clinical experience and lack large-scale multicenter clinical studies.

On the other hand, the development of I-125 brachytherapy must also consider spatial orientation, focusing on optimizing the path for radiation source implantation. Besides targeting the tumor site, the role of the operator in brachytherapy should not be overlooked. The introduction of 3D-printed personalized templates has been conducive to achieving personalized treatment and reducing dependence on operator experience. In addition, robot-assisted systems provide solutions for the puncture challenges in brachytherapy across various tumor sites through mechanical automation-assisted needle implantation. However, recent research on robotic technology in the field of brachytherapy has mainly focused on prostate cancer and radioactive particle implantation, with insufficient attention given to other diseases suitable for brachytherapy.

In the future, robotic system technologies can be leveraged to their full potential to realize precise and remote medical treatment for brachytherapy. Preliminary research indicates that the combined treatment of brachytherapy and immunotherapy demonstrates favorable tolerability and warrants further investigation. However, several unresolved issues remain regarding the optimal method of coordinating these two treatments, including duration and radiation dose. Moreover, additional preclinical and clinical studies are imperative to gain a comprehensive understanding of the immune regulatory effects of I-125 brachytherapy.

Acknowledgments

None.

Funding

This work was funded by the National Natural Science Foundation of China (grants 82173174 to C. Li and 82073335 to J. Wang), the Natural Science Foundation of Beijing Municipality (grants 7232207 to C. Li), Intramural funding from the Beijing University Third Hospital (grant BYSY2022044 to C. Li), the Special Fund of the National Clinical Key Specialty Construction Program, P. R. China (2021), and the Cancer Precision Radiotherapy Spark Program of China International Medical Foundation (grant number: 2019-N-11-13).

Conflict of interest

The authors declare no potential conflicts of interest.

Author contributions

Conceptualization: Chunxiao Li
Investigation: Mengyuan Li
Supervision: Ping Jiang, Junjie Wang
Writing – original draft: Liting Xiong, Yuhan Yang, Chunxiao
Writing – review and editing: Chunxiao Li
All authors have agreed to the final manuscript and approved the submitted version.

Ethics approval and consent to participate

Not applicable.

Consent for publication

Not applicable.

Availability of data

Not applicable.

References

1. Parker SL, 1997, Cancer statistics, 1997. *CA Cancer J Clin*, 47: 5–27.

https://doi.org/10.3322/canjclin.47.1.5

2. Rosenberg I, 2008, Radiation oncology physics: A handbook for teachers and students. *Br J Cancer*, 98: 1020.

https://doi.org/10.1038/sj.bjc.6604224

3. Yoshioka Y, 2009, Current status and perspectives of brachytherapy for prostate cancer. *Int J Clin Oncol*, 14: 31–36.

https://doi.org/10.1007/s10147-008-0866-z

4. Torp-Pedersen S, Holm HH, Littrup PJ, 1987, Transperineal I-125 seed implantation in prostate cancer guided by transrectal ultrasound. *Prog Clin Biol Res*, 237: 143–152.

5. Ji Z, Jiang Y, Guo F, *et al.*, 2020, Safety and efficacy of CT-guided radioactive iodine-125 seed implantation assisted by a 3D printing template for the treatment of thoracic malignancies. *J Cancer Res Clin Oncol*, 146: 229–236.

https://doi.org/10.1007/s00432-019-03050-7

6. Ji Z, Jiang Y, Tian S, *et al.*, 2019, The effectiveness and prognostic factors of CT-guided radioactive I-125 seed implantation for the treatment of recurrent head and neck cancer after external beam radiation therapy. *Int J Radiat Oncol Biol Phys*, 103: 638–645.

https://doi.org/10.1016/j.ijrobp.2018.10.034

7. Wang H, Wang J, Jiang Y, *et al.*, 2013, The investigation of 125I seed implantation as a salvage modality for unresectable pancreatic carcinoma. *J Exp Clin Cancer Res*, 32: 106.

https://doi.org/10.1186/1756-9966-32-106

8. Wang J, Yuan H, Ma Q, *et al.*, 2010, Interstitial 125I seeds implantation to treat spinal metastatic and primary paraspinal malignancies. *Med Oncol*, 27: 319–326.

https://doi.org/10.1007/s12032-009-9212-1

9. Yao L, Cao Q, Wang J, *et al*., 2016, CT-Guided (125)I Seed Interstitial brachytherapy as a salvage treatment for recurrent spinal metastases after external beam radiotherapy. *Biomed Res Int*, 2016: 8265907.

https://doi.org/10.1155/2016/8265907

10. Li Y, Jiang Y, Wang J, 2023, Safety and efficacy of CT-guided radioactive iodine-125 seed implantation as a salvage treatment for recurrent head and neck cancer after two or more courses of radiotherapy. *Radiat Oncol*, 18: 73.

https://doi.org/10.1186/s13014-023-02254-z

11. Qiu Z, Yu C, Qiu X, *et al*., 2023, Safety and efficacy of CT-guided iodine-125 brachytherapy for portal vein tumor thrombus in hepatocellular carcinoma. *Acad Radiol*, 30 Suppl 1: S53–S60.

https://doi.org/10.1016/j.acra.2023.02.006

12. McLaughlin PW, Troyer S, Berri S, *et al*., 2005, Functional anatomy of the prostate: Implications for treatment planning. *Int J Radiat Oncol Biol Phys*, 63: 479–491.

https://doi.org/10.1016/j.ijrobp.2005.02.036

13. Takiar V, Pugh TJ, Swanson D, *et al*., 2014, MRI-based sector analysis enhances prostate palladium-103 brachytherapy quality assurance in a phase II prospective trial of men with intermediate-risk localized prostate cancer. *Brachytherapy*, 13: 68–74.

https://doi.org/10.1016/j.brachy.2013.04.001

14. Register SP, Kudchadker RJ, Levy LB, *et al*., 2013, An MRI-based dose--reponse analysis of urinary sphincter dose and urinary morbidity after brachytherapy for prostate cancer in a phase II prospective trial. *Brachytherapy*, 12: 210–216.

https://doi.org/10.1016/j.brachy.2012.10.006

15. Lin ZY, Lin J, Lin C, *et al*., 2012, 1.5T conventional MR-guided iodine-125 interstitial implants for hepatocellular carcinoma: Feasibility and preliminary clinical experience. *Eur J Radiol*, 81: 1420–1425.

https://doi.org/10.1016/j.ejrad.2011.03.043

16. Huang MW, Liu SM, Zheng L, *et al*., 2012, A digital model individual template and CT-guided 125I seed implants for malignant tumors of the head and neck. *J Radiat Res*, 53: 973–977.

https://doi.org/10.1093/jrr/rrs046

17. Zhang H, Dev D, Yu H, *et al*., 2019, Feasibility of three-dimensional-printed template-guided (125)I seed brachytherapy and dosimetric evaluation in patients with malignant tumor. *J Cancer Res Ther*, 15: 793–800.

https://doi.org/10.4103/jcrt.JCRT_347_18

18. Qiu B, Jiang Y, Ji Z, *et al*., 2021, The accuracy of individualized 3D-printing template-assisted I(125) radioactive seed implantation for recurrent/metastatic head and neck cancer. *Front Oncol*, 11: 664996.

https://doi.org/10.3389/fonc.2021.664996

19. Rivard MJ, Coursey BM, DeWerd LA, *et al*., 2004, Update of AAPM Task Group No. 43 Report: A revised AAPM protocol for brachytherapy dose calculations. *Med Phys*, 31: 633–674.

https://doi.org/10.1118/1.1646040

20. Salembier C, Lavagnini P, Nickers P, *et al*., 2007, Tumour and target volumes in permanent prostate brachytherapy: A supplement to the ESTRO/EAU/EORTC recommendations on prostate brachytherapy. *Radiother Oncol*, 83: 3–10.

https://doi.org/10.1016/j.radonc.2007.01.014

21. Kunos CA, Resnick MI, Kinsella TJ, *et al*., 2004, Migration of implanted free radioactive seeds for adenocarcinoma of the prostate using a Mick applicator. *Brachytherapy*, 3: 71–77.

https://doi.org/10.1016/j.brachy.2004.06.002

22. Reed DR, Wallner KE, Merrick GS, *et al*., 2007, A prospective randomized comparison of stranded vs. loose 125I seeds for prostate brachytherapy. *Brachytherapy*, 6: 129–134.

https://doi.org/10.1016/j.brachy.2007.01.003

23. Nuver TT, Hilgers GC, Kattevilder RA, *et al*., 2022, Local seed displacement from day 0 to day 30 in I-125 permanent prostate brachytherapy: A detailed, computed tomography-based analysis. *Brachytherapy*, 21: 208–215.

https://doi.org/10.1016/j.brachy.2021.12.009

24. Herbert C, Morris WJ, Hamm J, *et al*., 2011, The effect of loose versus stranded seeds on biochemical no evidence of disease in patients with carcinoma of the prostate treated with iodine-125 brachytherapy. *Brachytherapy*, 10: 442–448.

https://doi.org/10.1016/j.brachy.2011.01.011

25. Al-Qaisieh B, Carey B, Ash D, *et al*., 2004, The use of linked seeds eliminates lung embolization following permanent seed implantation for prostate cancer. *Int J Radiat Oncol Biol Phys*, 59: 397–399.

https://doi.org/10.1016/j.ijrobp.2003.10.034

26. Ishiyama H, Satoh T, Kawakami S, *et al*., 2014, A prospective quasi-randomized comparison of intraoperatively built custom-linked seeds versus loose seeds for prostate brachytherapy. *Int J Radiat Oncol Biol Phys*, 90: 134–139.

https://doi.org/10.1016/j.ijrobp.2014.05.009

27. Ahmed AK, Zygourakis CC, Kalb S, *et al*., 2019, First spine surgery utilizing real-time image-guided robotic assistance. *Comput Assist Surg* (*Abingdon*), 24: 13–17.

https://doi.org/10.1080/24699322.2018.1542029

28. Egberts JH, Möller T, Becker T, 2019, Robotic-assisted sleeve lobectomy using the four-arm technique in the DaVinci Si® and Xi® systems. *Thorac Cardiovasc Surg*, 67: 603–605.

https://doi.org/10.1055/s-0038-1660508

29. Rohatgi P, Jafrani RJ, Brandmeir NJ, *et al*., 2018, Robotic-guided bihippocampal and biparahippocampal depth placement for responsive neurostimulation in bitemporal lobe epilepsy. *World Neurosurg*, 111: 181–189.

https://doi.org/10.1016/j.wneu.2017.10.164

30. Dhaliwal SS, Chettibi T, Wilby S, *et al*., 2021, Review of clinical and technological consideration for MRI-guided robotic prostate brachytherapy. *IEEE Trans Med Robot Bionics*, 3: 583–605.

https://doi.org/10.1109/TMRB.2021.3097127

31. Seifabadi R, Song SE, Krieger A, *et al*., 2012, Robotic system for MRI-guided prostate biopsy: Feasibility of teleoperated needle insertion and *ex vivo* phantom study. *Int J Comput Assist Radiol Surg*, 7: 181–190.

https://doi.org/10.1007/s11548-011-0598-9

32. Salcudean SE, Prananta TD, Morris WJ, *et al*., 2008, A Robotic Needle Guide for Prostate Brachytherapy. In: 2008 IEEE International Conference on Robotics and Automation.

33. Bodei L, Kassis AI, Adelstein SJ, *et al*., 2003, Radionuclide therapy with iodine-125 and other auger-electron-emitting radionuclides: Experimental models and clinical applications. *Cancer Biother Radiopharm*, 18: 861–877.

https://doi.org/10.1089/108497803322702833

34. Welt S, Scott AM, Divgi CR, *et al*., 1996, Phase I/II study of iodine 125-labeled monoclonal antibody A33 in patients with advanced colon cancer. *J Clin Oncol*, 14: 1787–1797.

https://doi.org/10.1200/JCO.1996.14.6.1787

35. Chargari C, Van Limbergen E, Mahantshetty U, *et al*., 2018, Radiobiology of brachytherapy: The historical view based on linear quadratic model and perspectives for optimization. *Cancer Radiother*, 22: 312–318.

https://doi.org/10.1016/j.canrad.2017.11.011

36. Thames HD, 1985, An "incomplete-repair" model for survival after fractionated and continuous irradiations. *Int J Radiat Biol Relat Stud Phys Chem Med*, 47: 319–339.

https://doi.org/10.1080/09553008514550461

37. Dikomey E, Brammer I, 2000, Relationship between cellular radiosensitivity and non-repaired double-strand breaks studied for different growth states, dose rates and plating conditions in a normal human fibroblast line. *Int J Radiat Biol*, 76: 773–781.

https://doi.org/10.1080/09553000050028922

38. Deore SM, Sarin R, Dinshaw KA, *et al*., 1993, Influence of dose-rate and dose per fraction on clinical outcome of breast cancer treated by external beam irradiation plus iridium-192 implants: Analysis of 289 cases. *Int J Radiat Oncol Biol Phys*, 26: 601–606.

https://doi.org/10.1016/0360-3016(93)90275-z

39. Steel GG, 1991, The ESTRO Breur lecture. Cellular sensitivity to low dose-rate irradiation focuses the problem of tumour radioresistance. *Radiother Oncol*, 20: 71–83.

https://doi.org/10.1016/0167-8140(91)90140-c

40. Williams JR, Zhang Y, Zhou H, *et al*., 2008, Overview of radiosensitivity of human tumor cells to low-dose-rate irradiation. *Int J Radiat Oncol Biol Phys*, 72: 909–917.

https://doi.org/10.1016/j.ijrobp.2008.06.1928

41. Baumann M, Dörr W, Petersen C, *et al*., 2003, Repopulation during fractionated radiotherapy: Much has been learned, even more is open. *Int J Radiat Biol*, 79: 465–467.

https://doi.org/10.1080/0955300031000160259

42. Zhang WF, Jin WD, Li B, *et al*., 2014, Effect of brachytherapy on NF-kappaB and VEGF in gastric carcinoma xenografts. *Oncol Rep*, 32; 635–640.

https://doi.org/10.3892/or.2014.3255

43. Wang H, Li J, Qu A, *et al*., 2013, The different biological effects of single, fractionated and continuous low dose rate irradiation on CL187 colorectal cancer cells. *Radiat Oncol*, 8: 196.

https://doi.org/10.1186/1748-717X-8-196

44. Hennequin C, Mazeron JJ, 2013, Radiobiology in brachytherapy. *Cancer Radiother*, 17: 81–84.

https://doi.org/10.1016/j.canrad.2013.03.001

45. Halle C, Andersen E, Lando M, *et al*., 2012, Hypoxia-induced gene expression in chemoradioresistant cervical cancer revealed by dynamic contrast-enhanced MRI. *Cancer Res*, 72: 5285–5295.

https://doi.org/10.1158/0008-5472.CAN-12-1085

46. Barendsen GW, 1982, Dose fractionation, dose rate and iso-effect relationships for normal tissue responses. *Int J Radiat Oncol Biol Phys*, 8: 1981–1997.

https://doi.org/10.1016/0360-3016(82)90459-x

47. Jani AB, Hand CM, Lujan AE, *et al*., 2004, Biological effective dose for comparison and combination of external beam and low-dose rate interstitial brachytherapy prostate cancer treatment plans. *Med Dosim*, 29: 42–48.

https://doi.org/10.1016/j.meddos.2003.09.005

48. Antipas V, Dale RG, Coles IP, 2001, A theoretical investigation into the role of tumour radiosensitivity, clonogen repopulation, tumour shrinkage and radionuclide RBE in permanent brachytherapy implants of 125I and 103Pd. *Phys Med Biol*, 46: 2557–25569.

https://doi.org/10.1088/0031-9155/46/10/304

49. Ling CC, Li WX, Anderson LL, 1995, The relative biological effectiveness of I-125 and Pd-103. *Int J Radiat Oncol Biol Phys*, 32: 373–378.

https://doi.org/10.1016/0360-3016(95)00530-C

50. Armpilia CI, Dale RG, Coles IP, *et al*., 2003, The determination of radiobiologically optimized half-lives for radionuclides used in permanent brachytherapy implants. *Int J Radiat Oncol Biol Phys*, 55: 378–385.

https://doi.org/10.1016/s0360-3016(02)04208-6

51. Manimaran S, 2007, Radiobiological equivalent of low/high dose rate brachytherapy and evaluation of tumor and normal responses to the dose. *Radiat Med*, 25: 229–235.

https://doi.org/10.1007/s11604-007-0131-9

52. Patankar SS, Tergas AI, Deutsch I, *et al*., 2015, High versus low-dose rate brachytherapy for cervical cancer. *Gynecol Oncol*, 136: 534–541.

https://doi.org/10.1016/j.ygyno.2014.12.038

53. Cagetti LV, Zemmour C, Salem N, *et al*., 2019, High-dose-rate vs. low-dose-rate interstitial brachytherapy boost for anal canal cancers. *Brachytherapy*, 18: 814–822.

https://doi.org/10.1016/j.brachy.2019.08.005

54. Nath R, Anderson LL, Luxton G, *et al*., 1995, Dosimetry of interstitial brachytherapy sources: recommendations of the AAPM Radiation Therapy Committee Task Group No. 43. American Association of Physicists in Medicine. *Med Phys*, 22: 209–234.

https://doi.org/10.1118/1.597458

55. Li R, Ying Z, Yuan Y, *et al*., 2019, Comparison of two iodine-125 brachytherapy implant techniques for the treatment of lung tumor: Preplanning and intraoperative planning. *Brachytherapy*, 18: 87–94.

https://doi.org/10.1016/j.brachy.2018.08.007

56. Loftus TP, 1984, Exposure standardization of Iodine-125 seeds used for brachytherapy. *J Res Natl Bur Stand* (*1977*), 89: 295–303.

https://doi.org/10.6028/jres.089.017

57. DeWerd LA, Huq MS, Das IJ, *et al*., 2004, Procedures for establishing and maintaining consistent air-kerma strength standards for low-energy, photon-emitting brachytherapy sources: Recommendations of the Calibration Laboratory Accreditation Subcommittee of the American Association of Physicists in Medicine. *Med Phys*, 31: 675–681.

https://doi.org/10.1118/1.1645681

58. Perez-Calatayud J, Ballester F, Das RK, *et al*., 2012, Dose calculation for photon-emitting brachytherapy sources with average energy higher than 50 keV: Report of the AAPM and ESTRO. *Med Phys*, 39: 2904–2929.

https://doi.org/10.1118/1.3703892

59. Nath R, Anderson LL, Meli JA, *et al*., 1997, Code of practice for brachytherapy physics: Report of the AAPM Radiation Therapy Committee Task Group No. 56. American Association of Physicists in Medicine. *Med Phys*, 24: 1557–1598.

60. Podder TK, Beaulieu L, Caldwell B, *et al*., 2014, AAPM and GEC-ESTRO guidelines for image-guided robotic brachytherapy: Report of Task Group 192. *Med Phys*, 41: 101501.

https://doi.org/10.1118/1.4895013

61. Liu S, Wang H, Wang C, *et al*., 2019, Dosimetry verification of 3D-printed individual template based on CT-MRI fusion for radioactive (125)I seed implantation in recurrent high-grade gliomas. *J Contemp Brachytherapy*, 11: 235–242.

https://doi.org/10.5114/jcb.2019.85729

62. Major T, Polgár C, Jorgo K, *et al*., 2017, Dosimetric comparison between treatment plans of patients treated with low-dose-rate vs. high-dose-rate interstitial prostate brachytherapy as monotherapy: Initial findings of a randomized clinical trial. *Brachytherapy*, 16: 608–615.

https://doi.org/10.1016/j.brachy.2017.02.003

63. Zhang H, Liang Y, Qiu G, *et al*., 2019, Precision dose measurement of 125I seed in solid water through SPECT/CT detecting. *J Cancer Res Ther*, 15: 291–297.

https://doi.org/10.4103/jcrt.JCRT_522_18

64. Zhang H, Zhao X, Wang J, *et al*., 2016, Dose distribution detected by SPECT/CT in a patient with prostate cancer treated with 125I seeds: A case report. *Brachytherapy*, 15: S183–S184.

https://doi.org/10.1016/j.brachy.2016.04.337

65. Kono Y, Miyamoto Y, Oohashi S, *et al*., 2011, Radiation exposure to general public after permanent brachytherapy for prostate cancer. *Radiat Prot Dosimetry*, 146: 229–230.

https://doi.org/10.1093/rpd/ncr156

66. Herrera FG, Bourhis J, Coukos G, 2017, Radiotherapy combination opportunities leveraging immunity for the next oncology practice. *CA Cancer J Clin*, 67: 65–85.

https://doi.org/10.3322/caac.21358

67. Pencik J, Schlederer M, Gruber W, *et al*., 2015, STAT3 regulated ARF expression suppresses prostate cancer metastasis. *Nat Commun*, 6: 7736.

https://doi.org/10.1038/ncomms8736

68. Formenti SC, Demaria S, 2013, Combining radiotherapy and cancer immunotherapy: A paradigm shift. *J Natl Cancer Inst*, 105: 256–265.

https://doi.org/10.1093/jnci/djs629

69. Finkelstein SE, Salenius S, Mantz CA, *et al*., 2015, Combining immunotherapy and radiation for prostate cancer. *Clin Genitourin Cancer*, 13: 1–9.

https://doi.org/10.1016/j.clgc.2014.09.001

70. Du E, Wang L, Li CY, *et al*., 2017, Analysis of immune status after iodine-125 permanent brachytherapy in prostate cancer. *Onco Targets Ther*, 10: 2561–2567.

https://doi.org/10.2147/OTT.S137491

71. Ishihara D, Pop L, Takeshima T, *et al*., 2017, Rationale and evidence to combine radiation therapy and immunotherapy for cancer treatment. *Cancer Immunol Immunother*, 66: 281–298.

https://doi.org/10.1007/s00262-016-1914-6

72. Cabel L, Loir E, Gravis G, *et al*., Long-term complete remission with Ipilimumab in metastatic castrate-resistant prostate cancer: Case report of two patients. *J Immunother Cancer*, 5: 31.

https://doi.org/10.1186/s40425-017-0232-7

73. Tumeh PC, Harview CL, Yearley JH, *et al*., 2014, PD-1 blockade induces responses by inhibiting adaptive immune resistance. *Nature*, 515: 568–571.

https://doi.org/10.1038/nature13954

74. Arina A, Karrison T, Galka E, *et al*., 2017, Transfer of allogeneic CD4+ T cells rescues CD8+ T cells in anti-PD-L1-resistant tumors leading to tumor eradication. *Cancer Immunol Res*, 5: 127–136.

https://doi.org/10.1158/2326-6066.CIR-16-0293

75. Sallin MA, Sakai S, Kauffman KD, *et al*., 2017, Th1 differentiation drives the accumulation of intravascular, non-protective CD4 T cells during tuberculosis. *Cell Rep*, 18: 3091–3104.

https://doi.org/10.1016/j.celrep.2017.03.007

76. Hou PF, Zhu LJ, Chen XY, *et al*., Age-related changes in CD4+CD25+FOXP3+ regulatory T cells and their relationship with lung cancer. *PLoS One*, 12: e0173048.

https://doi.org/10.1371/journal.pone.0173048

77. Wang X, Liu Y, Dai L, *et al*., 2016, Foxp3 downregulation in NSCLC mediates epithelial-mesenchymal transition via NF-kappaB signaling. *Oncol Rep*, 36: 2282–2288.

https://doi.org/10.3892/or.2016.5024

78. Wada S, Harris TJ, Tryggestad E, *et al*., Combined treatment effects of radiation and immunotherapy: Studies in an autochthonous prostate cancer model. *Int J Radiat Oncol Biol Phys*, 87: 769–776.

https://doi.org/10.1016/j.ijrobp.2013.07.015

79. Nardone V, Botta C, Caraglia M, *et al*., 2016, Tumor infiltrating T lymphocytes expressing FoxP3, CCR7 or PD-1 predict the outcome of prostate cancer patients subjected to salvage radiotherapy after biochemical relapse. *Cancer Biol Ther*, 17: 1213–1220.

https://doi.org/10.1080/15384047.2016.1235666

80. Harris TJ, Hipkiss EL, Borzillary S, *et al*., 2008, Radiotherapy augments the immune response to prostate cancer in a time-dependent manner. *Prostate*, 68: 1319–1329.

https://doi.org/10.1002/pros.20794

81. Mittal D, Gubin MM, Schreiber RD, *et al*., 2014, New insights into cancer immunoediting and its three component phases--elimination, equilibrium and escape. *Curr Opin Immunol*, 27: 16–25.

https://doi.org/10.1016/j.coi.2014.01.004

ACCSCIENCE PUBLISHING

Advances in Radiotherapy & Nuclear Medicine

REVIEW ARTICLE

Fibroblast activation protein-targeted radioligand therapy in various types of cancer: Background, clinical studies, and future development

Yizhen Pang[1,2†], Liang Zhao[1,2†], Jianhao Chen[2], Weizhi Xu[3], Jiayu Cai[3], Haojun Chen[1,3*], and Qin Lin[1,2*]

[1]The School of Clinical Medicine, Fujian Medical University, Fuzhou, China

[2]Department of Radiation Oncology, Xiamen Cancer Center, Xiamen Key Laboratory of Radiation Oncology, the First Affiliated Hospital of Xiamen University, School of Medicine, Xiamen University, Xiamen, China

[3]Department of Nuclear Medicine and Minnan PET Center, Xiamen Key Laboratory of Development and Translation of Radiopharmaceuticals, The First Affiliated Hospital of Xiamen University, School of Medicine, Xiamen University, Xiamen, China

Abstract

Cancer is the leading cause of mortality worldwide. The proliferation and viability of cancer cells are intricately related to the complex tumor microenvironment in which they reside. Cancer-associated fibroblasts (CAFs) play a pivotal role in multiple stages of tumorigenesis, including tumor growth, invasion, metastasis, and resistance to treatment, through intricate crosstalk with tumor and immune cells. Targeted radionuclide therapy involves the systemic administration of small molecule drugs labeled with β-emitting or α-emitting radioisotopes, allowing precise targeting of tumor sites and delivering radiation directly to the tumor. Prostate-specific membrane antigen-targeted radioligand therapy (RLT) and somatostatin receptor-targeted peptide receptor radionuclide therapy (PRRT) have demonstrated favorable safety profiles and significant antitumor efficacy, leading to their approval by the Food and Drug Administration. Recently, the utilization of theranostic approaches that target overexpressed fibroblast activation proteins (FAPs) within the CAFs of the tumor stroma has demonstrated encouraging preliminary outcomes. This review aims to provide a concise summary of current clinical research outcomes and the applications of RLT based on FAP inhibitors in the context of solid tumors.

Keywords: Fibroblast activation proteins; Radioligand therapy; Immunotherapy; Synergistic effect

†These authors contributed equally to this work.

***Corresponding authors:**
Haojun Chen
(leochen0821@foxmail.com)
Qin Lin
(linqin05@163.com)

Citation: Pang Y, Zhao L, Chen J, *et al.*, 2023, Fibroblast activation protein-targeted radioligand therapy in various types of cancer: Background, clinical studies, and future development. *Adv Radiother Nucl Med,* 1(2): 1667
https://doi.org/10.36922/arnm.1667

Received: August 23, 2023

Accepted: September 19, 2023

Published Online: October 24, 2023

1. Introduction

Cancer is among the leading causes of mortality globally, with projections indicating that cancer-related deaths will surpass those caused by cardiovascular disease[1]. Current cancer treatment strategies typically involve a combination of chemotherapy, radiotherapy, and surgical interventions tailored to individual patient needs. Remarkably, over the past two decades, there has been minimal appreciable improvement in the average cancer

survival rate despite the use of conventional therapies[2]. Immunotherapy has ushered in a new era of tumor treatment, demonstrating promising efficacy. However, the effectiveness of these treatments is hindered by several obstacles, with drug resistance being a significant barrier that reduces the efficacy of chemotherapeutic agents[3]. Therefore, it is imperative to explore novel and alternative therapeutic approaches to address this challenge and improve treatments.

Recently, targeted radioligand therapy (TRT) has gained significant momentum and emerged as a promising avenue for treating various types of malignancies[4]. TRT is characterized by different β-emitting or α-emitting radionuclides of label-specific molecules, which are expressed or upregulated in tumors through the systemic administration of a radioactive drug, allowing precise targeting of tumor sites and delivering radiation directly to the tumor while sparing healthy tissues and organs[5]. Peptide receptor radionuclide therapy (PRRT) has been widely recognized as a highly effective and well-tolerated treatment approach for patients with neuroendocrine tumors (NETs) and was approved by the US Food and Drug Administration (FDA) in 2017. Moreover, in an international, randomized, open-label phase III study (NCT03511664, available from https://clinicaltrials.gov/ct2/show/NCT03511664), ^{177}Lu-PSMA-617 plus standard of care (SOC) treatment was a well-tolerated regimen. This approach has improved radiographic progression-free survival (rPFS) and prolonged overall survival (OS) compared to SOC alone in men with advanced-stage prostate-specific membrane antigen (PSMA)-positive metastatic castration-resistant prostate cancer (mCRPC), supporting its adoption as an SOC and receiving FDA approval in 2022[6]. Nevertheless, the absence of pan-tumor targets poses a challenge to the widespread adoption of TRT. Therefore, identifying pan-tumor targets is a key to successful TRT application.

Cancer-associated fibroblasts (CAFs) are crucial and abundant constituents of the tumor microenvironment (TME) that plays a significant role in tumor progression, including tumorigenesis, angiogenesis, metastasis, immunosuppression, and developing drug resistance[7]. CAFs exhibit high fibroblast activation protein (FAP) expression, while normal organs and tissues display either no or low expression[8]. Consequently, several small FAP inhibitors (FAPIs) have been developed and used to visualize the tumor stroma by targeting FAP. FAPI has demonstrated superiority over 18F-fluorodeoxyglucose (^{18}F-FDG) in diagnosing various tumors[9,10], making it a novel method for tumor imaging and radioligand therapy. Several pre-clinical and clinical studies have explored the effect of FAP-TRT (RLT) on various malignancies. Preliminary results have demonstrated good safety across all studies and effectiveness to different degrees[11-13]. This review summarizes the latest pre-clinical and clinical findings regarding FAP-targeted RLT.

2. Non-radionuclide targeting of FAP as an antitumor therapy approach

Tumor tissues consist of tumor cells and the surrounding TME. The TME plays a vital role in tumor growth, progression, metastasis, and treatment outcomes, making it indispensable for the development of malignant tumors[7]. CAFs, which originate from normal fibroblasts activated by tumor cells, are essential components of the TME. They contribute to tumor cell survival, invasion, and metastasis[14]. CAFs can also arise through processes such as an epithelial-to-mesenchymal transition from non-fibroblastic cells or endothelial-to-mesenchymal transition from endothelial cells[15]. Notably, CAFs exhibit diverse functions, and while they often promote tumorigenesis, specific subsets of CAFs have shown significant tumor-suppressive effects[16].

CAFs can express receptors such as FAP, platelet-derived growth factor receptor β, and CD10. Among these, FAP, a type II transmembrane serine protease belonging to the dipeptidyl peptidase 4 family[17], has attracted increasing attention. Normal fibroblasts and tissues are characterized by the absence or low expression of FAP, making it a promising target for imaging and treatment[18,19]. Various strategies targeting FAP have been investigated for the treatment of colorectal and non-small-cell lung carcinomas, including anti-FAP monoclonal antibodies[20], FAP-antigen vaccination[21], suppression of FAP enzyme activity[22], and chimeric antigen receptor-T (CAR-T) cells specifically targeting FAP[23]. These therapies have been well-tolerated and deemed safe. Another potential approach involves anti-cytokine therapies targeting interleukin-6, C-X-C motif chemokine ligand 12, and transforming growth factor-β (TGF-β). These therapies aim to reduce the recruitment and activation of CAFs, thereby decreasing the secretion of cytokines and chemokines by CAFs[7]. The extracellular matrix (ECM) serves as a physical barrier to delivering tumor drugs. Strategies focusing on targeting the production of ECM proteins or promoting ECM degradation show promise in facilitating drug delivery and potentially enhancing cytotoxic effects in tumors[24]. Among these approaches, AVA6000 stands out as a FAP-activated prodrug of maytansinoid. It is expected to possess enhanced tumor-killing effects while minimizing systemic side effects (NCT04969835, available from https://clinicaltrials.gov/ct2/show/NCT04969835). While several

drugs have undergone testing, only a few pre-clinical studies have shown improved outcomes, and the efficacy of these drugs in clinical trials has been limited. The current status of targeting FAP for anti-CAF therapy remains at an early clinical trial stage[25]. Table 1 summarizes the different non-radionuclide-targeted therapeutic strategies against FAP available from clinicaltrials.gov.

3. FAP-targeted RLT as an antitumor therapy approach

In recent years, multiple small-molecule FAPIs and cyclic peptides targeting FAP (FAP-2286) have been designed for imaging purposes, facilitating the visualization of the tumor stroma (labeled with ^{68}Ga, ^{18}F, or ^{99m}Tc). Multiple studies have reported on the tumor uptake and biodistribution of FAPIs/FAP-2286[9,26,27]. For instance, Kratochwil *et al*. conducted an evaluation involving 80 patients with 28 different tumor entities (54 primary tumors and 229 metastases). This evaluation employed ^{68}Ga-FAPI positron emission tomography/computed tomography (PET/CT)[9]. The results revealed that esophageal, breast, cholangiocarcinoma, sarcoma, and lung cancers exhibited higher ^{68}Ga-FAPI uptake, leading to elevated tumor-to-background ratios (TBR). Chen *et al*. conducted a study involving ^{68}Ga-FAPI PET/CT to diagnose primary and metastatic lesions in 74 patients with 12 different tumor types, comparing it with ^{18}F-FDG PET/CT[10]. Their findings demonstrated that ^{68}Ga-FAPI PET/CT excelled in identifying malignancies, boasting favorable TBR, and outperformed ^{18}F-FDG PET/CT in diagnosing primary and metastatic lesions. Pang *et al*. also explored the usefulness of ^{68}Ga-FAP-2286 PET/CT in imaging various malignancies, conducting a comparative analysis with ^{18}F-FDG and ^{68}Ga-FAPI-46 PET/CT[28]. Their results indicated that ^{68}Ga-FAP-2286 may offer a superior alternative to ^{18}F-FDG, particularly for cancer types characterized by low-to-moderate ^{18}F-FDG uptake, including gastric, pancreatic, and hepatic cancers. In addition, ^{68}Ga-FAP-2286 demonstrated longer tumor retention than ^{68}Ga-FAPI-46 at later time points. Figure 1 shows the representative PET images of 7 patients with diverse tumor types who underwent ^{18}F-FDG PET, ^{68}Ga-FAPI-46 PET, and ^{68}Ga-FAP-2286 PET imaging in a week or less. These results suggest that 68Ga-FAP-2286 is a promising candidate for pan-tumor TRT. Consequently, therapeutic radionuclides labeled with FAPI, peptides, and small-molecule radioconjugates targeting FAP have gained popularity in pre-clinical and clinical antitumor

Table 1. Summary of trials of non-radionuclide targeted therapeutic strategies against fibroblast activation protein (FAP)

Trial registration no. and medicine	Phase	Type of tumor	Study start	Study completion	Enrollment
NCT03932565: Enfortumab Vedotin	Phase 1	Nectin4-positive advanced malignant solid tumor	February 13 2019 (actual)	December 31 2021 (estimated)	30 (estimated)
NCT01722149: Adoptively transferred FAP-specific CD8 positive re-directed T cells	Early phase 1	Malignant pleural mesothelioma with pleural effusion	February 19 2015 (actual)	July 18 2019 (estimated)	4 (estimated)
NCT05098405: MP0317	Phase 1	Relapsed/refractory advanced solid tumors	October 11 2021 (actual)	2024 – 2004 (estimated)	78 (estimated)
NCT04969835: AVA6000	Phase 1	Locally advanced (unresectable) and/or metastatic solid tumors	July 16 2021 (actual)	June 30 2023 (estimated)	80 (estimated)
NCT02558140: RO6874813	Phase 1	Locally advanced or metastatic solid tumors	October 11 2015 (actual)	November 06 2017 (actual)	120 (actual)
NCT04857138: RO7300490	Phase 1	Advanced and/or metastatic solid tumor	May 18 2021 (actual)	August 17 2026 (estimated)	280 (estimated)
NCT03875079: RO6874281	Phase 1	Advanced or metastatic melanoma	June 24 2019 (actual)	July 14 2022 (actual)	83 (actual)
NCT04826003: RO7122290	Phase 1, Phase 2	Previously treated, metastatic, microsatellite-stable colorectal adenocarcinoma with high CEACAM5 expression	July 14 2021 (actual)	July 31 2025 (estimated)	80 (estimated)
NCT03386721:RO6874281	Phase 2	Advanced and/or metastatic solid tumors	February 19 2018 (actual)	December 30 2021 (actual)	256 (actual)

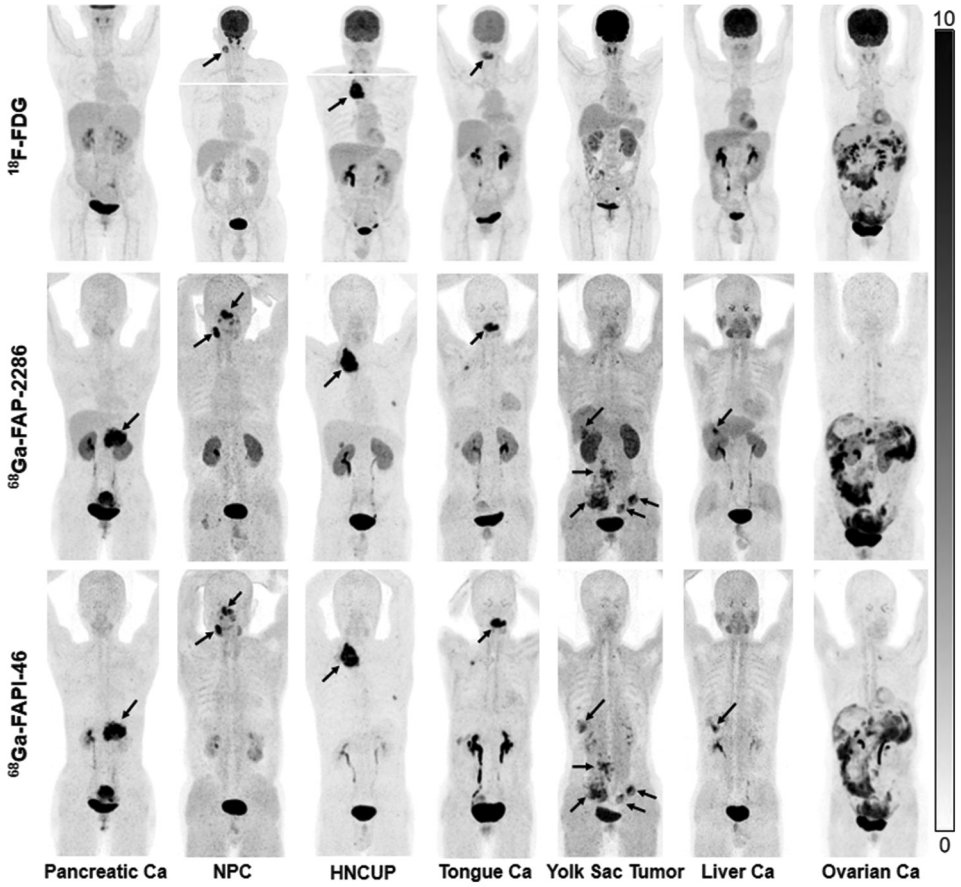

Figure 1. Representative PET images of seven patients with different types of tumors undergoing ^{18}F-FDG PET, ^{68}Ga-FAPI-46 PET, and ^{68}Ga-FAP-2286 PET imaging within <1 week[28]. Image reprinted with permission, Copyright © 2023, Yizhen Pang *et al.*
Abbreviations: PET: Positron emission tomography; Ca: Carcinoma; FAP: Fibroblast activation proteins; FAPI: Fibroblast activation protein inhibitor; FDG: Fluorodeoxyglucose; HNCUP: Head-and-neck carcinoma of unknown primary; NPC: Nasopharyngeal carcinoma.

studies. Table 2 summarizes various FAP-targeting radiopharmaceuticals currently employed in clinical imaging and therapeutic studies.

4. Insights from pre-clinical studies of FAP-targeted RLT

Pre-clinical *in vitro* and animal studies have been conducted to faithfully replicate the intended biological impact of a drug. These studies enable the assessment of efficacy, safety, and potential toxicities, covering aspects such as pharmacokinetics, pharmacodynamics, administration routes, dosing, and side effects. Despite safety testing in animal models, it is noteworthy that human drug trials have reported high failure rates associated with toxicity[29].

The key to TRT lies in understanding the pharmacokinetics of the radioactive ligands. The pharmacokinetic pre-requisites for therapeutic radiopharmaceuticals include prolonged circulation in the bloodstream, serum stability, reduced non-specific uptake, and sustained retention in the tumor. These characteristics result in a prolonged effective half-life and tumor radiation dose, ultimately minimizing radiation exposure to healthy surrounding tissues and reducing systemic toxicity. This, in turn, allows for the possibility of administering higher doses to patients.

Since 2018, several pre-clinical studies have been conducted to investigate changes in the structure and properties of FAPI radiopharmaceuticals. Lindner *et al.* determined that among 15 different FAPIs (ranging from FAPI-02 to FAPI-15), FAPI-04 shows promise as a tracer for clinical applications based on a comparison of *in vivo* pharmacokinetics in pre-clinical studies[11]. In a pre-clinical study, a single administration of ^{225}Ac-FAPI-04 demonstrated the ability to delay the growth of tumors carrying PANC-1 xenografts in mice, all while showing no significant changes in the mice's body weight[30]. Given the relatively short tumor retention times observed

Table 2. Summary of fibroblast activation protein (FAP)-targeting radiopharmaceuticals

FAP-targeting radiopharmaceuticals in imaging studies	
^{68}Ga-tracers	^{68}Ga-FAPI-04
	^{68}Ga-FAPI-46
	^{68}Ga-FAPI-74
	^{68}Ga-DOTA-2P (FAPI)$_2$
	^{68}Ga-OncoFAP-DOTAGA
	^{68}Ga-FAPI NOS
	^{68}Ga-FAPI-02
	^{68}Ga-DOTA-SA-FAPi
	^{68}Ga-DATA5m-SA-FAPi
	^{68}Ga-FAP-2286
^{18}F-tracers	^{18}F-AlF-NOTA-FAPI
	^{18}F-FAPI-74
	^{18}F-FAPI-NOS
	^{18}F-FAPI-42
	^{18}F-AlF-P-FAPI
^{99m}Tc-tracers	^{99m}Tc-FAPI-34
FAP-targeting radiopharmaceuticals in radionuclide therapy studies	
^{177}Lu-radionuclides	^{177}Lu-FAPI-46
	^{177}Lu-FAPI-04
	^{177}Lu-DOTA-SA-FAPi
	^{177}Lu-FAPI-2286
^{90}Y-radionuclides	^{90}Y-FAPI-46
	^{90}Y-FAPI-04
^{153}Sm-radionuclides	^{153}Sm-FAPI-04

with FAPI-02 and FAPI-04, Loktev *et al.* embarked on the development of several other derivatives[31]. Their investigation led to the discovery that FAPI-46 exhibited superior pharmacokinetics when compared to FAPI-04. Notably, FAPI-46 displayed higher 24-h tumor retention and lower physiological uptake. While FAPI-21 demonstrated the highest tumor retention after 24 h, unfortunately, it also exhibited high physiological uptake in the oral mucosa, thyroid, and salivary glands[31]. Moreover, the incorporation of the 1,4,7,10-tetraazacyclododecane-1,4,7,10-tetraacetic acid (DOTA) ligand as a chelator for FAPI-46 made it compatible with the labeling ^{90}Y, ^{177}Lu, and ^{153}Sm radionuclides, rendering it suitable for TRT[12,32-34]. Researchers have leveraged the multimerization effect to design and synthesize radiopharmaceuticals with improved properties. Zhao *et al.* linked two FAPI-46 monomer motifs to create DOTA-2P(FAPI)$_2$[35], while Pang *et al.* synthesized DOTA-4P(FAPI)$_4$ using four FAPI-46 monomers[36]. The application of multimerization techniques has been shown to increase tumor uptake and retention, consequently enhancing the antitumor effect[36,37]. Moon *et al.* took a different approach by transforming FAPI-04 into a dimeric system, resulting in DOTA (SA.FAPI)$_2$ and DOTAGA (SA.FAPI)[38]. In addition to these developments, a cyclic peptide known as FAP-2286 has been designed specifically for FAP-based radionuclide therapy. This peptide has demonstrated higher tumor uptake, lower background signal, prolonged tumor retention time, and remarkable antitumor effects[39]. Furthermore, albumin binder-truncated Evans blue (^{177}Lu-EB-FAPI-B1) has demonstrated favorable pharmacokinetics and significant antitumor effects[40]. The introduction of albumin-binding FAPIs has contributed to increased blood drug concentrations, delayed excretion, stability in physiological saline and plasma, high FAP-binding affinity, and minimal physiological uptake[41].

Another crucial aspect of TRT is the selection of the appropriate radionuclide. The radiation dose delivered to a target relies on the type, range, half-life, and energy of the particles emitted. α-particle-based treatments have demonstrated effectiveness in targeting CAFs, although their direct impact on tumor cells may be limited. In a pre-clinical study, a single dose of ^{225}Ac-FAPI-04 resulted in tumor growth retardation in mice bearing PANC-1 xenografts, with no significant changes in body weight[30]. Tranel *et al.* conducted a study comparing absorbed dose estimates in a three-dimensional cell model consisting of a mixture of CAFs and tumor cells[42]. Their findings revealed that the efficacy of ^{225}Ac decreased with increasing tumor cluster size. In such cases, ^{177}Lu, which emits β-emitters with a more extended range, might be a more effective option due to crossfire effects. However, the efficacy of ^{177}Lu is also limited when dealing with large cluster sizes (0.6–0.7 mm)[42]. In addition, the use of other radionuclides, such as ^{90}Y and ^{131}I, for labeling FAPIs could provide additional treatment options for tumors.

5. Initial findings from clinical studies on FAP-targeted RLT

At present, our knowledge of human FAP-targeted RLT is primarily derived from case reports, case series, and small-scale prospective studies (Table 3)[11-13,32-34,43-50]. These investigations employed various FAPI agents, including FAPI-04, FAPI-46, FAP-2286, 3BP-3940, and (SA.FAPi)$_2$ in combinations with radionuclides such as ^{90}Y, ^{177}Lu, ^{153}Sm, and ^{225}Sc. While most studies included patients with various malignancies, Ballal *et al.* specifically focused on patients with thyroid cancer[51]. Early studies reported disease progression or stable disease[32,44,45], while recent studies have revealed partial responses by patients to new therapies[12,49]. The first documented case of FAP-targeted RLT was reported by Lindner *et al.*[11],

Table 3. Summary of the studies involving human fibroblast activation protein inhibitor (FAPI)-based radionuclide therapy

Study (Country)	Tracers	Injected activity	No. of patients	Type of cancer (no. of patients)	Response (RECIST)	Adverse events
Lindner *et al.*[11] (Germany)	^{90}Y-FAPI-04	2.9 GBq, 1 cycle	2	Breast cancer (2)	NA	None
Lindner *et al.*[12] (Germany)	^{90}Y-FAPI-46	6 GBq, 2 cycles	2	Pancreatic cancer (1), ovarian cancer (1)	NA	NA
Jokar *et al.*[43] (Iran)	^{177}Lu-FAPI-46	3.7 GBq, 2 cycles	1	Breast cancer (1)	NA	NA
Rathke *et al.*[32] (Germany)	^{90}Y-FAPI-46	7.4 GBq (Cumulative 28.1 GBq), 4 cycles	1	Breast cancer (1)	PD	NA
Assadi *et al.*[44] (Iran)	^{177}Lu-FAPI-46	3.7 GBq (1.85–13.7 GBq), 36 cycles	18	Ovarian cancer (2), sarcomas (1), colon cancer (3), breast cancer (5), pancreatic cancer (2), prostate cancer (2), cervical cancer (1), lung cancer (1), thyroid cancer (1)	12 SD, 6 PD	Anemia G3 (1); leukopenia G1 (1); thrombocytopenia G1 (1)
Ballal *et al.*[45] (India)	^{177}Lu-DOTA.SA.FAPI; ^{177}Lu-DOTAGA.(SA.FAPI)$_2$	2.96 GBq SA.FAPI and 1.48 GBq (SA.FAPI)$_2$, 17 cycles	10	Thyroid cancer (5), breast cancer (4), paraganglioma (1)	SA.FAPIPD (SA.FAPi)$_2$ clinical response	Anemia G3 (1); thrombocytopenia G1 (1)
Ballal *et al.*[13] (India)	^{177}Lu-DOTA.SA.FAPi	3.2 GBq, 1 cycle	1	Breast cancer (1)	NA	NA
Ballal *et al.*[51] (India)	^{177}Lu-DOTAGA.(SA.FAPI)$_2$	8.2±2.7 GBq, 45 cycles	15	Thyroid cancer (15)	4 PR, 3 SD, others NA	Diarrhea G1 (1)
Kuyumcu *et al.*[46] (Turkey)	^{177}Lu-FAPI-04	267.5±8.6 GBq, 4 cycles	4	Breast cancer (1), thymic carcinoma (1), thyroid cancer (1), ovarian cancer (1)	NA	NA
Kratochwil *et al.*[33] (Germany)	^{153}Sm-FAPI-46, ^{90}Y-FAPI-46	20 GBq ^{153}Sm-FAPI-46, and 8 GBq ^{90}Y-FAPI-46	1	Soft tissue sarcoma (1)	SD	NA
Fu *et al.*[34] (China)	^{177}Lu-FAPI-46	3.7 GBq, 1 cycle	1	Nasopharyngeal carcinoma (1)	PD, mixed response	None
Baum *et al.*[47] (Germany)	^{177}Lu-FAP-2286	5.8±2.0 GBq, 22 cycle	11	Pancreatic cancer (5), breast cancer (4), rectum tumor (1), ovary cancer (1)	9 PD, 2 SD	Headache G1 (4), G2 (4); Anemia G1 (1), G2 (2); leukopenia G2 (2), G3 (1); pancytopenia (1); pain flare-up G3 (1)
Ferdinandus *et al.*[48] (Germany)	^{90}Y-FAPI-46	3.8 GBq in the 1st cycle and 7.4 GBq in the 2nd cycle	9	Pancreatic cancer (3), Sarcomas (4), chordoma (1), neuroendocrine tumor (1)	4 PD, 4 SD, 1 NA	Anemia G1 (2), G2 (2) and G3 (4); renal G (1), G2 (1) and liver G1 (1), G2 (12), G3 (1), G4 (1); pancreatobiliary G1 (1), G3 (1), G4 (1)
Fendler *et al.*[49] (Germany)	^{90}Y-FAPI-46	3.7–7.4 GBq, 47 cycles	21	Sarcoma (16), pancreatic cancer (3), prostate cancer (1), gastric cancer (1)	1 PR, 8 PD, 7 SD, and others NA	Anemia G3 (6); thrombocytopenia G3 (6)
Fu *et al.*[72] (China)	^{177}Lu-FAPI-46	5.55 GBq (cumulative 16.7 GBq), 4 cycles	1	Thyroid cancer (1)	SD	Pain flare-up
Kaghazchi *et al.*[50] (Iran)	^{177}Lu-FAPI-46	1.85 GBq, 1 cycle	1	Pancreatic cancer (1)	PR	Pain flare-up
Rao *et al.*[73] (China)	^{177}Lu-FAP-2286	7.0 GBq, 1 cycle	1	Lung squamous cell carcinoma (1)	PR	None

Abbreviations: NA: Not available; PD: Progressive disease; PR: Partial response; RECIST: Response Evaluation Criteria in Solid Tumors; SD: Stable disease.

who reported a case involving a patient with last-stage breast cancer bone metastasis, treated with ^{90}Y-labeled FAPI-04. Following treatment with 2.9 GBq ^{90}Y-FAPI-04, the patients experienced symptom improvement with no signs of toxicity[11]. Another notable case was presented by Ballal *et al*., where ^{177}Lu-DOTA.SA.FAPi radionuclide therapy was administered to an end-stage breast cancer patient (a single cycle of 3.2 GBq). This treatment reduced symptom intensity without any treatment-related adverse events[13]. At the 18-month mark following TRT, Fendler *et al*. conducted a follow-up study on patients who had undergone FAP-targeted RLT, monitored through FDG PET/CT scans. Disease status was assessed based on the RECIST/PERCIST criteria. The results revealed that patients who exhibited a partial response or had stable disease following ^{90}Y-FAPI-46 therapy exhibited a significantly longer median survival than those with progressive disease (14.4 vs. 6.6 months)[49]. While none of the patients achieved a complete response following FAP-targeted RLT, promising results have been reported in the literature. Notably, this therapy has shown a generally favorable safety profile, with minimal toxicity and no reported allergic reactions. Several studies have identified grades 3 and 4 hematological and hepatobiliary toxicities[47-49]. The interpretation of these toxicities should be approached cautiously, considering the inclusion of heavily pre-treated patients with metastases. Nevertheless, repeat therapy is feasible and safe. Figure 2 shows PET and single-photon emission computed tomography (SPECT) images of a 25-year-old man with known nasopharyngeal carcinoma (NPC) who received experimental therapy with 3.7 GBq of ^{177}Lu-FAPI-46.

6. FAP-targeted RLT combined with immunotherapy for a synergistic effect

Cancer immunotherapy, specifically the use of immune checkpoint inhibitors (ICIs) targeting programmed cell death 1 (PD-1)/programmed cell death ligand 1 (PD-L1), has firmly established itself as a fundamental approach in the fight against cancer[52]. ICIs have significantly improved survival rates across various cancer types and are regarded as a significant advancement in cancer treatment[53]. Nevertheless, the clinical efficacy of ICIs is hindered by intrinsic and acquired tumor resistance, restricting their widespread application in cancer treatment[54]. Resistance to ICIs is partly attributed to the presence of immunosuppressive cells within the TME, including CAFs expressing FAP[55]. CAFs can secrete various immunosuppressive factors, such as TGF-β and IL-10, which have the potential to inhibit the activity of immune cells and limit their ability to target tumors[56]. These factors can suppress the effectiveness of immunotherapy, weakening the patient's immune response against the tumor. Furthermore, CAFs produce ECM within the TME. The ECM forms a tissue structure that supports tumor growth and migration. ECM remodeling may restrict the infiltration and activity of immune cells, thereby reducing the tumor's visibility to the immune system[57]. Consequently, immune cells encounter greater difficulty reaching the tumor area, compromising the efficacy of immunotherapy.

Numerous ongoing clinical trials investigating non-radionuclide-targeting CAF/FAP therapies have proposed combinations of therapeutic approaches (Table 1). These studies have explored the simultaneous use of multiple strategies to improve therapeutic outcomes. The findings from these clinical trials hold the potential to revolutionize the management of advanced tumors. However, as of yet, no clinical trials have reported promising results. One possible reason for this lack of success may be the limited efficacy of non-radionuclide-targeting CAF/FAP therapy, which could impede its ability to synergize effectively with other treatment modalities in combination therapy.

External beam radiation therapy (EBRT) is among the most extensively used therapeutic modalities in clinical tumor management[58]. EBRT represents a standard and effective treatment approach for various types of cancers, with the goal of precisely targeting and eliminating cancer cells using high-precision radiation while minimizing damage to surrounding healthy tissues[59]. EBRT can induce double-stranded DNA breaks, which exhibit lower repair rates and do not rely on oxygen availability. Previous studies have demonstrated that both EBRT and TRT can induce DNA damage, triggering the upregulation of pro-inflammatory cytokines, including interferons, through the activation of the stimulator of the interferon genes (STING) pathway[60]. These cytokines play a pivotal role in attracting immunostimulatory immune cells to the TME, such as T cells, antigen-presenting cells, and natural killer cells[61]. Simultaneously, they can hinder the activity of immunosuppressive immune cells, including regulatory T cells[62]. At present, there is substantial pre-clinical and clinical evidence showing that EBRT can enhance the response of both immunologically "hot" and "cold" tumors to anti-PD-1 and anti-cytotoxic T lymphocyte-associated protein 4 (anti-CTLA-4) immune checkpoint inhibition[63]. The combination of EBRT and immunotherapy exhibits a synergistic antitumor effect[63]. For many patients with metastatic cancer, providing low-dose immune-modulating radiation therapy to all tumors using EBRT is not feasible. This is due to the inability to target radiographically occult sites, along with the toxicity associated with large-field or whole-body radiation, lymphocyte depletion, and

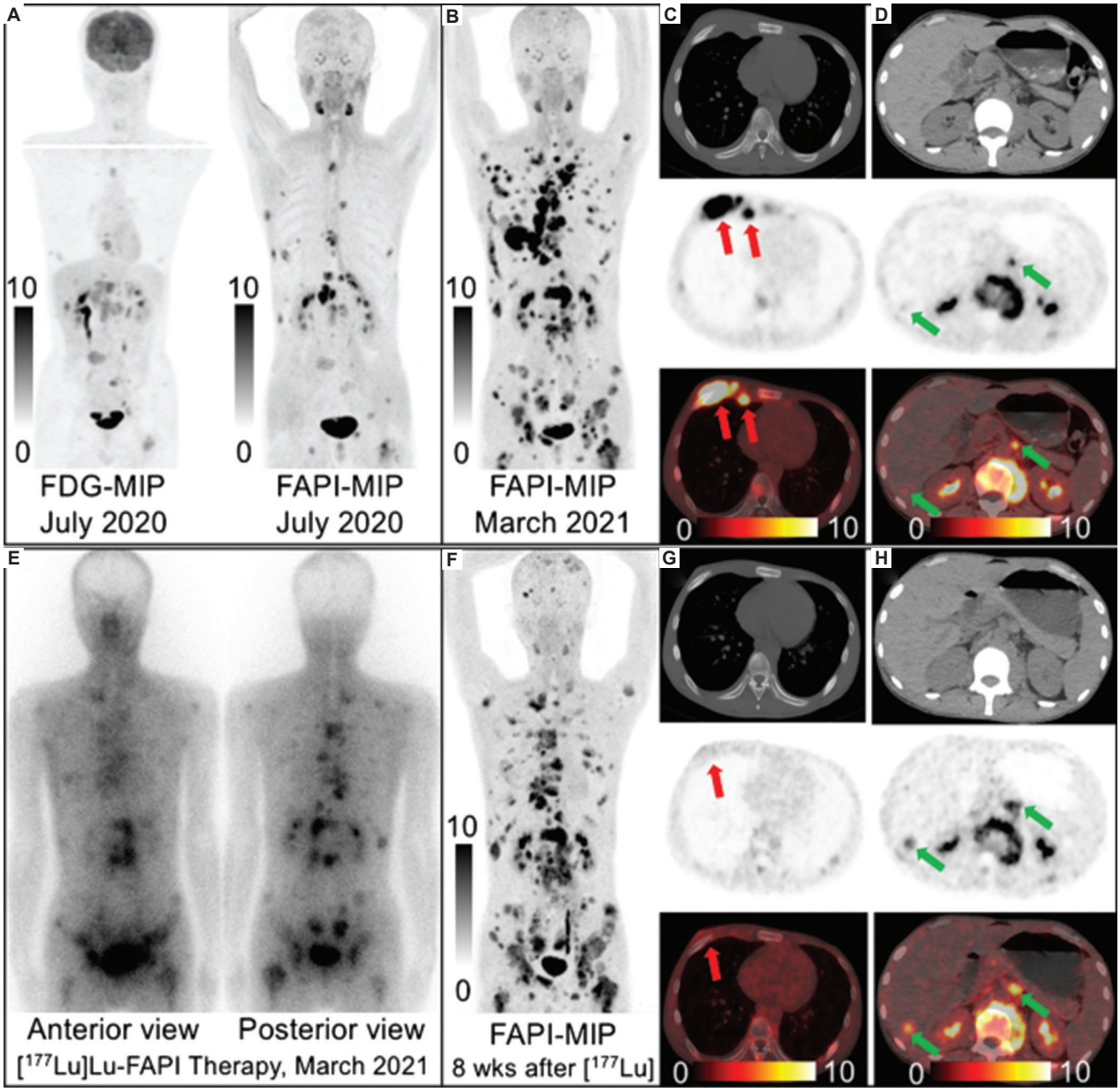

Figure 2. Radiology of a 25-year-old man diagnosed with nasopharyngeal carcinoma. (A) The ^{18}F-FDG and ^{68}Ga-FAPI-46 PET/CT images revealed multiple lymph node and bone metastases, and ^{68}Ga-FAPI-46 PET/CT showed a greater number of metastatic lesions than ^{18}F-FDG in July 2020. Due to the lack of other available treatment choices, the patient participated in a clinical trial for ^{177}Lu-FAPI-46 radionuclide therapy (NCT04849247). (B–D) A ^{68}Ga-FAPI-46 PET/CT was performed before radionuclide treatment, which showed intense radiotracer uptakes in most metastatic lesions. (E) Intense ^{177}Lu-FAPI-46 uptake was observed in most metastatic lesions on post-therapeutic scintigraphy at 2 h post-injection. (F–H) Follow-up ^{68}Ga-FAPI-46 PET/CT was performed 8 weeks after radionuclide therapy, which showed a mixed response: regression in some lesions but progressive disease in other lesions[34]. Image reprinted with permission, Copyright © 2022, Kaili Fu *et al.*

Abbreviations: PET: Positron emission tomography; FAPI: Fibroblast activation protein inhibitor; FDG: Fluorodeoxyglucose; MIP: Maximum intensity projection; PET/CT: Positron emission tomography/computed tomography.

related systemic immune suppression[61]. Similar to EBRT, TRT can also induce DNA double-strand breaks through radiation effects because of its ability to deposit higher energy within a shorter particle range, resulting in higher linear energy transfer[64]. However, unlike EBRT, TRT can be administered systemically to reach multiple metastatic lesions throughout the body and exert therapeutic effects through radiation[65].

Several pre-clinical studies have investigated the efficacy of TRT combined with immunotherapy, consistently demonstrating the capacity of this combination to enhance the immune response, improve the efficacy of immunotherapy, and achieve superior overall outcomes compared to the use of either immunotherapy or TRT alone[66,67]. Choi *et al.* conducted an investigation into the efficacy of TRT (^{177}Lu-LLP2A) when combined with dual immunotherapy (anti-PD-1 + anti-CTLA-4 or anti-PD-L1 + anti-CTLA-4) using a murine melanoma model[67]. In a separate study, Chen *et al.* explored the optimal timing and potential mechanisms of TRT (^{177}Lu-EB-RGD) when administered in conjunction with immunotherapy (anti-PD-L1 antibody) in a mouse model of colon cancer[66]. Czernin *et al.* confirmed that the combination of TRT (^{225}Ac-PSMA617) with immunotherapy (anti-PD-1 antibody) led to synergistic improvements in therapeutic outcomes in C57BL/6 mouse models of prostate cancer[68]. Furthermore, a recent report by Esfahani *et al.* reported improved treatment responses through the combination of PRRT (^{177}Lu-DOTATATE) and immunotherapy (anti-PD-1 antibody) in NET-bearing mice[69]. These collective findings underscore the potential for a synergistic effect when TRT and immunotherapy are combined. A previous study identified that the depletion of FAP-positive CAFs enhanced the antitumor effect of PD-L1 immunotherapy. In an autochthonous model of pancreatic ductal adenocarcinoma, T-cell infiltration has been demonstrated to reduce cancer cell growth[70]. This reduction in cancer cells suggests that the combination of FAP-targeted RLT with immunotherapy has the potential to enhance the immune response, thereby improving antitumor efficacy. However, only one pre-clinical study, conducted by Zboralski *et al.*, has investigated whether the combination of FAP-targeted RLT and immunotherapy could generate a synergistic effect, resulting in a treatment outcome where 1 + 1 >2[71]. The results of this pre-clinical study demonstrated that FAP-targeted RLT enhanced anti-PD-1-mediated inhibition of tumor growth by modulating the TME and increasing the recruitment of tumor-infiltrating CD8+ T cells. These findings provide a compelling rationale for conducting clinical studies involving a combination of FAP-targeted RLT and immunotherapy in FAP-positive tumors. By modulating the TME and enhancing the recruitment of tumor-infiltrating CD8+ T cells, this approach offers promising prospects for improved therapeutic outcomes.

7. Conclusion

FAP-targeted RLT has shown promising results in clinical and pre-clinical studies. Furthermore, combining FAP-targeted RLT with immunotherapy has demonstrated synergistic effects in pre-clinical studies, leading to a more robust immune response and improved antitumor efficacy. Therefore, the utilization of FAP-targeted RLT, either alone or in combination with immunotherapy or chemotherapy, holds significant promise for the future of cancer treatment. Nonetheless, comprehensive clinical trials will be essential in the future to ascertain the effectiveness of combining FAP-targeted RLT with immunotherapy or chemotherapy.

Acknowledgments

None.

Funding

This work was funded by the National Natural Science Foundation of China (Grant number: 82071961), Fujian Research and Training Grants for Young and Middle-aged Leaders in Healthcare, Key Scientific Research Program for Yong Scholars in Fujian (Grant number: 2021ZQNZD 016), Fujian Natural Science Foundation for Distinguished Yong Scholars (Grant number: 2022D005), Natural Science Foundation of Fujian Province (Grant number: 2020J011220), Key Medical and Health Projects in Xiamen (Grant number: 3502Z20209002), Xiamen Key Laboratory of Radiopharmaceuticals, Xiamen Key Laboratory of Radiation Oncology, Xiamen Clinical Research Center for Head and Neck Cancer, and 2021 National Clinical Key Specialty (Oncology, Grant number: 3210013).

Conflict of interest

The authors declare that they have no conflicts of interest.

Author contributions

Conceptualization: Haojun Chen, Qin Lin
Writing – original draft: Yizhen Pang, Liang Zhao
Writing – review & editing: Jianhao Chen, Weizhi Xu, Jiayu Cai

Ethics approval and consent to participate

Not applicable.

Consent for publication

Not applicable.

Availability of data

The datasets used and/or analyzed during the present study are available from the corresponding author upon reasonable request.

References

1. Kim KJ, Kim KJ, Choi J, *et al.*, 2023, Linear association between radioactive iodine dose and second primary malignancy risk in thyroid cancer. *J Natl Cancer Inst*,

115: 695–702.

https://doi.org/10.1093/jnci/djad040

2. Paskeh MDA, Entezari M, Mirzaei S, *et al*., 2022, Emerging role of exosomes in cancer progression and tumor microenvironment remodeling. *J Hematol Oncol*, 15: 83.

https://doi.org/10.1186/s13045-022-01305-4

3. Morad G, Helmink BA, Sharma P, *et al*., 2021, Hallmarks of response, resistance, and toxicity to immune checkpoint blockade. *Cell*, 184: 5309–5337.

https://doi.org/10.1016/j.cell.2021.09.020

4. Morris ZS, Wang AZ, Knox SJ, 2021, The radiobiology of radiopharmaceuticals. *Semin Radiat Oncol*, 31: 20–27.

https://doi.org/10.1016/j.semradonc.2020.07.002

5. Langbein T, Weber WA, Eiber M, 2019, Future of theranostics: An outlook on precision oncology in nuclear medicine. *J Nucl Med*, 60: 13S–19S.

https://doi.org/10.2967/jnumed.118.220566

6. Fallah J, Agrawal S, Gittleman H, *et al*., 2023, FDA approval summary: Lutetium Lu 177 vipivotide tetraxetan for patients with metastatic castration-resistant prostate cancer. *Clin Cancer Res*, 29: 1651–1657.

https://doi.org/10.1158/1078-0432.CCR-22-2875

7. Chen X, Song E, 2019, Turning foes to friends: Targeting cancer-associated fibroblasts. *Nat Rev Drug Discov*, 18: 99–115.

https://doi.org/10.1038/s41573-018-0004-1

8. Hamson EJ, Keane FM, Tholen S, *et al*., 2014, Understanding fibroblast activation protein (FAP): Substrates, activities, expression and targeting for cancer therapy. *Proteomics Clin Appl*, 8: 454–463.

https://doi.org/10.1002/prca.201300095

9. Kratochwil C, Flechsig P, Lindner T, *et al*., 2019, ^{68}Ga-FAPI PET/CT: Tracer uptake in 28 different kinds of cancer. *J Nucl Med*, 60: 801–805.

https://doi.org/10.2967/jnumed.119.227967

10. Chen H, Pang Y, Wu J, *et al*., 2020, Comparison of [^{68}Ga]Ga-DOTA-FAPI-04 and [^{18}F] FDG PET/CT for the diagnosis of primary and metastatic lesions in patients with various types of cancer. *Eur J Nucl Med Mol Imaging*, 47: 1820–1832.

https://doi.org/10.1007/s00259-020-04769-z

11. Lindner T, Loktev A, Altmann A, *et al*., 2018, Development of quinoline-based theranostic ligands for the targeting of fibroblast activation protein. *J Nucl Med*, 59: 1415–1422.

https://doi.org/10.2967/jnumed.118.210443

12. Lindner T, Altmann A, Kramer S, *et al*., 2020, Design and development of ^{99m}Tc-labeled FAPI tracers for SPECT imaging and ^{188}Re therapy. *J Nucl Med*, 61: 1507–1513.

https://doi.org/10.2967/jnumed.119.239731

13. Ballal S, Yadav MP, Kramer V, *et al*., 2021, A theranostic approach of [^{68}Ga]Ga-DOTA.SA.FAPi PET/CT-guided $^{[177}$Lu$^{]}$Lu-DOTA.SA.FAPi radionuclide therapy in an end-stage breast cancer patient: New frontier in targeted radionuclide therapy. *Eur J Nucl Med Mol Imaging*, 48: 942–944.

https://doi.org/10.1007/s00259-020-04990-w

14. Ohlund D, Elyada E, Tuveson D, 2014, Fibroblast heterogeneity in the cancer wound. *J Exp Med*, 211: 1503–1523.

https://doi.org/10.1084/jem.20140692

15. Mer AS, Ba-Alawi W, Smirnov P, *et al*., 2019, Integrative pharmacogenomics analysis of patient-derived xenografts. *Cancer Res*, 79: 4539–4550.

https://doi.org/10.1158/0008-5472.CAN-19-0349

16. Ozdemir BC, Pentcheva-Hoang T, Carstens JL, *et al*., 2014, Depletion of carcinoma-associated fibroblasts and fibrosis induces immunosuppression and accelerates pancreas cancer with reduced survival. *Cancer Cell*, 25: 719–734.

https://doi.org/10.1016/j.ccr.2014.04.005

17. Rettig WJ, Su SL, Fortunato SR, *et al*., 1994, Fibroblast activation protein: Purification, epitope mapping and induction by growth factors. *Int J Cancer*, 58: 385–392.

https://doi.org/10.1002/ijc.2910580314

18. Zhao L, Chen J, Pang Y, *et al*., 2022, Fibroblast activation protein-based theranostics in cancer research: A state-of-the-art review. *Theranostics*, 12: 1557–1569.

https://doi.org/10.7150/thno.69475

19. Ora M, Soni N, Nazar AH, *et al*., 2023, Fibroblast activation protein inhibitor-based radionuclide therapies: Current status and future directions. *J Nucl Med*, 64: 1001–1008.

https://doi.org/10.2967/jnumed.123.265594

20. Ostermann E, Garin-Chesa P, Heider KH, *et al*., 2008, Effective immunoconjugate therapy in cancer models targeting a serine protease of tumor fibroblasts. *Clin Cancer Res*, 14: 4584–4592.

https://doi.org/10.1158/1078-0432.CCR-07-5211

21. Duperret EK, Trautz A, Ammons D, *et al*., 2018, Alteration of the tumor stroma using a consensus DNA vaccine targeting fibroblast activation protein (FAP) synergizes with antitumor vaccine therapy in mice. *Clin Cancer Res*, 24: 1190–11201.

https://doi.org/10.1158/1078-0432.CCR-17-2033

22. Gunderson AJ, Yamazaki T, McCarty K, *et al*., 2019, Blockade of fibroblast activation protein in combination with radiation treatment in murine models of pancreatic adenocarcinoma. *PLoS One*, 14: e0211117.

https://doi.org/10.1371/journal.pone.0211117

23. Wang LCS, Lo A, Scholler J, *et al*., 2014, Targeting fibroblast activation protein in tumor stroma with chimeric antigen receptor T cells can inhibit tumor growth and augment host immunity without severe toxicity. *Cancer Immunol Res*, 2: 154–166.

https://doi.org/10.1158/2326-6066.CIR-13-0027

24. Laklai H, Miroshnikova YA, Pickup MW, *et al*., 2016, Genotype tunes pancreatic ductal adenocarcinoma tissue tension to induce matricellular fibrosis and tumor progression. *Nat Med*, 22: 497–505.

https://doi.org/10.1038/nm.4082

25. Valkenburg KC, de Groot AE, Pienta KJ, 2018, Targeting the tumour stroma to improve cancer therapy. *Nat Rev Clin Oncol*, 15: 366–381.

https://doi.org/10.1038/s41571-018-0007-1

26. Kessler L, Ferdinandus J, Hirmas N, *et al*., 2022, Pitfalls and common findings in ^{68}Ga-FAPI PET: A pictorial analysis. *J Nucl Med*, 63: 890–896.

https://doi.org/10.2967/jnumed.121.262808

27. van den Hoven AF, Keijsers RGM, Lam M, *et al*., 2023, Current research topics in FAPI theranostics: A bibliometric analysis. *Eur J Nucl Med Mol Imaging*, 50: 1014–1027.

https://doi.org/10.1007/s00259-022-06052-9

28. Pang Y, Zhao L, Meng T, *et al*., 2023, PET imaging of fibroblast activation protein in various types of cancer using ^{68}Ga-FAP-2286: Comparison with ^{18}F-FDG and ^{68}Ga-FAPI-46 in a single-center, prospective study. *J Nucl Med*, 64: 386–394.

https://doi.org/10.2967/jnumed.122.264544

29. Polson AG, Fuji RN, 2012, The successes and limitations of preclinical studies in predicting the pharmacodynamics and safety of cell-surface-targeted biological agents in patients. *Br J Pharmacol*, 166: 1600–1602.

https://doi.org/10.1111/j.1476-5381.2012.01916.x

30. Watabe T, Liu Y, Kaneda-Nakashima K, *et al*., 2020, Theranostics targeting fibroblast activation protein in the tumor stroma: ^{64}Cu- and ^{225}Ac-labeled FAPI-04 in pancreatic cancer xenograft mouse models. *J Nucl Med*, 61: 563–569.

https://doi.org/10.2967/jnumed.119.233122

31. Loktev A, Lindner T, Burger EM, *et al*., 2019, Development of fibroblast activation protein-targeted radiotracers with improved tumor retention. *J Nucl Med*, 60: 1421–1429.

https://doi.org/10.2967/jnumed.118.224469

32. Rathke H, Fuxius S, Giesel FL, *et al*., 2021, Two tumors, one target: Preliminary experience with 90Y-FAPI therapy in a patient with metastasized breast and colorectal cancer. *Clin Nucl Med*, 46: 842–844.

https://doi.org/10.1097/RLU.0000000000003842.

33. Kratochwil C, Giesel FL, Rathke H, *et al*., 2021, [^{153}Sm] Samarium-labeled FAPI-46 radioligand therapy in a patient with lung metastases of a sarcoma. *Eur J Nucl Med Mol Imaging*, 48: 3011–3013.

https://doi.org/10.1007/s00259-021-05273-8

34. Fu K, Pang Y, Zhao L, *et al*., 2022, FAP-targeted radionuclide therapy with [^{177}Lu]Lu-FAPI-46 in metastatic nasopharyngeal carcinoma. *Eur J Nucl Med Mol Imaging*, 49: 1767–1769.

https://doi.org/10.1007/s00259-021-05634-3

35. Zhao L, Niu B, Fang J, *et al*., 2022, Synthesis, preclinical evaluation, and a pilot clinical PET imaging study of ^{68}Ga-Labeled FAPI dimer. *J Nucl Med*, 63: 862–868.

https://doi.org/10.2967/jnumed.121.263016

36. Pang Y, Zhao L, Fang J, *et al*., 2023, Development of FAPI tetramers to improve tumor uptake and efficacy of FAPI radioligand therapy. *J Nucl Med*, 64: 1449–1455.

https://doi.org/10.2967/jnumed.123.265599

37. Zhao L, Chen J, Pang Y, *et al*., 2022, Development of fibroblast activation protein inhibitor-based dimeric radiotracers with improved tumor retention and antitumor efficacy. *Mol Pharm*, 19: 364036-51.

https://doi.org/10.1021/acs.molpharmaceut.2c00424

38. Moon ES, Ballal S, Yadav MP, *et al*., 2021, Fibroblast activation protein (FAP) targeting homodimeric FAP inhibitor radiotheranostics: A step to improve tumor uptake and retention time. *Am J Nucl Med Mol Imaging*, 11: 476–491.

39. Zboralski D, Hoehne A, Bredenbeck A, *et al*., 2022, Preclinical evaluation of FAP-2286 for fibroblast activation protein targeted radionuclide imaging and therapy. *Eur J Nucl Med Mol Imaging*, 49: 3651–3667.

https://doi.org/10.1007/s00259-022-05842-5

40. Wen X, Xu P, Shi M, *et al*., 2022, Evans blue-modified radiolabeled fibroblast activation protein inhibitor as long-acting cancer therapeutics. *Theranostics*, 12: 422–433.

https://doi.org/10.7150/thno.68182

41. Xu M, Zhang P, Ding J, *et al*., 2022, Albumin binder-conjugated fibroblast activation protein inhibitor radiopharmaceuticals for cancer therapy. *J Nucl Med*, 63: 952–958.

https://doi.org/10.2967/jnumed.121.262533

42. Tranel J, Palm S, Graves SA, *et al*., 2022, Impact of radiopharmaceutical therapy (^{177}Lu, ^{225}Ac) microdistribution in a cancer-associated fibroblasts model. *EJNMMI Phys*, 9: 67.

https://doi.org/10.1186/s40658-022-00497-5

43. Jokar N, Velikyan I, Ahmadzadehfar H, *et al*., 2021, Theranostic approach in breast cancer: A treasured tailor for future oncology. *Clin Nucl Med*, 46: e410–e420.

https://doi.org/10.1097/RLU.0000000000003678

44. Assadi M, Rekabpour SJ, Jafari E, *et al*., 2021, Feasibility and therapeutic potential of ^{177}Lu-fibroblast activation protein inhibitor-46 for patients with relapsed or refractory cancers: A preliminary study. *Clin Nucl Med*, 46: e523–e530.

https://doi.org/10.1097/RLU.0000000000003810

45. Ballal S, Yadav MP, Moon ES, *et al*., 2021, First-in-human results on the biodistribution, pharmacokinetics, and dosimetry of [^{177}Lu]Lu-DOTA.SA.FAPi and [^{177}Lu]Lu-DOTAGA.(SA.FAPi)(2). *Pharmaceuticals* (*Basel*), 14: 1212.

https://doi.org/10.3390/ph14121212

46. Kuyumcu S, Kovan B, Sanli Y, *et al*., 2021, Safety of fibroblast activation protein-targeted radionuclide therapy by a low-dose dosimetric approach using ^{177}Lu-FAPI04. *Clin Nucl Med*, 46: 641–646.

https://doi.org/10.1097/RLU.0000000000003667

47. Baum RP, Schuchardt C, Singh A, *et al*., 2022, Feasibility, biodistribution, and preliminary dosimetry in peptide-targeted radionuclide therapy of diverse adenocarcinomas using ^{177}Lu-FAP-2286: First-in-humans results. *J Nucl Med*, 63: 415–423.

https://doi.org/10.2967/jnumed.120.259192

48. Ferdinandus J, Costa PF, Kessler L, *et al*., 2022, Initial clinical experience with ^{90}Y-FAPI-46 radioligand therapy for advanced-stage solid tumors: A case series of 9 patients. *J Nucl Med*, 63: 727–734.

https://doi.org/10.2967/jnumed.121.262468

49. Fendler WP, Pabst KM, Kessler L, *et al*., 2022, Safety and efficacy of 90Y-FAPI-46 radioligand therapy in patients with advanced sarcoma and other cancer entities. *Clin Cancer Res*, 28: 4346–4353.

https://doi.org/10.1158/1078-0432.CCR-22-1432

50. Kaghazchi F, Aghdam RA, Haghighi S, *et al*., 2022, ^{177}Lu-FAPI therapy in a patient with end-stage metastatic pancreatic adenocarcinoma. *Clin Nucl Med*, 47: e243–e245.

https://doi.org/10.1097/RLU.0000000000004021

51. Ballal S, Yadav MP, Moon ES, *et al*., 2022, Novel fibroblast activation protein inhibitor-based targeted theranostics for radioiodine-refractory differentiated thyroid cancer patients: A pilot study. *Thyroid*, 32: 65–77.

https://doi.org/10.1089/thy.2021.0412

52. Darvin P, Toor SM, Sasidharan Nair V, *et al*., 2018, Immune checkpoint inhibitors: Recent progress and potential biomarkers. *Exp Mol Med*, 50: 1–11.

https://doi.org/10.1038/s12276-018-0191-1

53. Borghaei H, Paz-Ares L, Horn L, *et al*., 2015, Nivolumab versus docetaxel in advanced nonsquamous non-small-cell lung cancer. *N Engl J Med*, 373: 1627–1639.

https://doi.org/10.1056/NEJMoa1507643

54. Schoenfeld AJ, Hellmann MD, 2020, Acquired resistance to immune checkpoint inhibitors. *Cancer Cell*, 37: 443–455.

https://doi.org/10.1016/j.ccell.2020.03.017

55. Joyce JA, Fearon DT, 2015, T cell exclusion, immune privilege, and the tumor microenvironment. *Science*, 348: 74–80.

https://doi.org/10.1126/science.aaa6204

56. Sahai E, Astsaturov I, Cukierman E, *et al*., 2020, A framework for advancing our understanding of cancer-associated fibroblasts. *Nat Rev Cancer*, 20: 174–186.

https://doi.org/10.1038/s41568-019-0238-1

57. Grout JA, Sirven P, Leader AM, *et al*., 2022, Spatial positioning and matrix programs of cancer-associated fibroblasts promote T-cell exclusion in human lung tumors. *Cancer Discov*, 12: 2606–2625.

https://doi.org/10.1158/2159-8290.CD-21-1714

58. Dearnaley DP, Jovic G, Syndikus I, *et al*., 2014, Escalated-dose versus control-dose conformal radiotherapy for prostate cancer: Long-term results from the MRC RT01 randomised controlled trial. *Lancet Oncol*, 15: 464–473.

https://doi.org/10.1016/S1470-2045(14)70040-3

59. Hall S, Rudrawar S, Zunk M, *et al*., 2016, Protection against radiotherapy-induced toxicity. *Antioxidants* (*Basel*), 5: 22.

https://doi.org/10.3390/antiox5030022

60. Jagodinsky JC, Jin WJ, Bates AM, *et al*., 2021, Temporal analysis of Type 1 interferon activation in tumor cells following external beam radiotherapy or targeted radionuclide therapy. *Theranostics*, 11: 6120–6137.

https://doi.org/10.7150/thno.54881

61. Patel RB, Hernandez R, Carlson P, *et al*., 2021, Low-dose targeted radionuclide therapy renders immunologically cold tumors responsive to immune checkpoint blockade. *Sci Transl Med*, 13: eabb3631.

https://doi.org/10.1126/scitranslmed.abb3631

62. Hernandez R, Walker KL, Grudzinski JJ, *et al*., 2019, ^{90}Y-NM600 targeted radionuclide therapy induces immunologic memory in syngeneic models of T-cell non-Hodgkin's lymphoma. *Commun Biol*, 2: 79.

https://doi.org/10.1038/s42003-019-0327-4

63. Twyman-Saint Victor C, Rech AJ, Maity A, *et al*., 2015, Radiation and dual checkpoint blockade activate non-redundant immune mechanisms in cancer. *Nature*, 520: 373–377.

https://doi.org/10.1038/nature14292

64. Thierens HM, Monsieurs MA, Brans B, *et al*., 2001, Dosimetry from organ to cellular dimensions. *Comput Med Imaging Graph*, 25: 187–193.

https://doi.org/10.1016/s0895-6111(00)00047-1

65. Gill MR, Falzone N, Du Y, *et al*., 2017, Targeted radionuclide therapy in combined-modality regimens. *Lancet Oncol*, 18: e414–e423.

https://doi.org/10.1016/S1470-2045(17)30379-0

66. Chen H, Zhao L, Fu K, *et al*., 2019, Integrin alpha(v)beta(3)-targeted radionuclide therapy combined with immune checkpoint blockade immunotherapy synergistically enhances anti-tumor efficacy. *Theranostics*, 9: 7948–7960.

https://doi.org/10.7150/thno.39203

67. Choi J, Beaino W, Fecek RJ, *et al*., 2018, Combined VLA-4-targeted radionuclide therapy and immunotherapy in a mouse model of melanoma. *J Nucl Med*, 59: 1843–1849.

https://doi.org/10.2967/jnumed.118.209510

68. Czernin J, Current K, Mona CE, *et al*., 2021, Immune-checkpoint blockade enhances ^{225}Ac-PSMA617 efficacy in a mouse model of prostate cancer. *J Nucl Med*, 62: 228–231.

https://doi.org/10.2967/jnumed.120.246041

69. Esfahani SA, De Aguiar Ferreira C, Summer P, *et al*., 2023, Addition of peptide receptor radiotherapy to immune checkpoint inhibition therapy improves outcomes in neuroendocrine tumors. *J Nucl Med*, 64: 1056–1061.

https://doi.org/10.2967/jnumed.123.265391

70. Feig C, Jones JO, Kraman M, *et al*., 2013, Targeting CXCL12 from FAP-expressing carcinoma-associated fibroblasts synergizes with anti-PD-L1 immunotherapy in pancreatic cancer. *Proc Natl Acad Sci U S A*, 110: 20212–20217.

https://doi.org/10.1073/pnas.1320318110

71. Zboralski D, Osterkamp F, Christensen E, *et al*., 2023, Fibroblast activation protein targeted radiotherapy induces an immunogenic tumor microenvironment and enhances the efficacy of PD-1 immune checkpoint inhibition. *Eur J Nucl Med Mol Imaging*, 50: 2621–2635.

https://doi.org/10.1007/s00259-023-06211-6

72. Fu H, Huang J, Sun L, *et al*., 2022, FAP-targeted radionuclide therapy of advanced radioiodine-refractory differentiated thyroid cancer with multiple cycles of 177 Lu-FAPI-46. *Clin Nucl Med*, 47: 906–907.

https://doi.org/10.1097/RLU.0000000000004260

73. Rao Z, Zhang Y, Liu L, *et al*., 2023, ^{177}LuLu-FAP-2286 therapy in a case of right lung squamous cell carcinoma with systemic metastases. *Eur J Nucl Med Mol Imaging*, 50: 1266–1267.

https://doi.org/10.1007/s00259-022-06048-5

ACCSCIENCE PUBLISHING

Advances in Radiotherapy & Nuclear Medicine

ORIGINAL RESEARCH ARTICLE

Dosimetry and safety of single-channel applicators for intracavitary brachytherapy in cervical cancer

Ren-Jin Chen, Hao-Wen Pang, Xiang-Xiang Shi, Lei Yang, Sheng Lin*, and Jing-Bo Wu*

Department of Oncology, The Affiliated Hospital of Southwest Medical University, Sichuan 646000, China

Abstract

High-dose-rate intracavitary brachytherapy plays a crucial role in achieving local control in the treatment of unresectable uterine cervical cancer. In this treatment approach, the single-channel applicator (SCA) offers a simpler structure for implantation compared to the fletcher applicator set (FAS), easing the treatment planning. To evaluate the dosimetry and safety of the SCA for intracavitary brachytherapy in cervical cancer, the present study aims to assess its dose distribution in relation to the FAS. In this study, we compared the physical and dosimetric characteristics of the inferential reference points (A, cervix; B, bladder; and R, rectum) of the SCA to those obtained with tandem and FAS dosing. Dosimetric characteristics and dose distributions in a Chinese female anthropomorphic phantom were evaluated using RGD-3B thermoluminescent dosimetry. The SCA generated an oblate, pear-shaped dose distribution curve, resulting in a reduced high-dose area along the bladder-rectum axis. Compared to the tandem, the SCA resulted in dose reductions of 21% and 17% at the bladder and rectum, respectively. When compared to the FAS, the dosing with the SCA at the bladder and rectum did not show significant differences concerning the occurrence of severe toxic effects. The SCA demonstrated a dose distribution curve similar to the standard FAS but not the tandem. The results of the present study indicate that both SCA and FAS showed equally acute toxicity and resulted in late injuries to the rectum and bladder. Nevertheless, the SCA's simpler structure, which allows for more convenient placement and planning, warrants further clinical investigations to assess its efficacy and practical application.

Keywords: Single-channel applicator; Cervical cancer; Intracavitary brachytherapy; Dosimetry

***Corresponding authors:**
Sheng Lin
(lslinsheng@163.com)
Jing-Bo Wu
(wjb6147@163.com)

Citation: Chen R, Pang H, Shi X, *et al*., 2023, Dosimetry and safety of single-channel applicators for intracavitary brachytherapy in cervical cancer. *Adv Radiother Nucl Med,* 1(2): 0322
https://doi.org/10.36922/arnm.0322

Received: March 10, 2023

Accepted: July 13, 2023

Published Online: August 17, 2023

1. Introduction

Cervical cancer is the second most common gynecological malignancy worldwide, particularly prevalent in developing countries, and is also the leading cause of tumor-related mortality[1]. In China alone, cervical cancer accounts for 15,000 new cases and 30,000 deaths annually[2]. While the formulation of appropriate cancer control policies and the improvement in healthcare infrastructure may contribute to a reduction in incidence, it is essential for doctors to focus on improving current therapeutic approaches and patient outcomes[3-5].

Radiotherapy, which involves the optimal integration of brachytherapy and external-beam radiotherapy, represents a critical treatment option for cervical cancer at any stage. Brachytherapy plays an important role in treating all-invasive cervical cancer, mainly using afterloading devices for intracavitary treatment. The majority of currently available applicators have been prepared following the Manchester method[6-8], characterized by the use of intrauterine sources along with vaginal sources (one tandem plus two ovoids). However, each brachytherapy fraction shows significant variation due to the geometric displacement of the left ovoid, right ovoid, and tandem. Furthermore, we often encounter patients with narrow vaginas or sensitivity to surgical stress, making applicator placement difficult for them. As a result, these patients often need to undergo applicator placement under spinal or general anesthesia.

Accordingly, we aimed to challenge the existing method used for source placement by hypothesizing that a single tube (single-channel applicator [SCA]) could proximately represent a fletcher applicator set (FAS). In the present study, we modified the tandem with asymmetrical shielding on the channel and verified that this SCA could generate flat, pear-shaped, and isodose curves similar to those obtained using the FAS. This modification effectively reduced the irradiation along the bladder-rectum axis, as measured considering the physical and dosimetric characteristics. The SCA is a simple, and easy-to-use structure used for implant surgery; it causes limited autologous geometric displacement. Despite having a single-tube structure, it functions similarly to nearly three tubes. Accordingly, we believe that the SCA warrants further clinical investigation.

2. Materials and methods

2.1. Key instruments and materials

We used the SCA (Chinese patent no., 200710050108.1, State Intellectual Property Office of the PRC; the concise depiction of the structure is shown in Figure 1). We also used the FAS and a micro-electron ^{192}Ir afterloading system (Nucletron, the Netherlands), Oncentra 4.3 treatment planning software (Elekta Brachytherapy, Veenendaal, the Netherlands), GafChromic EBT2 films (ISP, Wayne, NJ, U.S.A.), RIT113 film dosimeter software, version 4.2 (Radiological Imaging Technology, Inc., U.S.A), an RGD-3B thermoluminescent dosimeter (TLD), and related-element LiF: Mg, Cu **and** P (GR-200A, standard treatment indicated by the National Institute of Metrology, Luzhou, China).

2.2. Patients and ethical considerations

A total of 48 patients with stage IIB to IIIB cervical cancer were selected for this trial from our department until 2008.

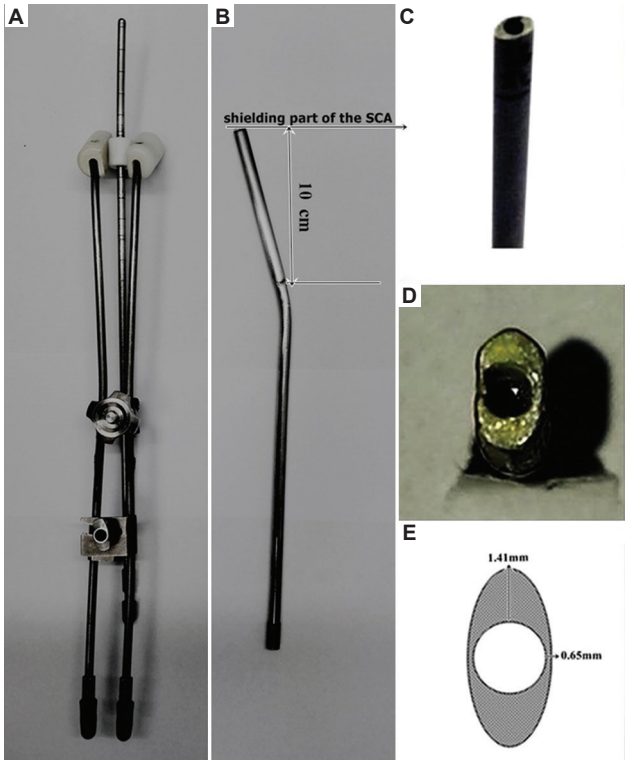

Figure 1. The structure of our single-patient applicator. (A) FAS; (B) SCA; (C) and (D) SCA appearance; and (E) SCA cross-sectional view. Schematic diagram shows different thicknesses of 1.41 mm and 0.65 mm at the sagittal and coronal axes, respectively. Finished SCA with an added trocar sheath for surgery, with a maximum diameter of 0.68 cm.
Abbreviations: FAS: Fletcher applicator set; SCA: Single-channel applicator.

The Hospital Ethics Committee conducted a thorough inspection and assessment to ensure the least possible harm and maximum benefit for the patients (approval no. K22012004). All patients provided informed consent by signing consent forms for participation.

2.3. Planar physical dosimetry

Films were irradiated with 2 Gy using the SCA and tandem in the coronal, sagittal, and sectional planes. To compare the differences between the SCA and tandem, the irradiated films were then analyzed with a RIT113 film dosimeter using version 4.2 software (RIT, Chicago, USA).

2.4. Dosimetry of the SCA on the Chinese female anthropomorphic phantom (CFAP)

The applicators were inserted to a depth of 5 cm into the phantom, and the inferential reference points (A, cervix; B, bladder; and R, rectum) were determined according to the ICRU 38 definitions. Point A was defined as a point located 2 cm superior to the lateral vaginal fornix and 2 cm lateral to the cervical canal. The posterior vaginal wall was visualized on computed tomography images with the

help of an intravaginal obturator and posterior catheters. The bladder reference point (B) was identified as the most posterior point of the Foley balloon. The rectal reference point (R) was located on the appropriate axial slice on an anteroposterior line drawn through the lowest intrauterine source dwell position, 5 mm behind the posterior vaginal wall. Matched, sheeted LiF was fixed at the homologous sites mentioned above for dose calculation using a TLD (the dose to point A was 2 Gy). CFAP and related devices are shown in Figure 2.

2.5. Three-dimensional dosimetry of the SCA and FAS

The three-dimensional dose of the FAS (Elekta, Veenendaal, the Netherlands) was generated using the Oncentra 4.3 TPS (Elekta, Veenendaal, the Netherlands), and the three-dimensional dose of the SCA was generated using the TPS prepared by our team.

2.6. Dosimetric points

Before applicator placement, laxatives were administered to facilitate the elimination of rectal content. A Foley catheter was inserted to keep the bladder empty, and the catheter's balloon was routinely filled with radiopaque solution (7 cm^3). A clubbed LiF dosimeter was fixed at the forepart of the urinary Foley catheter's balloon, which was placed at the point B and point R sites, according to the ICRU 38 definitions. Dosimetry measurements between the SCA and tandem were undertaken in six patients between 2009 and 2010. At the time of administering the last fraction of intracavitary brachytherapy, an extra dose of 20 cGy was administered to compare the dose contribution to the B and R points. For a randomized dosimetry comparison between the SCA and FAS, 41 patients were selected beginning in 2012 based on the findings of our clinical trial of the SCA (ChiCTR-TRC-12002321, Chinese Clinical Trail Registry). The total sample size of our randomized and controlled trial was n = 300 and patients were randomly assigned to either the SCA or FAS group using a computerized randomization procedure. Patients ready for treatment were randomized after routine external-beam radiotherapy using the above-mentioned dosimetric procedure, except for the testing dose, which was 7 Gy.

2.7. Statistical methods

Data on physical dosimetry are presented only as raw data, and we used one-way ANOVA for direct assessment. Dosimetric measurements were analyzed using the t-test, while disease characteristics were assessed using the F-test method. We used SPSS 19.0 software (IBM, Chicago, USA) to analyze the different groups. $P < 0.05$ was considered statistically significant.

3. Results

3.1. Isodose distribution between the SCA and tandem on film dosimetry

With a testing dose of 2 Gy, the isodose curves of the SCA presented a flat buninoid dose distribution, while the tandem presented a buninoid dose distribution, especially in cross-section images (Figure 3). Compared to the tandem, the SCA demonstrated an asymmetrical dose distribution due to the asymmetrical shielding of the SCA channel. This asymmetry resulted in a reduction in the high-dose area on distinct axes, making SCA suitable for protecting adjacent organs, such as the rectum and bladder. The reduction ratios of the SCA were 1.86%, 10.32%, and 19.59% on the coronal, sagittal, and cross-sectional axes, respectively (Table 1).

3.2. Isodose distribution between the SCA and tandem on the CFAP using a TLD

With a testing dose of 2 Gy, the absorbed irradiation doses at points A, B, and R with the SCA were 2.18 Gy, 1.47 Gy, and 1.91 Gy, respectively, while those with the tandem were 2.26 Gy, 1.95 Gy, and 2.59 Gy, respectively. Compared to the tandem, the reduction ratios of the SCA

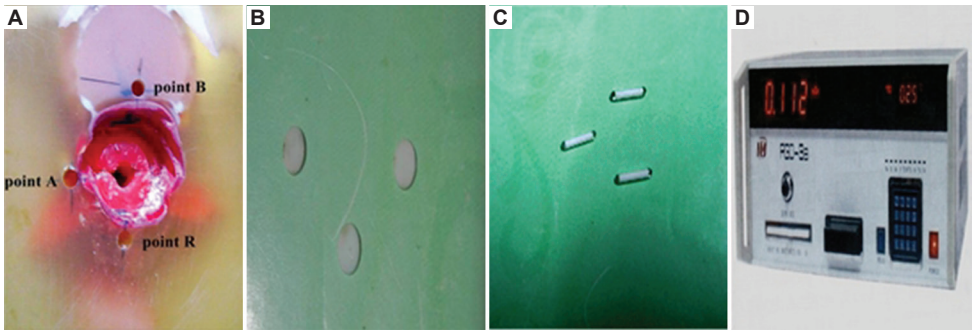

Figure 2. CFAP applied for dosimetric detection of TLD relative elements, sheeted LiF applied for CFAH TLD detection and clubbed LiF applied for patient detection. (A) CFAP; (B) sheeted LiF; (C) clubbed LiF; and (D) measuring instrument for TLD.
Abbreviations: TLD: Thermoluminescent dosimeter; CFAD: Chinese female anthropomorphic phantom.

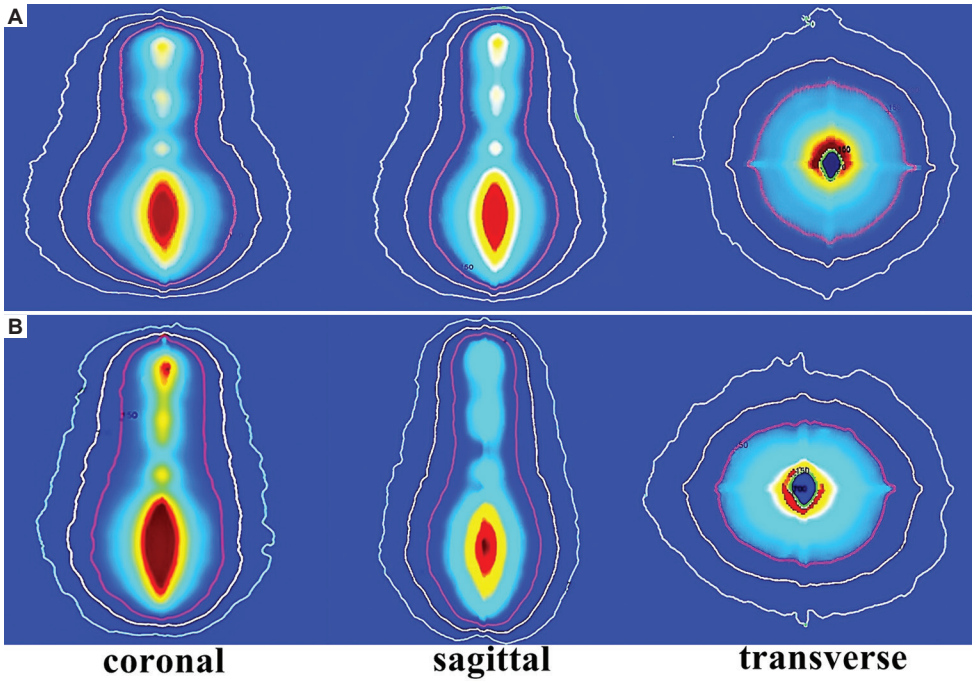

Figure 3. Sectional and three-dimensional dose distributions between SCA and tandem. Isodose curve of SCA and tandem on coronal, sagittal, and cross-sectional views (from inner to outer representing isodose curves of 150%, 100% and 70%, respectively (shown in Table 1).
Abbreviations: SCA: Single-channel applicator.

Table 1. Different areas of 100% dose curves between SCA and tandem

	Tandem (cm^2)	SCA (cm^2)	Difference (%)
Coronal plane	40.87±1.01	40.11±1.01	1.86±0.14
Sagittal plane	40.02±0.47	35.89±0.68	10.32±0.92
Cross-sectional plane	32.35±0.62	26.01±0.20	19.59±0.95

Notes: SCA was almost the same as tandem on the coronal axis; SCA was smaller than tandem on the sagittal and cross-sectional axes.
Abbreviations: TLD: Thermoluminescent dosimeter;
SCA: Single-channel applicator.

at points A, B, and R were 3.18%, 24.88%, and 26.58%, respectively (Table 2). Dosimetry findings with a TLD on the CFAP revealed that the SCA could effectively reduce the irradiation to points B and R.

3.3. Preliminary dosimetry comparison between the SCA and tandem in 6 patients treated with a low dose of 20 cGy

A total of six patients, aged 28 – 56 years, were enrolled in a clinical trial between 2009 and 2010 after providing informed consent to participate. They agreed to receive an additional 20 cGy as part of the last fraction of brachytherapy. When 20 cGy was administered using each applicator, the absorbed irradiation doses of the SCA at points B and R were approximately 5.06 cGy and 6.79 cGy, respectively, while those of the tandem were 6.43 cGy and 8.23 cGy, respectively. The reduction ratios of the SCA at points B and R were 21.5% and 17.6%, respectively (Table 3), thus completing the preliminary identification.

3.4. Dosimetry between the SCA and FAS in 41 patients with cervical cancer

The dosimetric results on a TLD at point B showed a mean dose of 232.83 ± 23.33 cGy for the SCA in 19 patients, compared with a mean dose of 236.0 ± 17.49 cGy for the FAS in 22 patients. The results indicate no significant difference (P = 0.903). At point R, the mean dose for the SCA was 510.2 ± 27.20 cGy, while the mean dose for the FAS was 538.6±18.35 cGy, also showing no significant difference (P = 0.381; Figure 4). The patient and disease characteristics at baseline, treated with the SCA and FAS, are shown in Table 4. There was no significant difference in baseline data between the two groups. The SCA was found to be as safe as FAS when used as an applicator of intracavitary brachytherapy in cervical cancer.

4. Discussion

Recommendations for the treatment of cervical cancer are based on the clinical stage. At present, patients with stage IA1 cervical cancer usually undergo a hysterectomy due to the low incidence of lymph node metastasis, while patients with IA2 to IIA disease have the option of surgery or radiotherapy, both of which are equally effective. Lymph

Table 2. Chinese female anthropomorphic phantom's TLD dosimetry between SCA and tandem

	Point A (cGy)	Point B (cGy)	Point R (cGy)	B/A	R/A
Tandem	226.01±25.71	195.62±13.14	259.88±19.9	6.91±5.24	116.65±21.97
SCA	218.64±22.54	147.10±13.09	191.04±20.04	7.38±2.72	88.67±18.78
Difference	7.37±3.33	48.53±0.36	68.84±5.93	7.55±3.32	10.65±4.35
Difference %	3.18±1.11	24.88±1.62	26.58±2.76	8.57±3.30	8.87±2.24

Notes: SCA was almost the same as tandem at point A; SCA was smaller than tandem at points B and R; B/A: Dose at point B divided by dose at point A; R/A: Dose at point R divided by dose at point A.
Abbreviations: TLD: Thermoluminescent dosimeter; SCA: Single-channel applicator.

Table 3. Dosimetric TLD dosimetry between SCA and tandem

	Tandem (cGy)	SCA (cGy)	Difference (cGy)	Difference (%)
Point B	6.43±0.79	5.06±0.84	1.37±0.06	21.54±3.35
Point R	8.23±0.35	6.79±0.46	1.45±0.18	17.62±2.61

Abbreviations: TLD: Thermoluminescent dosimeter; SCA: Single-channel applicator.

node involvement is observed in 60% of patients with stage IB2 cervical cancer, and patients with IIB or worse disease should be treated with concomitant chemoradiotherapy[9-11]. In fact, radiotherapy plays an important role in the treatment of each stage of cervical cancer, even early-stage cancer, as it is as effective as surgery.

Brachytherapy is a vital element of radiotherapy, and the American Brachytherapy Society has affirmed its essential curative role in the management of locally advanced cervical cancer through tandem-based treatment[7,12]. Bladder and rectal toxicities associated with cervical cancer are due to the effects of brachytherapy[13]. The importance of the applicator in brachytherapy cannot be overstated, as it is necessary for delivering the radioactive source. Current applicator sets typically consist of one intrauterine applicator combined with vaginal applicators, generating an oblate, and pear-shaped dose curve, which not only covers the tumor mass but also reduces irradiation to the bladder and rectum[14,15]. However, during low-dose-rate or high-dose-rate brachytherapy, the position differences have been observed to be more than 1 cm in 60% of applications, partly due to insufficient fixation of the applicators both to each other and to the table, changes in the two ovoids, or ovoids being higher than the tandem in non-fixed applications[16-19]. Another issue is the compliance of patients during applicator placement without using analgesia[20-23].

Accordingly, in the present study, we focused on altering the placement pattern of currently used applicators to simplify the procedure of brachytherapy. We modified the channel of the tandem with an overlay of lead shielding that was 1.41 mm thick in the sagittal axis and 0.65 mm

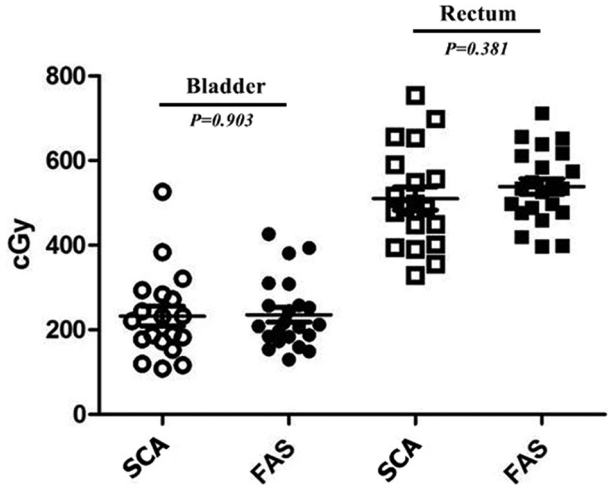

Figure 4. Statistical comparison of dosimetric at points B and R between SCA and FAS. Detection between SCA and FAS of absorbed irradiation r showed no significant difference with *P* values of 0.381 of at point R and 0.903 at point B.
Abbreviations: SCA: Single-channel applicator; FAS: Fletcher applicator set.

thick in the coronal axis (the structure of the SCA is shown in Figure 1). First, we observed whether this modified tube could achieve deformation of the dose distribution curve in certain axes. As expected, after the shielding modification, the isodose curve of the SCA definitively formed a flat, pear-shaped isodose curve. The reduction ratios of the SCA in the sagittal and cross-sectional planes were 10.32% and 19.59%, respectively, compared to those observed for the tandem (Figure 3 and Table 1). Thus, the SCA, as a novel applicator for cervical cancer, possessed the most important features to effectively reduce the high-dose area along the bladder-rectum axis.

Next, we compared the results of six patients treated with an additional small dose of 20 cGy, and the findings were consistent with those obtained with physical dosimetry. The reduction ratios at points B and R with the SCA were 21% and 17%, respectively, compared to those obtained with the tandem (Table 2). These dosimetric data encouraged us to proceed with the subsequent comparison with the FAS and lay the foundations for future clinical

Table 4. Patients and disease characteristics at baseline ready for treatment and comparison of toxicity between SCA and FAS

Characteristic	SCA (n=19)		FAS (n=22)		*P*-value	
Age (years)					0.863	
Range	41–65		36–69			
Median	51		53			
Pathology (n [%])					0.861	
Squamous cell carcinoma	16 (84.21)		20 (90.91)			
Adenocarcinoma	3 (15.79)		2 (9.09)			
Staging (n [%])					0.426	
IIA	5 (26.32)		2 (9.09)			
IIB	10 (52.63)		16 (72.73)			
IIIA	3 (15.79)		2 (9.09)			
IIIB	1 (5.26)		2 (9.09)			
ECOG score (n [%])					0.563	
0	8 (42.11)		12 (54.55)			
1	10 (52.63)		8 (36.36)			
2	1 (5.26)		2 (9.09)			
Acute toxicity[a] (n [%])	B	R	B	R	B 0.689	R 0.344
0	11 (57.89)	8 (42.11)	14 (63.64)	14 (63.64)		
1	7 (36.84)	9 (47.37)	5 (22.73)	6 (27.27)		
2	1 (5.26)	2 (10.53)	2 (9.09)	2 (9.09)		
3			1 (4.55)			
Late injury[b] (n [%])	B	R	B	R	B 0.860	R 0.850
0	14 (73.68)	15 (78.95)	15 (68.18)	14 (63.64)		
1	4 (21.05)	3 (15.79)	6 (27.27)	5 (22.73)		
2	1 (5.26)	1 (5.26)	1 (4.55)	2 (9.09)		
3				1 (4.55)		

Notes: B represents bladder, and R represents rectum. [a]Acute toxicity means toxicity to the bladder and rectum over the course of treatment or within 3 months post-treatment (*F*-test-based method). [b]Late injury means injury to the bladder and rectum after 3 months post-treatment (*F*-test-based method).
Abbreviations: FAS: Fletcher applicator set; SCA: Single-channel applicator.

applications. Based on our study, irradiation to point A, point B, and point R, was equal between the SCA and FAS, showing no significant differences ($P > 0.05$) in both acute and late toxic effects during follow-up.

5. Conclusions

We found that the SCA was superior to the FAS on the grounds of its more simplified procedure of brachytherapy. Nevertheless, despite the promising potential of the SCA, further prospective validation studies are needed before considering it as a possible alternative for those unwilling to undergo brachytherapy using the FAS.

Acknowledgments

None.

Funding

This work was supported by grants from the Supported Project of Science and Technology Department of Sichuan Province (Z1443) and the Affiliated Hospital of Southwest Medical University (14004).

Conflict of interest

The authors declare no conflicts of interest.

Author contributions

Conceptualization: Jing-Bo Wu
Investigation: Hao-Wen Pang, Xiang-Xiang Shi
Writing – original draft: Ren-Jin Chen, Lei Yang
Writing – review & drafting: Sheng Lin

Ethics approval and consent to participate

The Hospital Ethics Committee conducted a thorough inspection and assessment to ensure minimal harm and maximum benefit to the patients (approval no. K22012004). All patients provided informed consent for participation.

Consent for publication

Not applicable.

Availability of data

All the data are included in the article, and further, inquiries can be directed to the corresponding authors following formal request.

References

1. Sankaranarayanan R, Ferlay J, 2013, Burden of breast and gynecological cancers in low-resource countries. In: Breast and Gynecological Cancers. New York: Springer, p1–17.

2. Jemal A, Bray F, Center MM, *et al*., 2011, Global cancer statistics. *CA Cancer J Clin*, 61: 69–90.

   https://doi.org/10.3322/caac.20107

3. Jemal A, Center MM, DeSantis C, *et al*., 2010, Global patterns of cancer incidence and mortality rates and trends. *Cancer Epidemiol Biomarkers Prev*, 19: 1893–1907.

   https://doi.org/10.1158/1055-9965.EPI-10-0437

4. Arbyn M, Castellsague X, de Sanjose S, *et al*., 2011, Worldwide burden of cervical cancer in 2008. *Ann Oncol*, 22: 2675–2686.

   https://doi.org/10.1093/annonc/mdr015

5. Forouzanfar MH, Foreman KJ, Delossantos AM, *et al*., 2011, Breast and cervical cancer in 187 countries between 1980 and 2010: A systematic analysis. *Lancet*, 378: 1461–1484.

   https://doi.org/10.1016/S0140-6736(11)61351-2

6. Basu B, Basu S, Chakraborti B, *et al*., 2012, A comparison of dose distribution from Manchester-style and Fletcher-style intracavitary brachytherapy applicator systems in cervical cancer. *J Contemp Brachytherapy*, 4: 213–218.

   https://doi.org/10.5114/jcb.2012.32555

7. Narayan K, Barkati M, van Dyk S, *et al*., 2010, Image-guided brachytherapy for cervix cancer: From Manchester to Melbourne. *Expert Rev Anticancer Ther*, 10: 41–46.

   https://doi.org/10.1586/era.09.166

8. Wakatsuki M, Ohno T, Yoshida D, *et al*., 2011, Intracavitary combined with CT-guided interstitial brachytherapy for locally advanced uterine cervical cancer: Introduction of the technique and a case presentation. *J Radiat Res*, 52: 54–58.

   https://doi.org/10.1269/jrr.10091

9. Giorda G, Boz G, Gadducci A, *et al*., 2011, Multimodality approach in extra cervical locally advanced cervical cancer: Chemoradiation, surgery and intra-operative radiation therapy: A phase II trial. *Eur J Surg Oncol*, 37: 442–447.

   https://doi.org/10.1016/j.ejso.2011.02.011

10. Rob L, Skapa P, Robova H, 2011, Fertility-sparing surgery in patients with cervical cancer. *Lancet Oncol*, 12: 192–200.

    https://doi.org/10.1016/S1470-2045(10)70084-X

11. James ND, Hussain SA, Hall E, *et al*., 2012, Radiotherapy with or without chemotherapy in muscle-invasive bladder cancer. *N Engl J Med*, 366: 1477–1488.

    https://doi.org/10.1056/nejmoa1106106

12. Mourya A, Aggarwal LM, Choudhary S, 2021, Evolution of brachytherapy applicators for the treatment of cervical cancer. *J Med Phys*, 46: 231–243.

    https://doi.org/10.4103/jmp.jmp_62_21

13. Mahantshetty U, Tiwana MS, Jamema S, *et al*., 2011, Additional rectal and sigmoid mucosal points and doses in high dose rate intracavitary brachytherapy for carcinoma cervix: A dosimetric study. *J Cancer Res Ther*, 7: 298–303.

    https://doi.org/10.4103/0973-1482.87027

14. Goyal MK, Kehwar TS, Manjhi J, *et al*., 2016, Dosimetric evaluation of tandem-based cervical high-dose-rate brachytherapy treatment planning using American Brachytherapy Society 2011 recommendations. *J Radiother Pract*, 15: 283–289.

    https://doi.org/10.1017/S1460396916000133

15. Jahan D, Ahmad S, Thompson S, *et al*., 2023, Dosimetric evaluation of the feasibility of utilizing a reduced number of interstitial needles in combined intracavitary and interstitial brachytherapy for cervical cancer. *J Appl Clin Med Phys*, 24: e13833.

    https://doi.org/10.1002/acm2.13833

16. Hoskin PJ, Cook M, Bouscale D, *et al*., 1996, Changes in applicator position with fractionated high dose rate gynaecological brachytherapy. *Radiother Oncol*, 40: 59–62.

    https://doi.org/10.1016/0167-8140(96)01746-x

17. Datta NR, Kumar S, Das KJ, *et al*., 2001, Variations of intracavitary applicator geometry during multiple HDR brachytherapy insertions in carcinoma cervix and its influence on reporting as per ICRU report 38. *Radiother Oncol*, 60: 15–24.

    https://doi.org/10.1016/s0167-8140(01)00352-8

18. Garipağaoğlu M, Tuncçl N, Köseoğlu FG, *et al*., 2004, Geometric and dosimetric variations of ICRU bladder and rectum reference points in vaginal cuff brachytherapy using ovoids. *Int J Radiat Oncol Biol Phys*, 58: 1607–1615.

    https://doi.org/10.1016/j.ijrobp.2003.11.039

19. Garipağaoğlu M, Tunçel N, Dalmaz MG, *et al*., 2006,

Changes in applicator positions and dose distribution between high dose rate brachytherapy fractions in cervix carcinoma patients receiving definitive radiotherapy. *Br J Radiol*, 79: 504–509.

https://doi.org/10.1259/bjr/33762931

20. Wiebe E, Surry K, Derrah L, *et al.*, 2011, Pain and symptom assessment during multiple fractions of gynecologic high-dose-rate brachytherapy. *Brachytherapy*, 10: 352–356.

https://doi.org/10.1016/j.brachy.2011.04.001

21. Waldenström AC, Olsson C, Wilderäng U, *et al.*, 2011, Pain and mean absorbed dose to the pubic bone after radiotherapy among gynecological cancer survivors. *Int J Radiat Oncol Biol Phys*, 80: 1171–1180.

https://doi.org/10.1016/j.ijrobp.2010.04.007

22. Bhanabhai H, Samant R, Grenier L, *et al.*, 2013, Pain assessment during conscious sedation for cervical cancer high-dose-rate brachytherapy. *Curr Oncol*, 20: e307–e310.

https://doi.org/10.3747/co.20.1404

23. Cepni K, Gul S, Cepni I, *et al.*, 2011, Randomized trial of oral misoprostol treatment for cervical ripening before tandem application in cervix cancer. *Int J Radiat Oncol Biol Phys*, 81: 778–781.

https://doi.org/10.1016/j.ijrobp.2010.06.051

ACCSCIENCE PUBLISHING

Advances in Radiotherapy & Nuclear Medicine

ORIGINAL RESEARCH ARTICLE

Unveiling the relationship between the SUVmax of ^{18}F-FDG PET/CT and patient and tumor characteristics

Nishant Lohia[1], Sirshendu Ghosh[2], Sankalp Singh[1]*, Indranil Sinha[3], Abhishek Mahato[3], Dharmesh Paliwal[3], and Gaurav Trivedi[1]

[1]Department of Radiation Oncology, Malignant Disease Treatment Centre, Command Hospital (Central Command), Lucknow, Uttar Pradesh, India

[2]Command Dental Centre, Lucknow, Uttar Pradesh, India

[3]Department of Nuclear Medicine, Command Hospital (Central Command), Lucknow, Uttar Pradesh, India

Abstract

^{18}F-fluoro-2-deoxyglucose (FDG)-based positron emission tomography (PET)/computed tomography (CT) is an indispensable tool in modern oncology, extensively used for diagnosing and staging various cancers. The maximum standardized uptake value (SUV_{max}) of FDG helps identify the most metabolically active areas of disease. In this analytical cross-sectional study performed between January and December 2019, we compared SUV_{max} for different cancer types and determined the effect of demographic, pathological, and clinical variables on SUV_{max}. The study included 117 newly diagnosed cancer patients who underwent FDG PET/CT before treatment. Data on descriptive variables, including age, gender, stage, histopathological diagnosis, and tumor differentiation grade, were collected for each patient. Correlation analysis of these variables with SUV_{max} in FDG PET/CT was performed using Spearmen's test and a forward stepwise regression model. A total of 117 patients (63 males and 54 females) with a median age of 61 years (range: 21 – 90) were included in this study. Histopathological diagnoses revealed squamous cell carcinoma (n = 71%), adenocarcinoma (n = 24%), and small cell cancer (n = 5%). The SUV_{max} of the primary tumor was positively correlated with histology ($P < 0.05$), with the highest SUV_{max} observed in squamous cell carcinomas. In conclusion, SUV_{max} was positively correlated with histology, while no association was detected with the patient's age and gender, as well as the stage, organ, site, or grade of the tumors. However, we recommend a larger and more homogenous study sample to further investigate any clinically relevant relationship between the SUV_{max} and various disease factors in diverse patient populations.

Keywords: ^{18}F-fluoro-2-deoxyglucose; Maximum standardized uptake value; Positron emission tomography/computed tomography; Cancer; Histopathology; Squamous cell carcinoma

***Corresponding author:**
Sankalp Singh
(oncodoctor81@gmail.com)

Citation: Lohia N, Ghosh S, Singh S, *et al.*, 2024, Unveiling the relationship between the SUVmax of ^{18}F-FDG PET/CT and patient and tumor characteristics. *Adv Radiother Nucl Med*, 1(2): 2032. https://doi.org/10.36922/arnm.2032

Received: October 13, 2023

Accepted: January 5, 2024

Published Online: January 10, 2024

1. Introduction

Cancer is one of the leading causes of death worldwide. Its treatment requires multimodality care, commencing with early diagnosis, accurate staging, and a

comprehensive metastatic workup. ^{18}F-fluoro-2-deoxyglucose-positron emission tomography (FDG-PET), used in conjunction with computerized tomography (CT), offers precise anatomical localization and functional information about metabolic activity. As a result, it becomes a useful imaging tool in both the diagnosis and staging of malignant tumors[1-3].

FDG-PET/CT is widely used in evaluating malignant tumors[4]. The increased uptake of ^{18}F-fluoro-2-deoxyglucose (^{18}F-FDG), an analog of glucose, serves as a marker of increased glycolytic activity within tumor tissues due to their heightened metabolism compared to surrounding normal tissues. The advent of PET-CT has significantly changed cancer staging, resulting in many cases being upstaged or downstaged compared to conventional anatomical imaging. Consequently, this change has a substantial impact on the management of individual patients. Integrated PET/CT has rapidly and widely gained clinical acceptance since its acceptance, becoming an indispensable imaging tool in the management of most solid tumors over the past decade.

PET/CT not only visualizes but also quantifies FDG uptake to differentiate metabolically highly active tissues from less active tumor tissues. Thus, the level of cell proliferation activity in different tissues can be inferred. The maximum standardized uptake value (SUV_{max}) is a semi-quantitative parameter commonly used in reporting different levels of metabolic activity in PET/CT scans[5-7].

To the best of our knowledge and based on an extensive online literature search, demographic and clinicopathological factors influencing the change of SUV_{max} in PET have not yet been comprehensively researched or documented. However, a study on squamous cell carcinomas of the tongue (TSCC) established some relationship between SUV_{max} and clinicopathological characteristics[8]. In addition, there are systematic reports on the relationship between SUV_{max} and clinicopathological characteristics in lung, esophageal, ovarian, and endometrial cancers[9-12]. The present study aimed to investigate the correlation of clinicopathological parameters with SUV_{max} in FDG PET/CT of patients of various cancer sites. The established relationship could yield additional information, such as the inherent aggressiveness and natural course of various tumors based on their SUV_{max}, as well as prognostic information, including the survival outcomes of the patients.

2. Methods

Our study was approved by the Institutional Review Board of Command Hospital (CC), Lucknow, and written informed consent was obtained from every patient. This cross-sectional study was carried out in the nuclear medicine and oncology departments of a tertiary cancer care center in Northern India. It included all newly diagnosed, treatment-naïve cancer patients who underwent PET/CT at the mentioned departments from January 2019 to December 2019, encompassing patients with various cancer sites.

2.1. Study population

The study population consisted of patients diagnosed with cancers in four broad organ systems, namely, head and neck, gastrointestinal (GI), thoracic, and gynecological cancers. Within these systems, various sub-sites were explored: (i) head–and-neck system, encompassing nasopharynx, oropharynx, hypopharynx, larynx, oral cavity, and CUPS neck (carcinoma of unknown primary with secondaries in the neck) cancers; (ii) GI system, covering esophageal, gastro-esophageal, rectal, and anal malignancies; (iii) thoracic system, including lung cancers; and (iv) gynecological system, involving cervical cancers. The exclusion criteria ensured that patients with prior oncological surgery or prior neoadjuvant chemotherapy or radiotherapy were excluded from our study.

2.2. Imaging technique

All patients observed a minimum fasting period of at least 6 h before undergoing PET/CT. To reduce the muscular uptake of FDG, patients were given 5 mg of diazepam (a muscle relaxant) about 30 min before the administration of the radiolabeled drugs. The injected amount of FDG ranged from 185 MBq to 740 MBq, based on the patient's weight (0.15 mCi/kg). Immediately before scanning, patients were instructed to void their bladder. In accordance with the ALARA (as low as reasonably achievable) principle of radiation protection, the facility where the patients rested had limited public access. The average PET/CT acquisition time was between 1.5 and 2 min. Images were acquired in 3D mode, covering from the base of the skull to the mid-femur level, following the staging and metastatic work-up protocol. This procedure was carried out 45 – 50 min after the injection of the radio-labeled drugs, using a hybrid WB-FDG PET/CT Scanner (Discovery 690, General Electric Company, USA), which combines a 64-slice helical CT with a full-ring dedicated PET. The imaging process commenced with a topogram (130 kV and 30 mA), followed by a spiral CT scan (130 kV and 80 – 120 mA), and concluded with an automated PET. The CT images were obtained without the administration of intravenous contrast. A CT-based attenuation correction factor was generated for the PET data, and the images were reconstructed using digital geometrical processing and tomographic reconstruction employing a standard

iterative algorithm (OSEM: accelerated ordered subsets expectation maximization implementations and iterative reconstruction) and reformatted into transaxial, coronal, and sagittal views. Fusion of PET and CT images was achieved using the specialized Siemen's fusion software.

2.3. Outcome parameters

Demographic data (age and gender), clinical data (tumor site and stage), and pathological data (histopathology and grades) were recorded, and the correlation of SUV_{max} to these parameters was analyzed.

2.4. Statistical analysis

Our data were analyzed using the IBM SPSS Version 20 (the Statistical Package for the Social Sciences, International Business Administration Corporation, USA) software. Categorical variables were compared using Pearson's Chi-square test, and correlations were assessed using Spearman's correlation test. The confidence intervals were set at 95%, and $P < 0.05$ was considered statistically significant. The validity of the regression equation was verified, and non-correlated independent variables were selected for the forward stepwise regression model.

3. Results

As illustrated in Figure 1A and B, a total of 117 patients (63 males and 54 females) with a median age of 61 years (range: 21 – 90) were included in the study. The majority of the patients were in the seventh decade of age (33%) followed by the sixth decade (28%). Out of the 117 patients, 29% had metastatic cancers (Figure 1C). Histopathologically, the tumors were classified into three types: squamous cell carcinoma in 71% patients, adenocarcinoma in 24% patients, and small cell cancer in 5% patients.

According to the World Health Organization criteria, tumor differentiation is classified into three histological grades (well, moderate, or poor). In our study, 24 patients had well-differentiated tumors, 53 had moderately-differentiated tumors, and 34 had poorly-differentiated tumors. The actual distribution with respect to various tumor sites, histology, and grades is presented in Tables 1 and 2. The frequency distributions of SUV_{max} for age, gender, sites, histology, and tumor grade are presented in Tables 3 and 4.

Based on Spearman's correlation test, a positive correlation was observed between histology and the SUV_{max}, with *P*-value of 0.01. Likewise, the chi-square test revealed a significant positive correlation between histology and SUV_{max} with *P*-value of 0.024 (Table 5). However, no such association was detected between SUV_{max} and other factors such as age, gender, system, grade, and stage.

The regression model (Equation I) was constructed using grade, age (years), and system.

$$SUV_{max} = 12.728 + (0.33 \times \text{Age [year]}) + (0.158 \times \text{Grade}) - (0.515 \times \text{System}) \quad \text{(I)}$$

This model shows a better predictive value compared to other predictors ($P < 0.05$) (Table 6). In the probability-probability plot, the predicted outcome follows the diagonal line, which fulfills the criteria for normal distribution (Figure 2A), and the predicted values concentrate in a single area similar to the original values (Figure 2B). This model was constructed based on the bragging methodology, which is appropriate for accurate prediction in our study sample.

4. Discussion

Several studies have investigated the relationship between the SUVmax of FDG PET/CT and demographic, clinical,

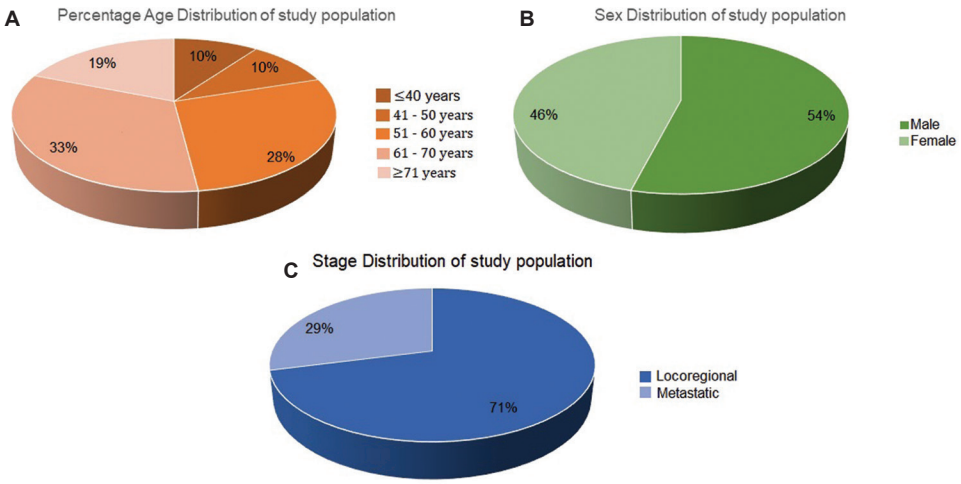

Figure 1. (A) Age, (B) gender, and (C) cancer stage distribution; $n = 117$.

Table 1. Distribution of study population as per organ system, anatomical site, histology, and tumor differentiation grade

Variables	Sites	Histology	Number as per histology	Number as per site	Total number of patients as per system
System					
Gastrointestinal	Esophagus	SCC	18	18	26
	Gastroesophageal junction	Adenocarcinoma	01	01	
	Rectal	Adenocarcinoma	06	06	
	Anal	SCC	01	01	
Gynecological	Cervix	SCC	28	32	32
		Adenocarcinoma	03		
		SCLC	01		
Head and neck	Nasopharynx	SCC	03	17	17
	Oropharynx	SCC	03		
	Hypopharynx	SCC	02		
	Larynx	SCC	04		
	Oral Cavity	SCC	04		
	CUPS Neck	SCC	01		
Thoracic	Lung	SCC	19	42	42
		Adenocarcinoma	18		
		SCLC	05		
Total				117	

Abbreviations: CUPS: Carcinoma of unknown primary with secondaries; SCC: Squamous cell carcinoma; SCLC: Small-cell lung carcinoma.

Table 2. Distribution as tumor differentiation grade in squamous cell carcinoma and adenocarcinoma

Histology	Grades	Number as per grades
Squamous cell carcinoma	WD	18
	MD	45
	PD	20
Adenocarcinoma	WD	06
	MD	08
	PD	14
Total		111

Abbreviations: MD: Moderately-differentiated; PD: Poorly-differentiated; WD: Well-differentiated.

pathological, and tumor-related factors across various cancer sites. The literature does not provide evidence that suggests any significant variation in SUV_{max} values with age or gender. In terms of pathological characteristics, a study on lung cancer revealed a positive correlation between SUV_{max} and tumor size, with squamous cell carcinoma exhibiting significantly higher values compared to other histologies[9]. On the contrary, a separate study found no statistically significant differences between tumor size or degree of differentiation and SUV_{max} in TSCC. However, the reported SUV_{max} was higher among male patients with posterior tumor locations, larger tumor sizes, and lymph node metastasis[8].

Similar to the previous studies, our study primarily aimed to analyze the correlation of various clinicopathological parameters across different cancer sites with SUV_{max}. Interestingly, our findings indicate that only histology demonstrated a significant correlation with SUV_{max}. However, other parameters such as age, gender, system (GI, gynecological, thoracic, or head and neck), grade, and stage showed no statistically significant association with SUV_{max}.

Poorly differentiated tumors are known for their high proliferation rates, theoretically implying a higher uptake of radioactive isotopes. However, the correlation between the SUV_{max} and tumor differentiation remains a topic of controversy. Some studies[10-13] have demonstrated significant connections between SUV_{max} and tumor differentiation. However, in studies conducted by Dylan *et al.*[14] and Chen and Xue Zhen[15], the correlation between grades of tumor differentiation and SUV_{max} was not found to be significant in lung cancer. Moreover, some studies have reported high FDG uptake with a poorer prognosis[16-18], while others have found no association between FDG uptake and overall survival[19,20]. Consequently, FDG uptake is not recommended as a measure for risk stratification neither in the American Joint Committee on Cancer

Table 3. Frequency distribution of age, gender, and sites with the SUVmax

Variables	SUVmax range							
	≤9.00	9.01 – 12.00	12.01 – 15.00	15.01 – 18.00	18.01 – 21.00	21.01 – 24.00	≥24.01	Total
Age group								
≤40	2	5	1	1	1	1	1	12
41 – 50	0	5	2	4	0	1	0	12
51 – 60	5	9	6	8	5	0	0	33
61 – 70	7	11	6	7	5	2	0	38
≥70	2	7	4	1	5	2	1	22
Total	16	37	19	21	16	6	2	117
Gender								
Male	9	24	7	11	8	3	1	63
Female	7	13	12	10	8	3	1	54
Total	16	37	19	21	16	6	2	117
Sites								
Gastrointestinal	4	4	3	9	2	3	1	26
Gynecological	5	8	7	6	6	0	0	32
Thoracic	7	19	4	5	5	1	1	42
Head and neck	0	6	5	1	3	2	0	17
Total	16	37	19	21	16	6	2	117

Abbreviation: SUVmax: Maximum standardized uptake value.

Table 4: Frequency distribution of histology and grades with the SUVmax

Variables	SUVmax range							
	≤9.00	9.01 – 12.00	12.01 – 15.00	15.01 – 18.00	18.01 – 21.00	21.01 – 24.00	≥24.01	Total
Histology								
Adenocarcinoma	9	10	1	5	2	1	0	28
SCC	6	25	18	15	12	5	2	83
SCLC	1	2	0	1	2	0	0	6
Total	16	37	19	21	16	6	2	117
Grade								
WD	2	9	2	4	4	2	1	24
MD	4	16	11	9	9	4	0	53
PD	9	10	6	7	1	0	1	34
SCLC*	1	2	0	1	2	0	0	6
Total	16	37	19	21	16	6	2	117

Note: *SCLC (small cell lung cancer) is generally an aggressive tumor on its own, and no classification in terms of grade is required.
Abbreviations: MD: Moderately differentiated; PD: Poorly differentiated; SCC: Squamous cell carcinoma; SUVmax: Maximum standardized uptake value; WD: Well differentiated.

Staging Manual nor the National Comprehensive Cancer Network guidelines.

In our study, while histology exhibited a significant positive correlation with SUV_{max} – with the highest values observed in squamous cell carcinomas – the tumor grade remained unaffected by the changes in SUV_{max} levels. No discernible trend was observed between the SUV_{max} and different cancer sites. In addition, we could also not find any published study describing an association between SUV_{max} values and the tumor sites.

A notable limitation of our study is the small sample size, coupled with heterogeneity in the numbers of various

Table 5. The relationship between various factors with the SUVmax as indicated by Spearman's correlation and Chi-square test

Factors	SUVmax				
	Correlation value	Pc	Linear association by Chi-square	Pc	Comment
Age group	0.051	0.583	0.258	0.611	Non-significant
Gender	0.094	0.314	0.802	0.370	Non-significant
System	−0.086	0.356	0.871	0.351	Non-significant
Histology	0.237	0.01	5.107	0.024	Significant
Grade	−0.064	0.494	0.028	0.867	Non-significant
Stage	0.048	0.608	0.297	0.586	Non-significant

Note: c is based on normal approximation. $P<0.05$ is statistically significant. Abbreviation: SUVmax: Maximum standardized uptake value.

Table 6. Variables selection and regression analysis factors

Role/function in generalized regression model				
Variables selection for regression equation				
System	Predictor			
Age	Predictor			
Grade	Predictor			
System	Merge categories to maximize association with target			
Age	Trim outliers			
Grade	Merge categories to maximize association with target			
Results of regression analysis				
Variables	**B (coefficient)**	**Standard error**	***T***	***P***
(Constant)	12.728	2.342	5.435	0.000
Age (years)	0.033	0.033	1.017	0.311
Grade	0.158	0.474	0.333	0.739
System	-0.515	0.441	-1.167	0.246

Note: $P<0.05$ is statistically significant.

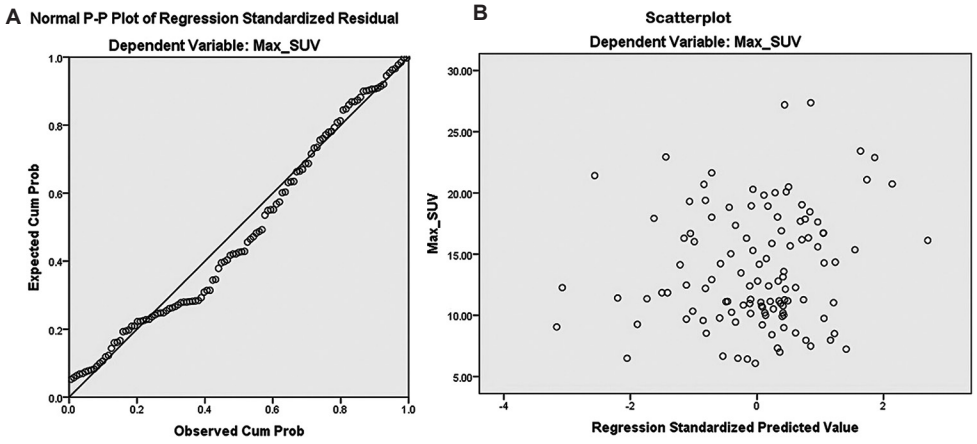

Figure 2. Regression plotted as (A) normal probability-probability plot showing fulfillment of criteria of normal distribution and (B) scatterplot showing the concentration of predicted values on a single area.
Abbreviations: Cum Pro: Cumulative probability; SUV_{max}: Maximum standardized uptake value.

histologies and tumor sites. These limitations hinder the interpretation and generalization of our results. A larger sample size would have increased statistical power and facilitated the application of the boosting method for the

forward stepwise regression model. These suggestions, in turn, could have enhanced the external validity of the constructed model and also the identification of valid predictors. Other limitations of this study include the lack of analysis of factors such as tumor size, which has shown some associations in various studies, along with other factors such as hematological, biochemical, and radiological parameters.

5. Conclusion

Patient's age and gender, as well as locations and stages of their tumors, do not exhibit any particular association with SUV_{max}, and any discernible trends are likely mere coincidences. On the contrary, there exists a potential correlation of SUV_{max} with histology, as evidenced in our study, and with the grade of tumor differentiation, as described in various other studies. Further extensive studies with larger sample sizes are required and recommended to validate this finding.

Acknowledgments

None.

Funding

None.

Conflict of interest

The authors declare that they have no competing interests.

Author contributions

Conceptualization: Nishant Lohia, Sankalp Singh
Formal analysis: Sirshendu Ghosh, Indranil Sinha
Investigation: Abhishek Mahato, Dharmesh Paliwal, Nishant Lohia, Indranil Sinha, Gaurav Trivedi
Methodology: Sankalp Singh, Sirshendu Ghosh
Writing—original draft: Nishant Lohia, Abhishek Mahato
Writing—review & editing: Sankalp Singh, Dharmesh Paliwal

Ethics approval and consent to participate

Ethics approval for the study was obtained from the Institutional Review Board of Command Hospital, Lucknow (IEC/32/19). Written informed consent was obtained from all study participants for their inclusion in the study.

Consent for publication

A written informed consent was obtained from all study participants for the use and publication of their clinical data without any identifying information about the participants.

Availability of data

Supporting data is available from the corresponding author on reasonable request.

References

1. Budak E, Çok G, Akgün A, 2018, The contribution of fluorine 18F FDG PET/CT to lung cancer diagnosis, staging and treatment planning. *Mol Imaging Radionucl Ther*, 27: 73–80.

   https://doi.org/10.4274/mirt.53315

2. Hu Y, Wu D, Tian C, *et al*., 2018, Diagnosis of multiple primary intestinal type adenocarcinoma in the lung by 18F FDG PET/CT. *Clin Nucl Med*, 43: 693–694.

   https://doi.org/10.1097/RLU.0000000000002171

3. Goense L, Ruurda JP, Carter BW, *et al*., 2018, Prediction and diagnosis of interval metastasis after neoadjuvant chemoradiotherapy for oesophageal cancer using 18F FDG PET/CT. *Eur J Nucl Med Mol Imaging*, 45: 1742–17451.

   https://doi.org/10.1007/s00259-018-4011-6

4. Farwell MD, Pryma DA, Mankoff DA, 2014, PET/CT imaging in cancer: Current applications and future directions. *Cancer*, 120: 3433–3445.

   https://doi.org/10.1002/cncr.28860

5. Annunziata S, Cuccaro A, Tisi MC, *et al*., 2018, FDG PET/CT at the end of immuno chemotherapy in follicular lymphoma: The prognostic role of the ratio between target lesion and liver SUVmax (rPET). *Ann Nucl Med*, 32: 372–377.

   https://doi.org/10.1007/s12149-018-1243-2

6. Verhagen AF, Bootsma GP, Tjan-Heijnen VC, *et al*., 2004, FDG-PET in staging lung cancer: How does it change the algorithm? *Lung Cancer*, 44: 175–181.

   https://doi.org/10.1016/j.lungcan.2003.11.007

7. Erdi YE, Macapinlac H, Rosenzweig KE, *et al*., 2000, Use of PET to monitor the response of lung cancer to radiation treatment. *Eur J Nucl Med*, 27: 861–866.

   https://doi.org/10.1007/s002590000258

8. Zheng D, Niu L, Liu W, *et al*., 2019, Relationship between the maximum standardized uptake value of fluoro-2-deoxyglucose-positron emission tomography/computed tomography and clinicopathological characteristics in tongue squamous cell carcinoma. *J Can Res Ther*, 15: 842–848.

   https://doi.org/10.4103/jcrt.JCRT_855_18

9. Sunnetcioglu A, Arısoy A, Demir Y, *et al*., 2015, Associations between the standardized uptake value of (18)F-FDG PET/CT and demographic, clinical, pathological, radiological factors in lung cancer. *Int J Clin Exp Med*, 8: 15794–15800.

10. Liu S, Feng Z, Wen H, *et al*., 2018, ^{18}FFDG PET/CT can predict chemosensitivity and proliferation of epithelial

ovarian cancer via SUVmax value. *Jpn J Radiol*, 36: 544–550.

https://doi.org/10.1007/s11604-018-0755-y

11. Shijun Z, Ning W, Rong Z, *et al*., 2013, Relationship between SUVmax of 18FDG PET and clinicopathological features of nonsmall cell lung cancer. *Chin J Oncol*, 35: 754–757.

12. Nakamura K, Kodama J, Okumura Y, *et al*., 2010, The SUVmax of ^{18}FFDG PET correlates with histological grade in endometrial cancer. *Int J Gynecol Cancer*, 20: 110–115.

https://doi.org/10.1111/IGC.0b013e3181c3a288

13. Kitajima K, Kita M, Suzuki K, *et al*., 2012, Prognostic significance of SUVmax (maximum standardized uptake value) measured by [18F] FDG PET/CT in endometrial cancer. *Eur J Nucl Med Mol Imaging*, 39: 840–845.

https://doi.org/10.1007/s00259-011-2057-9

14. Dylan J, Hazem A, David G, *et al*., 2013, Histological grade/differentiation and ^{18}FFDG PET/CT in oesophageal cancer. *Gastroenterol*, 144: S515–S519.

15. Chen Q, Xue Zhen M, 2009, Relationship between uptake values of ^{18}FFDG PET/CT standard and NSCLC clinicopathological factors. *J Qilu Med*, 24: 104–105.

16. Sasaki R, Komaki R, Macapinlac H, *et al*., 2005, [18F] fluorodeoxyglucose uptake by positron emission tomography predicts outcome of non-small-cell lung cancer. *J Clin Oncol*, 23: 1136–1143.

https://doi.org/10.1200/JCO.2005.06.129

17. Downey RJ, Akhurst T, Gonen M, *et al*., 2007, Fluorine-18 fluorodeoxyglucose positron emission tomographic maximal standardized uptake value predicts survival independent of clinical but not pathologic TNM staging of resected non-small cell lung cancer. *J Thorac Cardiovasc Surg*, 133: 1419–1127.

https://doi.org/0.1016/j.jtcvs.2007.01.041

18. Kwon W, Howard BA, Herndon JE, *et al*., 2015, FDG uptake on positron emission tomography correlates with survival and time to recurrence in patients with stage I non-small-cell lung cancer. *J Thorac Oncol*, 10: 897–902.

https://doi.org/10.1097/JTO.0000000000000534

19. Agarwal M, Brahmanday G, Bajaj SK, *et al*., 2010, Revisiting the prognostic value of preoperative 18F-fluoro-2-deoxyglucose (^{18}F-FDG) positron emission tomography (PET) in early-stage (I and II) non-small cell lung cancers (NSCLC). *Eur J Nucl Med Mol Imaging*, 37: 691–698.

https://doi.org/10.1007/s00259-009-1291-x

20. Hoang JK, Hoagland LF, Coleman RE, *et al*., 2008, Prognostic value of fluorine-18 fluorodeoxyglucose positron emission tomography imaging in patients with advanced-stage non-small-cell lung carcinoma. *J Clin Oncol*, 26: 1459–1464.

https://doi.org/10.1200/JCO.2007.14.3628

ACCSCIENCE PUBLISHING

Advances in Radiotherapy & Nuclear Medicine

MINI-REVIEW

The significance of image fusion in nuclear medicine and molecular imaging

Xiangxing Kong[1,2], Hua Zhu[1,2,3]*, and Zhi Yang[1,2,3]*

[1]Key Laboratory of Carcinogenesis and Translational Research (Ministry of Education/Beijing), NMPA Key Laboratory for Research and Evaluation of Radiopharmaceuticals, Department of Nuclear Medicine, Peking University Cancer Hospital and Institute, Beijing, 100142, China

[2]Institute of Medical Technology, Peking University Health Science Center, Beijing, 100191, China

[3]Institute of Biomedical Engineering, Peking University Shenzhen Graduate School, Shenzhen, Guangdong, 518055, China

Abstract

Nuclear medicine molecular imaging (NMMI) typically employs radioactive isotopes to label cells or molecules and then utilizes imaging devices such as positron emission tomography and single photon emission computed tomography to generate images. However, the images produced by these devices often suffer from problems such as signal noise, low resolution, and poor soft-organ contrast. To address these limitations, image fusion technology merges images from different imaging modalities, combining multiple types of medical image information obtained through various imaging techniques. This process generates a more comprehensive and accurate image, significantly improving image quality, reducing noise, and ultimately enhancing diagnostic accuracy and treatment effectiveness. Image fusion technology has found widespread applications in NMMI, achieving significant results in various fields. This review provides an overview of the development of image fusion technology, introduces traditional image fusion techniques, explores deep learning-based image fusion methods, and finally discusses the challenges and future directions of image fusion technology in NMMI.

Keywords: Nuclear medicine molecular imaging; Image fusion; Multimodal medical image

***Corresponding authors:**
Hua Zhu
(zhuhuananjing@163.com)
Zhi Yang
(pekyz@163.com)

Citation: Kong X, Zhu H and Yang Z, 2023, The significance of image fusion in nuclear medicine and molecular imaging. *Adv Radiother Nucl Med,* 1(2): 0870
https://doi.org/10.36922/arnm.0870

Received: April 27, 2023

Accepted: July 20, 2023

Published Online: August 17, 2023

1. Introduction

Nuclear medicine molecular imaging (NMMI) encompasses the techniques that use radioactive tracers, such as radiolabeled drugs, to study biological molecules and physiological processes. These tracers can be detected and monitored *in vivo* by specific imaging instruments, such as positron emission tomography (PET) and single photon emission computed tomography (SPECT), through changes in absorption, distribution, and metabolism processes. As a non-invasive diagnostic method, NMMI has been widely used to detect the physiological and metabolic processes related to various diseases, providing valuable information for early diagnosis, quantitative evaluation, and treatment monitoring. However, due to factors such as the complex tissue structure, diverse imaging methods, and varying imaging parameters, accurately locating and diagnosing lesions through a single modality medical image are usually impossible.

In addition, the images produced often suffer from problems such as noise, low resolution, and low contrast, which reduce image quality and diagnostic accuracy. In clinical practice, other modality images, such as computed tomography (CT) and magnetic resonance imaging (MRI), are often used to supplement information (Figure S1). To address the challenges mentioned above, image fusion technology aims to merge multiple image data sources into a high-quality image, playing a significant role in disease diagnosis and treatment processes, including monitoring, characterization, and other processes[1]. For instance, recent studies have applied prostate-specific membrane antigen-PET/CT (PSMA PET/CT) image fusion technology to guide biopsies[2]. Image fusion technology has become an essential tool in the field of NMMI for improving image quality and information content[3].

Image fusion technology combines image information from multiple imaging modalities to produce a fused image with improved diagnostic accuracy and visualization. Its development can be traced back to the 1980s[4]. Since then, image fusion technology has rapidly developed in various fields, particularly computer vision, medical imaging, and remote sensing imaging[5]. In the early 1990s, image fusion technology began to be applied in medical imaging. Early image fusion techniques relied on the manual alignment and superimposition of two images. Physicians would visually compare different modalities of nuclear medicine images and manually fuse them. This method is complex, requires significant manual intervention, and is subjective, limiting the reproducibility and accuracy of the resulting images. With the rapid development of computer technology and improvements in hardware equipment, automatic image registration and fusion algorithms have emerged, providing strong support for the advancement of image fusion technology. In recent years, with the rapid development of deep learning technology, deep learning-based image fusion methods have become a research hotspot[6]. These methods use neural network models to learn the relationship between images and generate higher-quality fused images[7]. Traditional and deep learning-based methods differ in several aspects. First, in terms of methodology, traditional methods often rely on predefined rules and handcrafted features for fusion, while deep learning-based methods utilize neural networks to learn and automatically extract features from input images. Second, in feature representation, traditional methods usually focus on low-level features, whereas deep learning-based methods can capture complex and high-level features by learning hierarchical representations. Finally, in regard to adaptability, traditional methods often require manual parameter tuning and adjustment for different imaging modalities, whereas deep learning-based methods, once trained on diverse data, demonstrate better adaptability to different modalities and scenarios.

From January 2010 to March 2023, image fusion technology has made significant progress in NMMI, as shown in Figure 1. The number of publications on molecular imaging and nuclear medicine image fusion has shown sustained growth in recent years (the number of papers was calculated using Web of Science from January 2010 to March 2023, with keywords "medical image fusion," "NMMI," and "medical multimodal image"). Several factors contribute to this growth: (i) Single-modality PET and SPECT images are insufficient to meet the clinical diagnosis needs, necessitating the fusion of other modal images such as CT or MRI to provide additional information; (ii) the continuous improvement in computer hardware performance enables the effective implementation of large-scale image fusion technology; and (iii) ongoing research and refinement of image processing algorithms have led to continuous enhancement in image fusion.

This review provides an overview of the development of image fusion technology, introduces traditional image fusion techniques and deep learning-based image fusion methods, and finally discusses the challenges and future directions of image fusion technology in NMMI.

2. Traditional image fusion methods

Traditional image fusion methods typically involve several steps. First, multiple modal images are acquired from different medical imaging devices. These images are then preprocessed, including denoising, registration, and calibration, to ensure spatial and intensity consistency. Next, an appropriate fusion algorithm is selected to combine the multiple modal images. Finally, the quality and effectiveness of the fusion result are evaluated. Traditional image fusion methods can be mainly categorized into five types: Spatial fusion, frequency fusion, decision-level fusion, hybrid fusion, and sparse representation fusion.

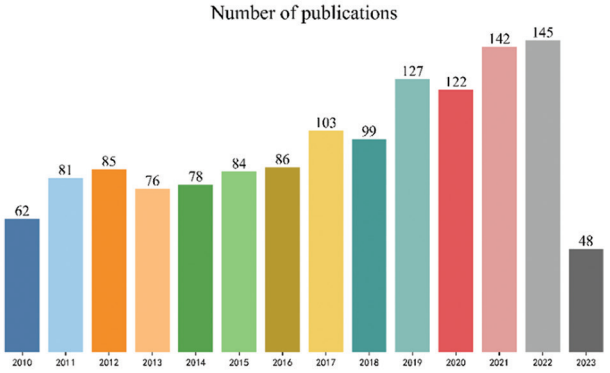

Figure 1. Number of published papers on image fusion in nuclear medicine molecular imaging from January 2010 to March 2023.

Section 2 mainly introduces the application of traditional image fusion methods in the field of NMMI. The studies reporting on the application of traditional image fusion methods in NMMI are provided in Table 1. A comparison of different image fusion methods is provided in Table S1.

2.1. Spatial fusion

Spatial fusion methods mainly rely on pixel-level fusion, directly merging pixels from different images. These methods include simple average, weighted average, maximum value, minimum value, and high-pass filtering[8]. Although these methods are simple and easy to implement, they usually require pre-processing and post-processing and can easily cause spatial distortion in the fused image.

Liu *et al.*[9] proposed a new image fusion method based on a multi-resolution and non-parametric density model. They employed two different fusion rules based on a non-parametric density model and variable weighting theory for the fusion of low-frequency and high-frequency coefficients. The fusion image is constructed by applying the inverse non-subsampled contourlet transform operation to all composite coefficients. Haddadpour *et al.*[10] used MRI and PET as input images and fused them based on the combination of two-dimensional Hilbert transform (2-D HT) and intensity-hue-saturation (IHS) method, which preserves both spatial and spectral features of input images. Stokking *et al.*[11] proposed a hue-saturation-value (HSV) model for fusing anatomical and functional information obtained from MRI and SPECT modes using a color coding scheme. This model outperforms the RGB model and allows for quick, simple, and intuitive retrospective determination of color coding in the fused image. Chen[12]

Table 1. Traditional image fusion methods in NMMI

Authors	Year	Fusion methods	Multimodal images	Fusion Techniques	Organ
Liu *et al.*[9]	2019	Spatial fusion	PET-MRI	Non-parametric density model and variable weighting theory	Brain
Haddadpour *et al.*[10]	2017	Spatial fusion	PET-MRI	Two-dimensional Hilbert transform (2-D HT) and intensity-hue-saturation (IHS) method	Brain
Chen[12]	2017	Spatial fusion	PET-MRI	Combined the IHS model with Log-Gabor transform	Brain
He *et al.*[41]	2010	Spatial fusion	PET-MRI	IHS and principal component analysis (PCA)	Brain
Liu *et al.*[14]	2010	Frequency fusion	PET-CT	Multiwavelet transform	Lung
Xiong *et al.*[42]	2017	Frequency fusion	PET-CT	Shift-invariant Shearlet Transform (SIST) and adaptive Pulse coupled neural network (PCNN)	Brain
Bhavana and Krishnappa[43]	2015	Frequency fusion	PET-MRI	Discrete Wavelet Transform (DWT)	Brain
Wang *et al.*[44]	2006	Frequency fusion	PET-MRI	DWT	Brain
Du *et al.*[45]	2018	Frequency fusion	PET-CT	Parallel significant features	Brain
Shabanzade *et al.*[18]	2019	Decision-level fusion	PET-MRI	Non-parametric Bayesian technique	Brain
Zong and Qiu[20]	2017	sparse representation fusion	SPECT-MRI, PET-CT, MRI-CT	Ssparse representation of classified image patches	Brain, lung
Shahdoosti and Mehrabi[46]	2018	Sparse representation fusion	SPECT-MRI, CT-MRI, PET-MRI	Tetrolet transform	Brain
Zhu *et al.*[21]	2018	Hybrid fusion	PET-MRI, SPECT-MRI	Spatial method for cartoon component and sparse representation method for texture components	Brain
Chaitanya *et al.*[47]	2017	Hybrid fusion	PET-MRI	Shearlet transformation and discrete cosine transform	Brain
Daneshvar and Ghassemian[22]	2010	Hybrid fusion	PET-MRI	IHS and the retina-inspired model (RIM) fusion technique	Brain

Abbreviations: CT: Computed tomography; MRI: Magnetic resonance imaging; PET: Positron emission tomography; SPECT: Single-photon emission computed tomography.

combined the IHS model with Log-Gabor transform and proposed a new method for fusing MRI and PET, using IHS to decompose PET images into three basic features: Hue, saturation, and intensity. This approach effectively preserves the structure and details of the source image and reduces color distortion.

2.2. Frequency fusion

Frequency image fusion methods are based on the principles of Fourier transform. These methods involve transforming images from the spatial domain to the frequency domain. The fusion algorithm is then applied to the transformed images, and the inverse Fourier transform is performed to obtain the synthesized fusion image. Frequency fusion techniques can be further classified into pyramid and transform-based methods[13]. Compared to spatial fusion methods, the frequency fusion method is more complex, but it offers the advantage of reducing the distortion of the fusion image.

Liu *et al.*[14] proposed a medical image fusion algorithm based on multiwavelet transform for PET/CT fusion. The experimental results demonstrated that the fusion image integrates information from the source images, adding more details and texture information and ultimately achieving a good fusion result. Haribabu *et al.*[15] proposed a new approach for PET-MRI image fusion using wavelet and spatial frequency methods. This algorithm addresses the issues of image imbalance and blurred phenomena often encountered infusion images, improving clarity and providing more reference information for medical professionals.

In addition to transform-based methods, the pyramid technique is also commonly used in image fusion. This technique decomposes the original image into multiple scales, fuses the corresponding scales, and then reconstructs to obtain the fused image. During this process, Gaussian pyramid (GP) and Laplacian pyramid (LP) are typically employed for image decomposition and reconstruction. Sahu *et al.*[16] proposed an algorithm that utilizes LP with discrete cosine transformation (DCT). The LP decomposes the input image into different low-pass images, creating a pyramid-like structure. As the pyramid levels increase, the quality of the fusion image improves, thus enhancing the edges and information. In both quantitative and qualitative analyses, this method outperformed Daubechies complex wavelet transform (DCxWT), producing excellent fusion results.

2.3. Decision-level fusion

Decision-level image fusion treats the value of each pixel as a random variable and calculates its probability distribution in each input image. Subsequently, it employs a set of decision rules, such as maximum a posteriori, maximum likelihood, and expectation, to determine the final value of each pixel. The fusion rules of this approach rely on statistical analysis and decision theory, enabling it to fully utilize the information from each input image. As a result, decision-level image fusion improves the quality and robustness of the fusion results[17].

A non-parametric Bayesian technique is considered to learn dictionaries and mappings for two feature spaces[18]. In the proposed method, dictionaries for two feature spaces and the mapping between them are adaptively obtained from input PET and MR images. This algorithm not only learns the dictionaries for each feature space separately but also considers the relation between two feature spaces. This relation helped establish a proper connection between two different input images.

2.4. Sparse representation fusion

Sparse representation fusion combines sparse representation theory and image fusion, making it a highly effective medical image fusion method. The method operates on the assumption that an image can be represented linearly using a small number of atoms (such as the basis vectors in a dictionary). Initially, the input images are decomposed into a set of coefficients, representing linear combinations of the basis vectors in the dictionary. Subsequently, these coefficients are combined to generate fusion coefficients, which produce the fused image. By utilizing only a small subset of the basis vectors, this method excels at preserving the features of the original images while reducing the influence of image distortion and noise[19].

Zong and Qiu[20] developed a new fusion scheme for medical images based on a sparse representation of classified image patches. To achieve this, image patches are first classified according to their geometrical gradient direction. Subsequently, multi-class dictionaries are trained within each class using the online dictionary learning (ODL) algorithm.

2.5. Hybrid fusion

Considering the limitations of traditional image fusion methods, hybrid methods have gained popularity. Hybrid methods involve combining two or more fusion techniques, such as spatial fusion and frequency fusion, to utilize information from different domains and improve the image quality and lesion detection capabilities.

Zhu *et al.*[21] decomposed source multi-modality images into cartoon and texture components. They proposed a proper spatial-based method for preserving morphological

structure in the cartoon components and a sparse-representation-based method for the texture components. Their approach outperformed the state-of-art methods in both visual and quantitative evaluations. Daneshvar and Ghassemian[22] combined the IHS method with the retina-inspired model (RIM) fusion technique, which enabled the preservation of more spatial features and functional information content, respectively. By integrating the advantages of both IHS and RIM fusion methods, their algorithm successfully improved both functional and spatial information content.

3. Deep learning-based image fusion methods

The emergence of deep learning has further advanced the development of image fusion technology. Deep learning-based image fusion method utilizes deep neural network models to learn image features and weights, achieving automatic image fusion. First, multiple modal medical images are input into the deep neural network, which captures key information by extracting and learning features through multiple layers. Subsequently, the extracted features are fused using a fusion layer to generate the fused image. Finally, through training and optimizing the network weights, the fused image achieves the highest quality and information preservation.

Deep learning offers new feature representation methods, addressing the limitations of multiscale and spatial variability present in traditional methods. The main deep learning-based fusion methods include convolutional neural networks (CNN), convolutional sparse representation (CSR), generative adversarial networks (GAN), and deep restricted Boltzmann machines (RBM)[23]. In Section 3, we focus on the application of deep learning-based image fusion methods in the field of NMMI. Table 2 provides an overview of the works that report on the deep learning-based image fusion methods in NMMI.

3.1. CNN-based image fusion

CNN-based image fusion is a common method for medical image fusion. CNNs learn features from raw data, and thus learn different types of image features, ultimately achieving image fusion[24]. In this approach, different types of medical images are first extracted for features through CNNs, resulting in feature representations of different types of images. Then, these feature representations are fused to generate the final fusion image[25]. The flexibility of CNNs allows for the use of different network structures and hyperparameters during the feature extraction process, enabling adaptation to various types of medical images and fusion needs. For example, one can utilize classic CNN structures such as VGG and ResNet, or explore custom network structures and convolutional kernel sizes to achieve more precise feature extraction[26]. In addition, multi-scale feature fusion can be used to fuse feature maps of different scales, thereby enhancing the accuracy and robustness of the fusion image. Alternatively, pixel-level fusion methods can be used to fuse information for each pixel to generate a more refined fusion image. Overall, CNN-based image fusion presents a highly promising image fusion method for achieving more accurate and efficient medical image fusion. Continuous exploration of new network structures, hyperparameters, and fusion methods is essential for further improving its performance[27].

Lahoud and Süsstrunk[28] proposed a real-time image fusion method that utilizes pre-trained neural networks to generate a single image containing features from multi-modal sources. In contrast, Teng *et al.*[29] presented a fusion algorithm based on neuro-fuzzy logic and utilized a hybrid algorithm that combines the back propagation algorithm with the least mean square (LMS) algorithm to train the parameters of the membership function. The fused images based on neuro-fuzzy logic not only reserve more texture features but also enhance the information characteristics of the two original images. Wang *et al.*[30] proposed an algorithm that utilizes a trained Siamese CNN to fuse the pixel activity information of source images, enabling the generation of a weight map. In addition, they implemented a contrast pyramid to decompose the source image.

3.2. CSR-based image fusion

The core idea of CSR-based image fusion technology is to leverage the sparsity of CNN to decompose image features into a set of sparse coefficients and then fuse them by weighted summation. First, CNN is used to extract the features of two images to be fused, and subsequently, the extracted features are decomposed to obtain the sparse coefficients for each feature. For each pixel, the sparse coefficients of the two images are weighted and summed based on their feature weights in the two images, resulting in new sparse coefficients. Finally, these new sparse coefficients are restored into an image to obtain the fused image. CSR-based image fusion technology effectively retains the main features of both images during the fusion process while demonstrating robust detail preservation ability and noise resistance[31].

Liu *et al.*[32] designed a novel diagnostic framework with deep learning architecture to aid the diagnosis of Alzheimer's disease (AD). This framework employs a zero-masking strategy for data fusion, extracting complementary information from multiple data modalities. Compared

Table 2. Deep learning-based image fusion methods in NMMI

Authors	Year	Fusion methods	Multimodal images	Fusion Techniques	Organ
Liu *et al.*[48]	2017	CNN	SPECT-CT, SPECT-MRI, CT-MRI	Siamese convolutional network	Brain
Xu and Ma[49]	2021	CNN	SPECT-MRI, CT-MRI, PET-MRI	An unsupervised enhanced medical image fusion network	Brain
Lahoudand Süsstrunk[28]	2019	CNN	SPECT-MRI, CT-MRI, PET-MRI	A novel strategy based on deep feature maps extracted from a CNN	Brain
Wang *et al.*[30]	2020	CNN	SPECT-MRI	CNN and contrast pyramid	Brain
Liu *et al.*[32]	2015	CSR	PET-MRI	Zero-masking strategy for data fusion	Brain
Xia *et al.*[50]	2020	CSR	SPECT-MRI, CT-MRI, PET-MRI	Parameter-adaptive pulse-coupled neural network (PAPCNN)	Brain
Huang *et al.*[35]	2020	GAN	PET-MRI, SPECT- MRI, SPECT-CT	Multi-generator multi-discriminator conditional GAN (MGMDcGAN)	Brain
Ma *et al.*[51]	2020	GAN	PET-MRI	Dual-discriminator conditional GAN (DDcGAN)	Brain
Kang *et al.* [52]	2020	GAN	PET-MRI	Tissue-aware conditional GAN (TA-cGAN)	Brain
Suk *et al.*[40]	2014	RBM	PET-MRI	MultiModal DBM	Brain

Abbreviations: CNN: Convolutional neural network; CSR: Convolutional sparse representation; CT: Computed tomography; DBM: Deep Boltzmann machine; GAN: Generative adversarial networks; MRI: Magnetic resonance imaging; PET: Positron emission tomography; RBM: Restricted Boltzmann machines; SPECT: Single-photon emission computed tomography.

to previous workflows, this method efficiently fuses multimodal neuroimaging features in a single setting and has the potential to require less labeled data. A research study[31] proposed a CSR-based image fusion framework, where each source image is decomposed into a base layer and a detail layer, facilitating multi-focus image fusion and multimodal image fusion.

3.3. GAN-based image fusion

GAN-based image fusion technology consists of two neural networks: A generator and a discriminator. The generator takes two input images and produces a fused image as an output, while the discriminator's role is to distinguish between the generated fused image and real images[33]. Throughout the training process, the generator continually attempts to generate more realistic fused images to deceive the discriminator, while the discriminator attempts to identify the differences between real and generated images. Through repeated iterations, the generator gradually learns how to generate more realistic fused images[34]. GAN-based image fusion technology excels ingenerating more realistic fused images and demonstrates the ability to adaptively fuse images of varying types and resolutions while preserving the details and features of the original images.

Huang *et al.*[35] proposed a new deep learning-based fusion method for multi-modal medical images with different resolutions, termed multi-generator multi-discriminator conditional GAN (MGMDcGAN). This method enables the simultaneous preservation of functional and structural information, including texture details and dense structure information, without introducing spectral distortion or information loss.

3.4. RBM-based image fusion

RBM-based image fusion technique is an unsupervised learning-based method used for image fusion. It employs two RBMs, with one RBM dedicated to extracting features from the first image and the other from the second image. These two RBMs are interconnected to form a bidirectional image fusion model. The model leverages the energy function of RBMs to minimize the error between the fused image and the original images. When presented with a new input image, the model simultaneously extracts features from both RBMs and fuses them using the energy function[36,37]. The RBM image fusion technique demonstrates good adaptability and generalization ability, allowing it to effectively fuse images of different types and resolutions. Moreover, it preserves the image details, improves image quality, and reduces noise and artifacts[38,39].

Suk *et al.*[40] used deep Boltzmann machine (DBM), a deep network with a restricted Boltzmann machine as a building block, to find a latent hierarchical feature

representation from a 3D patch and then devise a systematic method for joint feature representation from paired patches of MRI and PET using a multimodal DBM.

4. Challenges and future directions of image fusion in nuclear medicine

In summary, both traditional image fusion methods and deep learning-based image fusion methods have shown good performance and are playing an increasingly important role in NMMI. As computer hardware and algorithms continue to evolve, the application prospects of image fusion technology are becoming more and more extensive. However, despite the progress, there are still some challenges and problems in the development of image fusion technology in NMMI. The challenges and future development trends of image fusion in NMMI are discussed in Section 4.

Although image fusion technology has made significant progress in recent years, several challenges and issues still require attention and resolution. First, different types of medical image data may exhibit different levels of noise, distortions, and spatial and temporal resolutions, which may affect the quality and visual effects of the fused data, resulting in distorted or missing information. Ensuring the quality and visual effects of the fusion results should be a top priority in the development of image fusion technology. Second, the heterogeneity of diseases and the complexity of human tissue in clinical work can give rise to different fusion requirements. However, most algorithms lack universality, making it difficult to meet these clinical needs. Ensuring the robustness of the algorithm to different types of images and data is a prerequisite for further development of image fusion technology in NMMI. Third, as medical image fusion involves the sharing and transmission of sensitive medical data, ensuring privacy and security becomes an important challenge. It is essential to address concerns related to data privacy, secure transmission, and storage in medical image fusion. Fourth, medical image fusion algorithms require the processing of large amounts of data and multiple variables, necessitating efficient computing and processing algorithms to ensure accuracy and real-time performance. Improving the speed of image fusion and achieving real-time fusion present additional challenges to image fusion technology. Finally, methods like deep learning rely on substantial data for validation, with publicly available datasets being frequently used to assess robustness and generalizability. However, most of the current multimodal publicly available datasets are centered around brain imaging data. Consequently, research on image fusion methods primarily focuses on brain images, imposing certain requirements for the robustness of other organ sites.

Considering the aforementioned limitations, several future research directions can be envisioned for image fusion technology in NMMI:

(i) As artificial intelligence continues to advance, image fusion technology can be combined with deep learning, neural networks, and other techniques to improve the automation and accuracy of medical image processing.
(ii) The utilization of 3D image fusion technology is expected to expand significantly, providing more accurate medical image information. By effectively evaluating the morphology and structure of organs, 3D medical image fusion technology can contribute to early disease diagnosis and treatment.
(iii) Real-time image fusion technology will be further developed and applied, thereby enhancing medical decision-making during complex procedures, including surgeries. By providing doctors with accurate and real-time medical image information, this innovative technology significantly impacts patient care and treatment outcomes.
(iv) The combination of image fusion technology with big data and cloud computing can significantly improve the speed and efficiency of medical image processing, thus allowing for faster diagnosis and treatment.

5. Conclusion

Medical image fusion technology holds promising prospects in NMMI. By fusing different types of medical image information, it offers more comprehensive and precise medical image information, enabling doctors to make more accurate diagnoses and treatments. Despite the significant progress achieved in medical image fusion technology, there remain challenges and issues that need to be addressed. To further improve the accuracy, efficiency, and reliability of medical image fusion technology, continuous exploration of new algorithms and technologies is imperative. Integrating new technologies such as artificial intelligence, big data, and cloud computing is essential to meet the ever-growing demands in medical imaging and clinical applications.

Acknowledgments

None.

Funding

The research was funded by Beijing Hospitals Authority Dengfeng Project (Grant No.: DFL20191102), the Pilot Project (4th Round) to Reform Public Development of Beijing Municipal Medical Research Institute (2021), and the Third Foster Plan in 2019 "Molecular Imaging Probe

Preparation and Characterization of Key Technologies and Equipment" for the Development of Key Technologies and Equipment in Major Science and Technology Infrastructure in Shenzhen, China.

Conflict of interest

The authors declare no conflicts of interest.

Author contributions

Conceptualization: Xiangxing Kong, Hua Zhu
Writing – original draft: Xiangxing Kong
Writing – review & editing: Hua Zhu, Zhi Yang

Ethics approval and consent to participate

Not applicable.

Consent for publication

Not applicable.

Availability of data

Not applicable.

References

1. Azam MA, Khan KB, Ahmad M, *et al.*, 2021, Multimodal medical image registration and fusion for quality enhancement. *Comput Mater Continua*, 68: 821–840.

   https://doi.org/10.32604/cmc.2021.016131

2. Bodar YJL, Jansen BHE, van der Voorn JP, *et al.*, 2021, Detection of prostate cancer with 18F-DCFPyL PET/CT compared to final histopathology of radical prostatectomy specimens: is PSMA-targeted biopsy feasible? The DeTeCT trial. *World J Urol*, 39: 2439–2446.

   https://doi.org/10.1007/s00345-020-03490-8

3. Azam MA, Khan KB, Salahuddin S, *et al.*, 2022, A review on multimodal medical image fusion: Compendious analysis of medical modalities, multimodal databases, fusion techniques and quality metrics. *Comput Biol Med*, 144: 105253.

   https://doi.org/10.1016/j.compbiomed.2022.105253

4. Huang B, Yang F, Yin M, *et al.*, 2020, A review of multimodal medical image fusion techniques. *Comput Math Methods Med*, 2020: 8279342.

   https://doi.org/10.1155/2020/8279342

5. James AP, Dasarathy BV, 2014, Medical image fusion: A survey of the state of the art. *Inform Fusion*, 19: 4–19.

   https://doi.org/10.1016/j.inffus.2013.12.002

6. LeCun Y, Bengio Y, Hinton G, 2015, Deep learning. *Nature*, 521: 436–444.

   https://doi.org/10.1038/nature14539

7. Zhou T, Ruan S, Canu S, 2019, A review: Deep learning for medical image segmentation using multi-modality fusion. *Array*, 3–4: 100004.

   https://doi.org/10.1016/j.array.2019.100004

8. Li S, Kang X, Fang L, *et al.*, 2017, Pixel-level image fusion: A survey of the state of the art. *Inform Fusion*, 33: 100–112.

   https://doi.org/10.1016/j.inffus.2016.05.004

9. Liu Z, Song Y, Sheng VS, *et al.*, 2019, MRI and PET image fusion using the nonparametric density model and the theory of variable-weight. *Comput Methods Programs Biomed*, 175: 73–82.

   https://doi.org/10.1016/j.cmpb.2019.04.010

10. Haddadpour M, Daneshvar S, Seyedarabi H, 2017, PET and MRI image fusion based on combination of 2-D Hilbert transform and IHS method. *Biomed J*, 40: 219–225.

    https://doi.org/10.1016/j.bj.2017.05.002

11. Stokking R, Zuiderveld KJ, Viergever MA, 2001, Integrated volume visualization of functional image data and anatomical surfaces using normal fusion. *Hum Brain Mapp*, 12: 203–218.

    https://doi.org/10.1002/1097-0193(200104)12:4<203:AID-HBM1016>3.0.CO;2-X

12. Chen CI, 2017, Fusion of PET and MR brain images based on IHS and log-gabor transforms. *IEEE Sens J*, 17: 6995–7010.

    https://doi.org/10.1109/JSEN.2017.2747220

13. Parmar K, Kher R, 2012, A Comparative Analysis of Multimodality Medical Image Fusion Methods. In: Conference: 2012 Sixth Asia Modelling Symposium.

14. Liu Y, Yang J, Sun J, 2010, PET/CT Medical Image Fusion Algorithm Based on Multiwavelet Transform. Vol. 2. In: Conference: Advanced Computer Control (ICACC), 2010 2nd International Conference. p264–268.

15. Haribabu M, Bindu CH, Prasad KS, 2012, Multimodal Medical Image Fusion of MRI-PET Using Wavelet Transform. In: 2012 International Conference on Advances in Mobile Network, Communication and its Applications.

16. Sahu A, Bhateja V, Krishn A, *et al.*, 2014, Medical image fusion with Laplacian Pyramids. In: 2014 International Conference on Medical Imaging, m-Health and Emerging Communication Systems (MedCom).

17. Mahmoudi FT, Samadzadegan F, Reinartz P, 2015, Object recognition based on the context aware decision-level fusion in multiviews imagery. *IEEE J Sel Top Appl Earth Obs Remote Sens*, 8: 12–22.

    https://doi.org/10.1109/JSTARS.2014.2362103

18. Shabanzade F, Khateri M, Liu Z, 2019, MR and PET image fusion using nonparametric bayesian joint dictionary learning. *IEEE Sens Lett*, 3: 1–4.

https://doi.org/10.1109/LSENS.2019.2925072

19. Zhang Q, Liu Y, Blum RS, *et al.*, 2018, Sparse representation based multi-sensor image fusion for multi-focus and multi-modality images: A review. *Inform Fusion*, 40: 57–75.

https://doi.org/10.1016/j.inffus.2017.05.006

20. Zong JJ, Qiu TS, 2017, Medical image fusion based on sparse representation of classified image patches. *Biomed Sig Process Control*, 34: 195–205.

https://doi.org/10.1016/j.bspc.2017.02.005

21. Zhu Z, Yin H, Chai Y, *et al.*, 2018, A novel multi-modality image fusion method based on image decomposition and sparse representation. *Inform Sci*, 432: 516–529.

https://doi.org/10.1016/j.ins.2017.09.010

22. Daneshvar S, Ghassemian H, 2010, MRI and PET image fusion by combining IHS and retina-inspired models. *Inform Fusion*, 11: 114–123.

https://doi.org/10.1016/j.inffus.2009.05.003

23. Liu Z, Cao Y, Li Y, *et al.*, 2020, Automatic diagnosis of fungal keratitis using data augmentation and image fusion with deep convolutional neural network. *Comput Methods Programs Biomed*, 187: 105019.

https://doi.org/10.1016/j.cmpb.2019.105019

24. Li Y, Zhao J, Lv Z, *et al.*, 2021, Multimodal medical supervised image fusion method by CNN. *Front Neurosci*, 15: 638976.

https://doi.org/10.3389/fnins.2021.638976

25. Dian R, Li S, Kang X, 2021, Regularizing hyperspectral and multispectral image fusion by CNN denoiser. *IEEE Trans Neural Netw Learn Syst*, 32: 1124–1135.

https://doi.org/10.1109/TNNLS.2020.2980398

26. Li J, Yuan G, Fan H, 2019, Multifocus image fusion using wavelet-domain-based deep CNN. *Comput Intell Neurosci*, 2019: 4179397.

https://doi.org/10.1155/2019/4179397

27. Liu M, Wang X, Zhang H, 2018, Taxonomy of multi-focal nematode image stacks by a CNN based image fusion approach. *Comput Methods Programs Biomed*, 156: 209–215.

https://doi.org/10.1016/j.cmpb.2018.01.016

28. Lahoud F, Süsstrunk S, 2019, Zero-Learning Fast Medical Image Fusion. In: 2019 22th International Conference on Information Fusion (FUSION).

29. Teng J, Wang S, Zhang J, *et al.*, 2010, Neuro-Fuzzy Logic Based Fusion Algorithm of Medical Images. In: 2010 3rd International Congress on Image and Signal Processing.

30. Wang K, Zheng M, Wei H, *et al.*, 2020, Multi-modality medical image fusion using convolutional neural network and contrast pyramid. *Sensors*, 20, 2169.

https://doi.org/10.3390/s20082169

31. Liu Y, Chen X, Ward RK, *et al.*, 2016, Image fusion with convolutional sparse representation. *IEEE Signal Process Lett*, 23: 1882–1886.

https://doi.org/10.1109/LSP.2016.2618776

32. Liu S, Liu S, Cai W, *et al.*, 2015, Multimodal neuroimaging feature learning for multiclass diagnosis of Alzheimer's disease. *IEEE Trans Biomed Eng*, 62: 1132–1140.

https://doi.org/10.1109/TBME.2014.2372011

33. Zhang H, Yuan J, Tian X, *et al.*, 2021, GAN-FM: Infrared and visible image fusion using GAN with full-scale skip connection and dual markovian discriminators. *IEEE Trans Computat Imaging*, 7: 1134–1147.

https://doi.org/10.1109/TCI.2021.3119954

34. Ma J, Yu W, Liang P, *et al.*, 2019, FusionGAN: A generative adversarial network for infrared and visible image fusion. *Inform Fusion*, 48: 11–26.

https://doi.org/10.1016/j.inffus.2018.09.004

35. Huang J, Le Z, Ma Y, *et al.*, 2020, MGMDcGAN: Medical image fusion using multi-generator multi-discriminator conditional generative adversarial network. *IEEE Access*, 8: 55145–55157.

https://doi.org/10.1109/ACCESS.2020.2982016

36. Lü X, Long L, Deng R, *et al.*, 2022, Image feature extraction based on fuzzy restricted Boltzmann machine. *Measurement*, 204: 112063.

https://doi.org/10.1016/j.measurement.2022.112063

37. Wu W, Qiu Z, Zhao M, *et al.*, 2018, Visible and infrared image fusion using NSST and deep Boltzmann machine. *Optik*, 157: 334–342.

https://doi.org/10.1016/j.ijleo.2017.11.087

38. Sakai Y, Yamanishi K, 2014, Data Fusion Using Restricted Boltzmann Machines. In: 2014 IEEE International Conference on Data Mining.

39. Fakhari A, Kiani K, 2021, A new restricted boltzmann machine training algorithm for image restoration. *Multimedia Tools Appl*, 80: 2047–2062.

https://doi.org/10.1007/s11042-020-09685-w

40. Suk HI, Lee SW, Shen D, 2014, Hierarchical feature representation and multimodal fusion with deep learning for AD/MCI diagnosis. *Neuroimage*, 101: 569–582.

https://doi.org/10.1016/j.neuroimage.2014.06.077

41. He C, Liu Q, Li H, *et al.*, 2010, Multimodal medical image fusion based on IHS and PCA. *Procedia Eng*, 7: 280–285.

https://doi.org/10.1016/j.proeng.2010.11.045

42. Xiong Y, Wu Y, Wang Y, *et al.*, 2017, A Medical Image Fusion Method Based on SIST and Adaptive PCNN. In:

2017 29th Chinese Control and Decision Conference (CCDC).

43. Bhavana V, Krishnappa HK, 2015, Multi-modality medical image fusion using discrete wavelet transform. *Procedia Comput Sci*, 70: 625–631.

https://doi.org/10.1016/j.procs.2015.10.057

44. Wang A, Haijing S, Yueyang G, 2006, The Application of Wavelet Transform to Multi-Modality Medical Image Fusion. In: 2006 IEEE International Conference on Networking, Sensing and Control.

45. Du J, Li W, Xiao B, 2018, Fusion of anatomical and functional images using parallel saliency features. *Inform Sci*, 430–431: 567–576.

https://doi.org/10.1016/j.ins.2017.12.008

46. Shahdoosti HR, Mehrabi A, 2018, Multimodal image fusion using sparse representation classification in tetrolet domain. *Digit Signal Process*, 79: 9–22.

https://doi.org/10.1016/j.dsp.2018.04.002

47. Chaitanya CK, Reddy GS, Bhavana V, *et al.*, 2017, PET and MRI medical image fusion using STDCT and STSVD. In: 2017 International Conference on Computer Communication and Informatics (ICCCI).

48. Liu Y, Chen X, Cheng J, *et al.*, 2017, A Medical Image Fusion Method Based on Convolutional Neural Networks. In: 2017 20th International Conference on Information Fusion (Fusion).

49. Xu H, Ma J, 2021, EMFusion: An unsupervised enhanced medical image fusion network. *Inform Fusion*, 76: 177–186.

https://doi.org/10.1016/j.inffus.2021.06.001

50. Xia J, Lu Y, Tan L, 2020, Research of multimodal medical image fusion based on parameter-adaptive pulse-coupled neural network and convolutional sparse representation. *Comput Math Methods Med*, 2020: 3290136.

https://doi.org/10.1155/2020/3290136

51. Ma J, Xu H, Jiang J, *et al.*, 2020, DDcGAN: A dual-discriminator conditional generative adversarial network for multi-resolution image fusion. *IEEE Trans Image Process*, 29: 4980–4995.

https://doi.org/10.1109/TIP.2020.2977573

52. Kang J, Lu W, Zhang W, 2020, Fusion of brain PET and MRI images using tissue-aware conditional generative adversarial network with joint loss. *IEEE Access*, 8: 6368–6378.

https://doi.org/10.1109/ACCESS.2019.2963741

ACCSCIENCE PUBLISHING

Advances in Radiotherapy & Nuclear Medicine

CASE REPORT

A case of primary pulmonary follicular dendritic cell sarcoma

Min Yang[1], Hongcheng Zhong[2], Xinghua He[3], and Hongjun Jin[1]*

[1]Guangdong Provincial Engineering Research Center of Molecular Imaging, the Fifth Affiliated Hospital, Sun Yat-sen University, Zhuhai, Guangdong Province 519000, China

[2]Thoracic Surgery Department, the Fifth Affiliated Hospital, Sun Yat-sen University, Zhuhai, Guangdong Province 519000, China

[3]Nuclear Medicine Department, the Fifth Affiliated Hospital, Sun Yat-sen University, Zhuhai, Guangdong Province 519000, China

Abstract

Here, we report a 66-year-old woman who presented with an irregular and lobulated pulmonary mass in the apical segment of the right superior lobe with an enlarged mediastinal lymph node. Abdominal computed tomography (CT), brain magnetic resonance imaging, and fluorine-18 fluorodeoxyglucose positron emission tomography/CT scans showed no extrapulmonary distant metastases. The patient underwent surgical sleeve resection of the right superior lobe with systematic hilar and mediastinal lymph node dissection. Post-operative histopathology, including hematoxylin and eosin staining, immunohistochemistry, and Epstein–Barr virus *in situ* hybridization, suggested primary pulmonary follicular dendritic cell sarcoma (FDCS). A follow-up plain chest CT indicated recurrence with multiple metastases of the liver, ribs, and mediastinal lymph nodes 1 year after surgery. The patient declined further therapy and was lost follow-up. In this case, FDCS located in the lung was unusual and rare. Corresponding imaging and histopathological features have enhanced our understanding of this disease. Meanwhile, it is necessary to include this tumor as a differential diagnosis of lung tumors and pay particular attention to the possibility of post-operative recurrence and metastasis. Moreover, considering the heterogeneity of FDCS, it is essential to identify the biological or imaging features that can reflect or predict the high risk of tumor recurrence and metastasis. A corresponding post-operative examination is also necessary to determine if any lesions remain.

Keywords: Pulmonary follicular dendritic cell sarcoma; Lung cancer; Positron emission tomography/computed tomography

***Corresponding author:**
Hongjun Jin
(jinhj3@mail.sysu.edu.cn)

Citation: Yang M, Zhong H, He X, 2023, A case of primary pulmonary follicular dendritic cell sarcoma. *Adv Radiother Nucl Med,* 1(2): 0824
https://doi.org/10.36922/arnm.0824

Received: April 24, 2023

Accepted: June 29, 2023

Published Online: July 13, 2023

1. Background

Follicular dendritic cell sarcoma (FDCS) is a rare low-grade malignant neoplasm that originates from follicular dendritic cells, predominantly involving the lymph nodes[1]. In general, lung involvement typically represents metastatic disease. In this case, we report a rare primary pulmonary FDCS.

2. Case presentation

A 66-year-old woman, who presented with weight loss and intermittent cough with sputum for nearly half a year, underwent a routine physical examination in our hospital. Chest high-resolution computed tomography revealed an irregular and lobulated pulmonary mass in the apical segment of the right superior lobe (longest diameter = 3.8 cm) with bronchial occlusion of the apical segment of the right superior lobe. The mass showed slight enhancement on enhanced computed tomography (CT) scans. The paratracheal lymph nodes (stations 2 and 4) and right hilar lymph nodes (station 10) were significantly enlarged. Abdominal CT and brain magnetic resonance imaging scans showed no obvious abnormalities. Blood routine test showed normal red blood cell count (4.09×10^{12}/L), low hemoglobin (111.0 g/L), high blood platelet count (351.0×10^{9}/L), high white blood cell count (12.99×10^{9}/L), high neutrophil count (10.10×10^{9}/L), high neutrophil percentage (77.70%), normal lymphocyte count (1.83×10^{9}/L), and low lymphocyte percentage (14.10%). Tumor markers examination showed normal levels for progastrin-releasing peptide, cytokeratin 19 fragment, carcinoembryonic antigen, neuron-specific enolase, cancer antigen 15-3, and squamous cell carcinoma antigen.

To clarify the diagnosis, the patient received a CT-guide percutaneous lung puncture biopsy; cytology of the punctured tissue showed a few atypical cells with scattered lymphocytes, plasma cells, and eosinophils. Due to high suspicion of malignancy, the patient received fluorine-18 fluorodeoxyglucose positron emission tomography/CT (^{18}F-FDG PET/CT) scan for further systemic evaluation for distant metastases. The PET maximum intensity projection images (Figure 1A) revealed that there was an avid lesion in the right lung (arrow) with several avid hilar and mediastinal lymph nodes (arrowhead) without distant metastases of other organs. Transversal lung CT, PET, and PET/CT (Figure 1B-D) images showed an irregular-shaped, lobulated, well-defined solitary pulmonary nodule (arrow) measuring 3.8 × 3.6 cm in the right superior lobe. The tumor demonstrated intense FDG uptake (SUV_{mean} = 7.19). For this case, due to involvement in a clinical trial, the patient received a 60-min dynamic ^{18}F-FDG PET/CT scan, and the influx rate constant (K_i) was calculated by applying the ^{18}F-FDG PET dynamic modeling approach known as Patlak graphical analysis[2]. The K_i value of the pulmonary tumor was 0.0428/min (Figure 1F). SUV_{mean} and K_i values of the most avid mediastinal lymph node (arrowhead, station 4) of the same sectional axial PET/CT (Figure 1B-D) were 6.84 and 0.0392/min (Figure 1E and F), respectively. In contrast, the SUV_{mean} and K_i values (SUV_{mean} = 0.45, K_i = 0.0007/min) of the normal lung were much smaller (Figure 1E and F).

The presence of extrapulmonary metastasis of lung cancer is a substantial prognostic determinant with a direct impact on survival because of a variance in the TNM classification, clinical management, and outcome[3]. However, only hilar and mediastinal lymph node metastases of primary lung cancer still have a chance of surgery and a good prognosis. Because malignancy was strongly suspected, considering there was no absolute surgical contraindication (normal cardiopulmonary function and no extrapulmonary metastases), aggressive surgical resection was suggested after discussion. The patient underwent surgical sleeve resection of the right superior lobe for the lesion with hilar and mediastinal lymph node dissection by removing lymph nodes from the upper paratracheal, lower paratracheal, subcarinal, hilar, interlobar, and lobar regions (stations 2, 4, 7, 10, 11 and 12). Photomicrograph revealed ovoid and spindle tumor cells with a diffuse growth pattern (Figure 2A, hematoxylin and eosin [H&E] staining). The cell nucleus was vesicular, and small nucleoli were observed. Cells appeared with plenty of cytoplasm with rare mitotic phases. Infiltration of scattered tumor giant cells, lymphocytes, and plasma cells was observed. The tumor cells were positive for vimentin (Figure 2B) and multifocal positive for CD21 and CD23. Ki-67 staining showed that the proportion of positive tumor cells was about 15% (Figure 2C). The tumor cells were negative for SMA, desmin, calponin, CD34, CD68, S-100, LCA, ALK, CK, CK7, CK5/6, P40, P63, CD56, CgA, and Syn. *In situ* hybridization was negative for Epstein–Barr virus. Moreover, only hilar (station 10) and lobar (station 12) lymph node metastases were found according to the histopathology of all removed lymph node tissue. Histopathology of other lymph nodes (marked stations 2, 4, 7, and 11) only showed the presence of lung tissue. Neither lymph nodes nor tumor tissue was found. These pathological findings (H&E staining, immunohistochemistry, and *in situ* hybridization) were consistent with the manifestations in primary pulmonary FDCS[1]. It was reported that localized FDCS patients who underwent surgery had significantly better overall survival (OS) compared to those who had other treatment modalities, and there was no significant difference between OS of early-staged patients who received adjuvant radiotherapy and surgery alone[1]. In this case, the patient received surgery alone. However, 1 year after surgery, follow-up plain chest CT indicated recurrence with multiple metastases of the liver, ribs, and mediastinal lymph nodes (Figure 3). The patient declined further therapy and was lost follow-up.

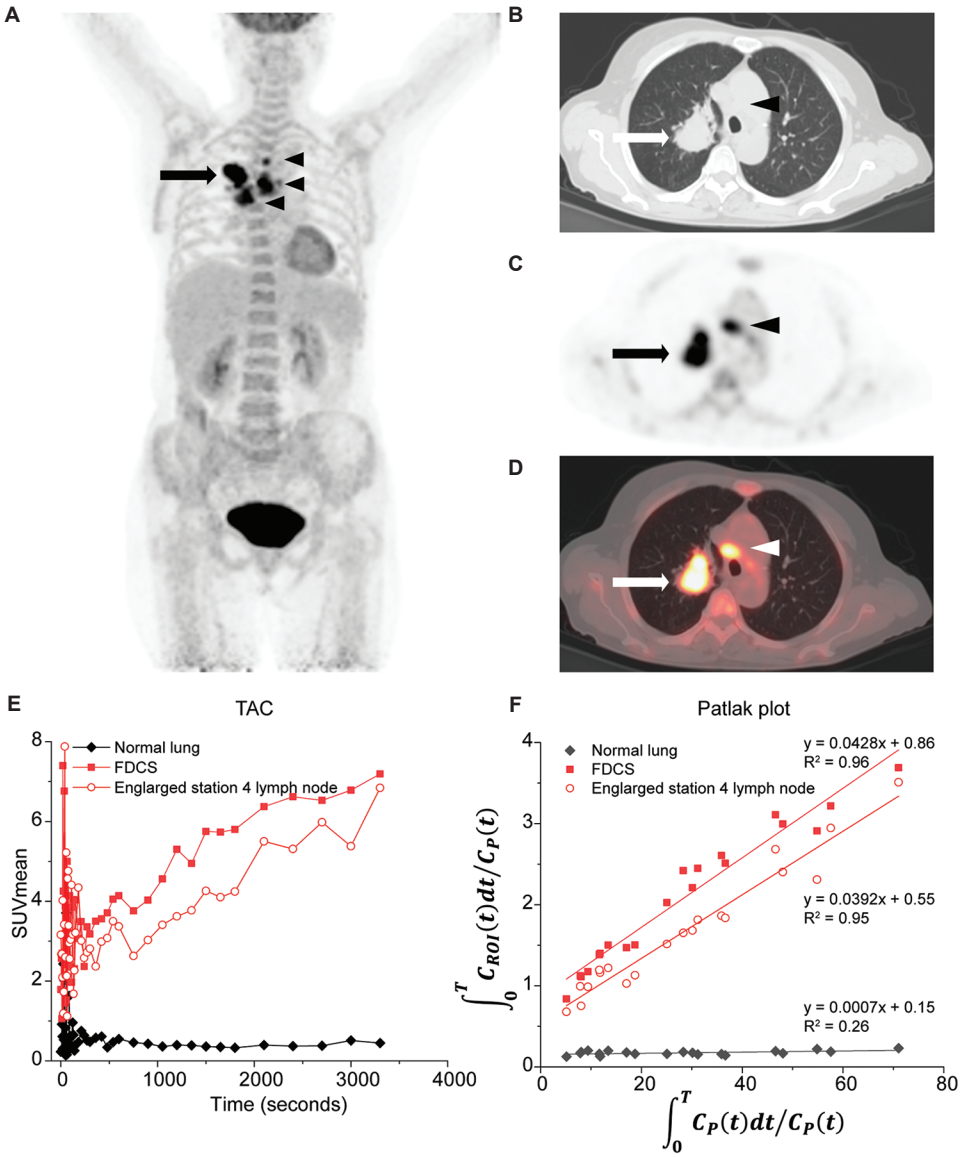

Figure 1. Positron emission tomography/computed tomography (PET/CT) images and analysis. (A) The PET maximum intensity projection images revealed an avid lesion in the right lung (arrow) with several avid hilar and mediastinal lymph nodes (arrowhead) without distant metastases of other organs. Transversal lung CT (B), PET (C), and PET/CT (D) images showed an irregular-shaped solitary pulmonary nodule (arrow) in the right superior lobe. (E) Time activity curve of follicular dendritic cell sarcoma (FDCS) (SUV_{mean} = 7.19), the most avid mediastinal lymph node (station 4, SUV_{mean} = 6.84), and normal lung (SUV_{mean} = 0.45). (F) Patlak plot of the FDCS (K_i = 0.0428/min), the most avid mediastinal lymph node (K_i = 0.0392/min), and normal lung (K_i = 0.0007/min).

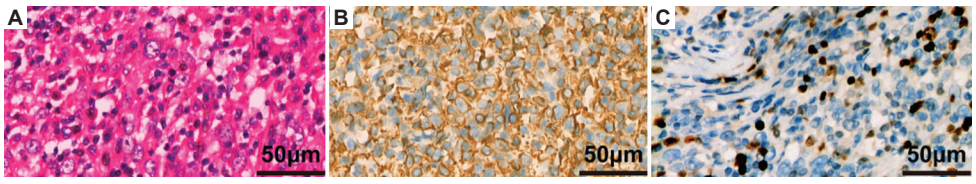

Figure 2. Pathological evidence for follicular dendritic cell sarcoma. (A) Pathology specimen from pulmonary lesion demonstrating typical pathological signs (H&E staining). (B) The tumor cells were positive for vimentin. (C) K_i-67 staining showed that the proportion of positive tumor cells was about 15%. Microscope magnification: ×80.

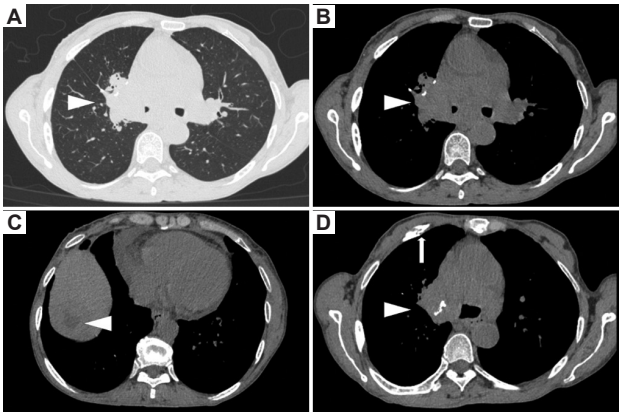

Figure 3. Follow-up plain chest computed tomography (CT) indicated local recurrence and distant metastases 1 year after surgery. (A and B) Lung window and mediastinal window CT images showed local recurrence (arrowhead). (C) Distant metastasis of the liver (arrowhead). (D) Distant metastasis of rib (arrow).

3. Discussion

FDCS, first described by Monda *et al.* in 1986, is a rare low-grade malignant neoplasm that originates from follicular dendritic cells[4]. Histologically, FDCS is characterized as a proliferation of spindle to ovoid cells having indistinct borders with abundant eosinophilic cytoplasm[1]. Besides, nuclei were observed with vesicular or granular chromatin with small distinct nucleoli[1]. The immunohistochemical features of FDCS include positive staining for CD21, CD23, CD35, vimentin, fascin, clusterin, epithelial membrane antigen (EMA), HLA-DR, and D2-40. FDCS predominantly involves the lymph nodes, especially the cervical and axillary lymph nodes[1]. Besides, it can occur in the extranodal areas such as the nasopharynx or oropharynx, tonsils, mediastinum, gastrointestinal tract, breast, pancreas, liver, spleen, mesentery, skin, and palate[1]. The common metastatic sites of FDCS are the liver, lung, lymph nodes, and peritoneum[5]. In general, lung involvement typically represents metastatic disease[1]. Primary pulmonary FDCS, first described in 2001 by Shah *et al.*, was an even rarer occurrence, with only a few cases reported in the literature so far[6-12].

There is no standard treatment regimen for FDCS up to now. In reported primary pulmonary FDCS cases, most cases with the local disease received surgical excision of the tumor with or without post-operative adjuvant therapy such as chemotherapy and radiotherapy[6-12]. The patient of this case underwent surgical excision without any adjuvant therapy. Although some patients remained disease free after surgery[7-9,12], post-operative local recurrence and/or distant metastasis occurred in certain patients after initial treatment[6,8]. For our reported case, local recurrence and distant metastases were found in this patient 1 year after surgery. These cases remind us of the need to develop new treatment strategies and further optimize and standardize the existing treatment strategies for this disease to reduce the risk of post-therapeutic recurrence and metastasis. Simultaneously, considering that post-operative pathological results of lymph nodes (marked stations 2, 4, 7, and 11) showed the presence of lung tissue, the absence of lymph nodes, and tumor tissue, it is possible that the lymph nodes (stations 2 and 4), which showed high uptake on PET images (Figure 1A), were not removed for some specific reasons. It cannot be ruled out that local recurrence and distant metastasis may be caused by unresected lymph nodes. However, proving this connection can be challenging. This highlights the importance of performing corresponding examinations, such as a post-operative PET/CT scan, shortly after surgery to determine whether the lesions are completely removed, thus guiding further treatment.

In this case, FDCS located in the lung was unusual, and the detailed radiological findings and ^{18}F-FDG PET features of this type of tumor were rarely systematically reported. Diagnosis of this rare tumor specifically is difficult based on these non-specific imaging features. Although dynamic ^{18}F-FDG PET/CT was not routinely used in clinical practice, our case revealed that primary tumor and suspected metastatic lesions showed more avid FDG uptake (SUV_{mean}) and higher net uptake rate constant (K_i) than normal lung, which indicated a higher glucose metabolic rate of the primary tumor and suspected metastatic lesions. Comprehensive imaging examination provides us with systematic information about disease invasion and metastasis. Therefore, imaging examinations play a critical role in treatment decisions and clinical management of patients with malignancy. However, the correct diagnosis of this uncommon tumor was mainly based on histological examination at present, whether the Patlak analysis can distinguish lung cancer from FDCS needs further study of large sample cases. New and more specific non-invasive examinations need to be developed for early detection of the disease. Moreover, considering the heterogeneity of FDCS, it is crucial to identify the biological or imaging features that can reflect or predict the high risk of tumor recurrence and metastasis. A corresponding post-operative examination is also necessary to determine if any lesions remain.

4. Conclusion

We share our experience in hopes that corresponding imaging and histopathological features will enhance

the understanding of this disease and aid in accurate diagnoses in clinical settings. Meanwhile, it is important to consider this type of tumor while making differential diagnosis of lung tumors and pay particular attention to the possibility of post-operative recurrence and metastasis.

Acknowledgments

The authors would like to thank Dr. Ying Wang, Dr. Zeqing Xu, Mr. Wenhua Xu, and Mr. Fanwei Zhang from the Nuclear Medicine Department, Dr. Qingdong Cao and Dr. Hua Cheng from the Thoracic Surgery Department of our hospital for their cooperation and technical supports. The authors also thank Dr. Chunlei Han (Turku PET Center, Turku University Hospital, Turku, Finland) for providing technical support with the Carimas software.

Funding

This work was supported by the clinical research IIT project of the Fifth Affiliated Hospital, Sun Yat-sen University (YNZZ2020-01), the National Natural Science Foundation of China (81871382 and 82150610508), the National Key R&D Program of China (2018YFC0910600), grant from the Guangdong Provincial Basic and Applied Basic Research Fund Provincial Enterprise Joint Fund (2021A1515220004), and Starting Fund (310103050303-220904094238) from the Fifth Affiliated Hospital, Sun Yat-sen University.

Conflict of interest

The authors declare that they have no competing interests.

Author contributions

Funding acquisition: Hongjun Jin
Investigation: Min Yang, Hongcheng Zhong, Xinghua He
Resources: Hongjun Jin, Hongcheng Zhong, Xinghua He
Writing – original draft: Min Yang
Writing – review & editing: Hongjun Jin

Ethics approval and consent to participate

This study was approved by the Institutional Review Board of the Fifth Affiliated Hospital, Sun Yat-sen University (approval number: [2018] K04-1, ZDWY.FZYX.002, NCT: 03679936 (http://www.clinicaltrials.gov/). Corresponding written informed consent to participate in the study was obtained from the patient.

Consent for publication

Written informed consent to publish corresponding data or images in the study was obtained from the patient.

Availability of data

The data presented in the study can be obtained from the corresponding author on reasonable request.

References

1. Saygin C, Uzunaslan D, Ozguroglu M, *et al.*, 2013, Dendritic cell sarcoma: A pooled analysis including 462 cases with presentation of our case series. *Crit Rev Oncol Hematol*, 88: 253–271.

   https://doi.org/10.1016/j.critrevonc.2013.05.006

2. Patlak CS, Blasberg RG, Fenstermacher JD, 1983, Graphical evaluation of blood-to-brain transfer constants from multiple-time uptake data. *J Cereb Blood Flow Metab*, 3: 1–7.

   https://doi.org/10.1038/jcbfm.1983.1

3. O'Sullivan B, Brierley J, Byrd D, *et al.*, 2017, The TNM classification of malignant tumours-towards common understanding and reasonable expectations. *Lancet Oncol*, 18: 849–851.

   https://doi.org/10.1016/S1470-2045(17)30438-2

4. Monda L, Warnke R, Rosai J, 1986, A primary lymph node malignancy with features suggestive of dendritic reticulum cell differentiation. A report of 4 cases. *Am J Pathol*, 122: 562–572.

5. Malik A, Veniyoor A, Fanthome B, *et al.*, 2012, Follicular dendritic cell sarcoma: A diagnostic challenge! *J Cancer Res Ther*, 8: 306–307.

   https://doi.org/10.4103/0973-1482.98998

6. Shah RN, Ozden O, Yeldandi A, *et al.*, 2001, Follicular dendritic cell tumor presenting in the lung: A case report. *Hum Pathol*, 32: 745–749.

   https://doi.org/10.1053/hupa.2001.25595

7. Kovacs RB, Sattar HA, Krausz T, *et al.*, 2006, Primary follicular dendritic cell sarcoma of the lung. *Histopathology*, 49: 431–433.

8. Hollingsworth J, Cooper WA, Nicoll KD, *et al.*, 2011, Follicular dendritic cell sarcoma of the lung: A report of two cases highlighting its pathological features and diagnostic pitfalls. *Pathology*, 43: 67–70.

   https://doi.org/10.1097/PAT.0b013e3283419e2a

9. Denning KL, Olson PR, Maley RH Jr., *et al.*, 2009, Primary pulmonary follicular dendritic cell neoplasm: A case report and review of the literature. *Arch Pathol Lab Med*, 133: 643–647.

   https://doi.org/10.5858/133.4.643

10. Kim H, Park CM, Jeon YK, *et al.*, 2012, Computed tomography and 18F-fluoro-2-deoxyglucose positron emission tomography findings of primary pulmonary follicular dendritic cell sarcoma: Case report and a literature review. *J Thorac Imaging*, 27: W94–W96.

https://doi.org/10.1097/RTI.0b013e318220309f

11. Caushi F, Berdica L, Xhemalaj D, *et al*., 2019, Primary pulmonary follicular dendritic cell sarcoma: Successful treatment of an extremely rare case. *J BUON*, 24: 862–863.

12. Garza-Chapa JI, Ocampo-Garza J, Vázquez-Herrera NE, *et al*., 2016, Paraneoplastic pemphigus associated with primary pulmonar follicular dendritic cell sarcoma showing good response to treatment. *J Eur Acad Dermatol Venereol*, 30: 465–467.

https://doi.org/10.1111/jdv.12842

ACCSCIENCE PUBLISHING

Advances in Radiotherapy & Nuclear Medicine

CASE REPORT

Evaluating the efficacy of immunochemoradiotherapy in malignant pleural mesothelioma and distinguishing benign from malignant lymph nodes using ^{18}F-FDG PET/CT and ^{18}F-FAPI-04 PET/CT imaging: A case report

Mengye Peng, Menglu Wang, Ying Zhang, Tingting Wu, and Kezheng Wang*

Department of PET-CT, Harbin Medical University Cancer Hospital, Harbin, China

Abstract

In this paper, we report a case of pleural mesothelioma, imaged employing ^{18}F-fluorodeoxyglucose (FDG) positron emission tomography/computed tomography (PET/CT), and ^{18}F-fibroblast activating protein inhibitor (FAPI)-04 PET/CT. The diagnosis of pleural mesothelioma was confirmed by histopathologically examining the thoracoscopic biopsy. The patient underwent an ^{18}F-FDG PET/CT before immunochemoradiotherapy, followed by an ^{18}F-FAPI-04 imaging 3 months after treatment. The changes in focal anatomy, morphology, and metabolic biology observed between the two distinct PET/CT imaging modalities can aid in distinguishing benign and malignant lymph nodes and assessing treatment efficacy. This case highlights the diagnostic utility of ^{18}F-FDG PET/C in pleural mesothelioma and suggests that ^{18}F-FAPI-04 PET/CT may serve as an effective tool for evaluating the outcomes of immunochemotherapy. Moreover, the combined application of ^{18}F-FDG PET/CT and ^{18}F-FAPI-04 PET/CT holds promise for the differentiation of benign and malignant lymph nodes.

Keywords: ^{18}F-fluorodeoxyglucose; Fibroblast activation protein inhibitor; Malignant mesothelioma; Positron emission tomography/computed tomography; Immunochemoradiotherapy

***Corresponding author:**
Kezheng Wang
(wangkezheng9954001@163.com)

Citation: Peng M, Wang M, Zhang Y, *et al.*, 2023, Evaluating the efficacy of immunochemoradiotherapy in malignant pleural mesothelioma and distinguishing benign from malignant lymph nodes using ^{18}F-FDG PET/CT and ^{18}F-FAPI-04 PET/CT imaging: A case report. *Adv Radiother Nucl Med,* 1(2): 0963
https://doi.org/10.36922/arnm.0963

Received: May 19, 2023

Accepted: September 4, 2023

Published Online: November 7, 2023

1. Background

Malignant pleural mesothelioma is a rare malignant tumor. While the combination of cisplatin and pemetrexed represents the first-line treatment for this condition, emerging evidence suggests the potential benefit of incorporating radiotherapy and immunotherapy in its management. The accurate evaluation of therapeutic efficacy carries significant implications for subsequent clinical decision-making and management. In this case, we present evidence supporting the utilization of ^{18}F-fluorodeoxyglucose (^{18}F-FDG) positron emission tomography/computed tomography (PET/CT) in combination with ^{18}F-fibroblast activating protein inhibitor (FAPI)-04 PET/CT imaging as a promising tool for evaluating the efficacy of immunochemotherapy combined with radiotherapy in pleural mesothelioma. These imaging modalities also exhibited the capacity to

differentiate between benign and malignant lymph nodes, further enhancing their diagnostic utility.

2. Case presentation

A 58-year-old woman who presented with dyspnea came to our hospital for medical consultation and treatment. A series of investigations were conducted on the patient to better comprehend her condition. Chest computed tomography (CT) revealed the presence of pleural effusion and diffused irregular hypertrophy in the left pleura. Subsequent thoracoscopic biopsy confirmed the diagnosis of malignant pleural mesothelioma (epithelial type), as indicated by immunohistochemistry findings: CR(+) (Figure 1A), D2-40(+) (Figure 1B-I), Napsin A(-), and TTF-1(-). Napsin A and TTF-1 are commonly used immunohistochemical markers for the identification of lung adenocarcinoma, while D2-40 is an established immunohistochemical marker crucial for diagnosing

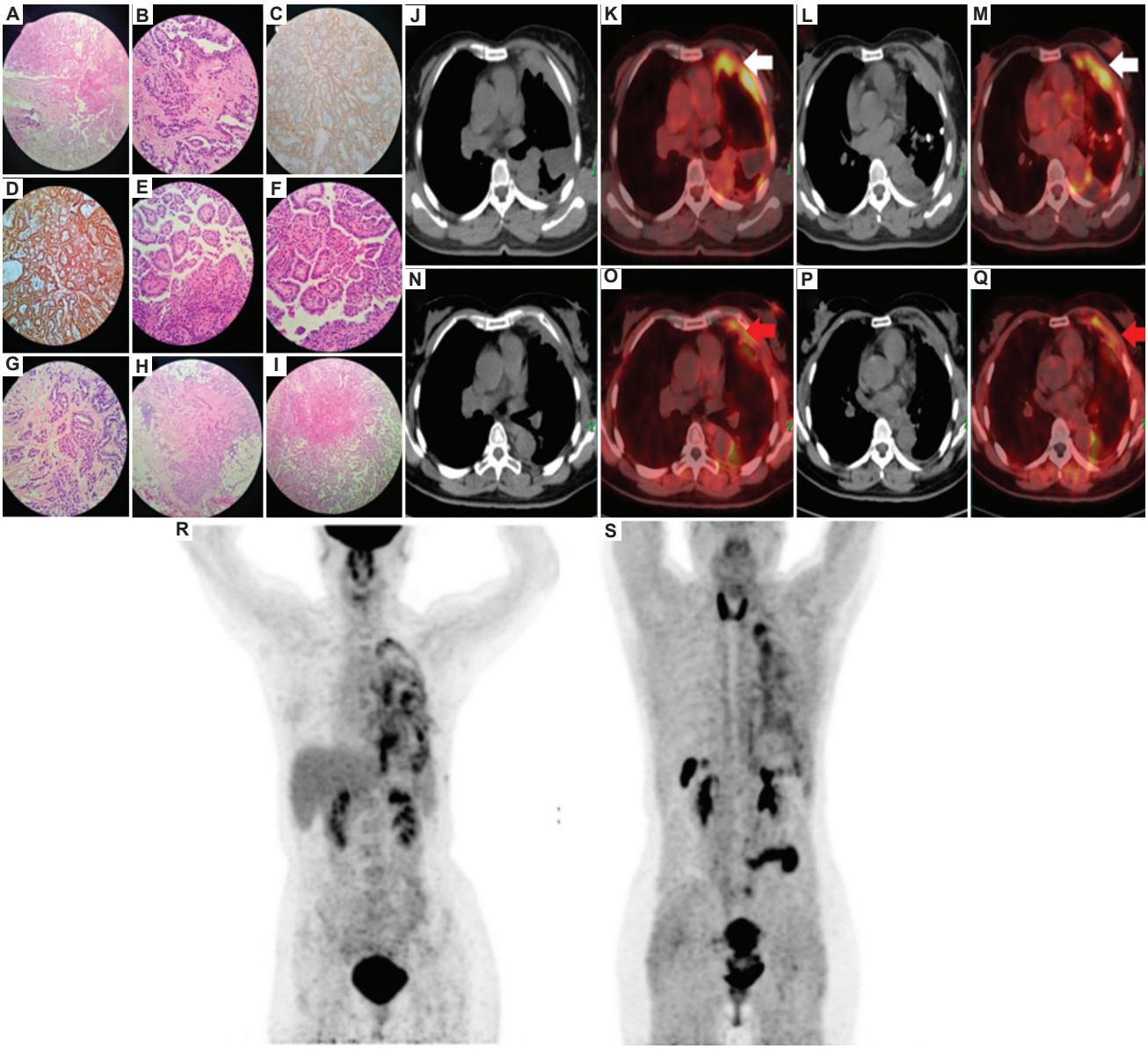

Figure 1. Immunohistochemistry of patient biopsy tissue: (A) CR(+); (B-I) D2-40(+). (J-M) ^{18}F-fluorodeoxyglucose (^{18}F-FDG) positron emission tomography/computed tomography (PET/CT) and CT imaging performed before the treatment shows a left pleural effusion, diffuse thickening of the left pleura, and pathologically increased ^{18}F-FDG accumulation in the left pleura with a maximal standard uptake value (SUVmax) of 6.6. The white arrows indicate lesions before treatment. (N-Q) ^{18}F-fibroblast activating protein inhibitor-04 (^{18}F-FAPI-04) and CT imaging performed after treatment show reduced lesion area and reduced ^{18}F-FAPI-04 accumulation in the left pleura with an SUVmax of 4.96 (tumor-to-background ratio: 3.06). The red arrows indicate the lesions on the same levels after treatment. (R) Maximum intensity projection (MIP) image of ^{18}F-FDG PET/CT. (S) MIP image of ^{18}F-FAPI-04.

epithelioid malignant mesothelioma. D2-40 exhibits a high positive rate in epithelioid mesothelioma and a negative expression in lung adenocarcinoma. The patient underwent ^{18}F-FDG PET/CT imaging before the initiation of treatment. After the imaging, the patient received four cycles of chemotherapy featuring pemetrexed in combination with nedaplatin and camrelizumab, alongside radiotherapy (DT: 5000 cGy/25 f). Three months after completing the treatment, ^{18}F-FAPI-04 PET/CT imaging was performed. ^{18}F-FDG PET/CT images obtained before treatment (Figure 1J-M, R) displayed left pleural effusion, diffuse thickening of the left pleura, and pathologically elevated ^{18}F-FDG accumulation in the left pleura, with a maximal standard uptake value (SUVmax) of 6.6. In contrast, the ^{18}F-FAPI-04 images acquired after treatment (Figure 1N-Q, S) displayed a reduction in lesion area and reduced ^{18}F-FAPI-04 accumulation in the left pleura, now exhibiting an SUVmax of 4.96 (tumor to background ratio: 3.06). These findings suggest that immunochemotherapy and radiotherapy resulted in a reduction in lesion extent and uptake, indicating an effective treatment response.

The ^{18}F-FDG PET/CT images (Figure 2A-F) taken before the patient's treatment revealed the presence of multiple lymph nodes in the bilateral supraclavicular regions, with no observed increased uptake of FDG. In addition, there were no abnormal FDG uptakes observed in the bilateral thyroid lobes. Following treatment, the ^{18}F-FAPI-04 image (Figure 2G-L) displayed no notable changes in the bilateral lymph nodes, with no increased uptake of FAPI-04. However, a marked contrast was observed in the ^{18}F-FAPI-04 PET/CT imaging, which revealed diffuse increased uptake of FAPI-04 in the thyroid region. Thyroid function tests confirmed an increase in levels of antithyroid microsomal antibody and antithyroglobulin antibody. This finding suggests that the elevated FAPI-04 uptake in the thyroid may be attributed to abnormal fibrocyte proliferation and inflammatory changes within the thyroid. Subsequent telephone consultations and CT imaging follow-up data, as of May 29, 2023, indicate process-free survival >17.2 months, local recurrence-free survival >17.2 months, distant metastasis-free survival >17.2 months, and overall survival >17.2 months for the patient. These findings support the effectiveness of immunochemotherapy combined with radiotherapy in the treatment of patients.

3. Discussion

Recent studies have demonstrated that FAPI PET/CT, when compared with FDG PET/CT, may offer certain advantages in the detection of primary tumor and peritoneal metastasis in various malignancies, including gastric cancer, liver cancer, benign non-inflammatory focal liver lesions, differentiated thyroid cancer, as well as lesions in the lymphatic, skeletal, pleural, and pulmonary regions[1-4]. Utilizing ^{68}Ga-FAPI-04, which targets fibroblast activating protein, shows great potential in the diagnosis of a wide range of cancers and sarcomas[5,6]. While CT scans are commonly employed methods for evaluating therapeutic efficacy in cases of malignant pleuroma, they do have inherent limitations[7-11]. Compared with CT, ^{18}F-FDG PET scans can detect metabolic changes at an earlier stage, proving valuable in assessing the treatment response in patients with malignant pleural mesothelioma[12,13]. However, the criteria for evaluating FDG PET scans have not been standardized, and FDG PET tends to exhibit lower sensitivity in the context of low-grade tumors[11,14].

Previous studies have also demonstrated that ^{68}Ga-FAPI PET/CT exhibits a superior capability for detecting primary tumors and lymph node metastases in malignant pleural mesothelioma when compared to ^{18}F-FDG PET, making ^{68}Ga-FAPI PET/CT a promising tool for the evaluation of malignant pleural mesothelioma[4,15-17]. Both

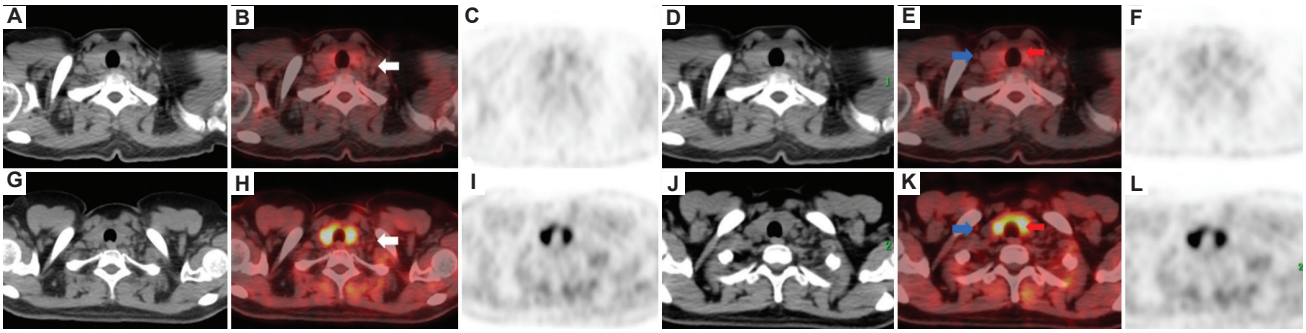

Figure 2. (A-F) ^{18}F-fluorodeoxyglucose (^{18}F-FDG) positron emission tomography/computed tomography images: The white arrows and blue arrows indicate multiple lymph nodes on the bilateral supraclavicular with no increased FDG uptake. The red arrows indicate no abnormal FDG uptake in bilateral thyroid lobes. (G-L) ^{18}F-fibroblast-activating protein inhibitor (FAPI)-04 images: The white arrows and blue arrows indicate the same multiple lymph nodes with no increased FAPI-04 uptake. The red arrows indicate diffuse FAPI-04 uptake in the thyroid (SUV_{max} = 4.86 with tumor-to-background ratio: 3.06).

^{18}F-FAPI-42 and ^{68}Ga-FAPI-04 exhibit similar detection capabilities[18], suggesting that ^{18}F-FAPI-42 holds promise for the detection and evaluation of malignant pleural mesothelioma. However, to our best knowledge, few studies have investigated the use of ^{18}F-FAPI PET/CT in malignant mesothelioma. This study represents the first case of employing ^{18}F-FDG PET/CT and ^{18}F-FAPI-04 PET/CT dual imaging to evaluate the efficacy of immunochemotherapy combined with radiotherapy and to distinguish between benign and malignant lymph nodes in malignant pleural mesothelioma. It is worth noting that although studies have indicated that lymph node metastatic lesions generally exhibit FAPI uptake, some other studies have reported a lack of FAPI uptake in lymph node metastatic lesions after treatment[19]. This suggests the need for caution when identifying this possibility.

4. Conclusion

Our case demonstrates the potential of ^{18}F-FDG PET/CT in the diagnosis of pleural mesothelioma. Furthermore, it suggests that ^{18}F-FAPI-04 PET/CT has the potential to effectively evaluate the effects of immunochemotherapy. Notably, both ^{18}F-FDG PET/CT and ^{18}F-FAPI-04 PET/CT may offer the capability to differentiate between benign and malignant lymph nodes.

Acknowledgments

The authors would like to thank the participating patient, as well as the colleagues and nurses who made this work possible.

Funding

This paper is supported by the National Natural Science Foundation of China General Projects (81571740) (KW); Provincial Key Research and Development Program of Heilongjiang Province (GA21C001) (KW); Postdoctoral Special Scientific Research Grant of Heilongjiang Provincial Government (LBH-Q17104) (KW); Distinguished Young Scientist Funding of Harbin Medical University Affiliated Tumor Hospital (JCQN2019-02); and Key Project of the Climbing Funding of the National Cancer Center (NCC201808B019).

Conflict of interest

The authors report no conflict of interest in this paper.

Author contributions

Conceptualization: Mengye Peng
Methodology: Menglu Wang, Ying Zhang, Tingting Wu
Writing - original draft: Mengye Peng
Writing – review & editing: Kezheng Wang
All authors contributed to the article and approved the submitted version.

Ethics approval and consent to participate

The studies involving human participants were reviewed and approved by the Harbin Medical University Cancer Hospital Medical Ethics Committee. The ethics committee added the requirement of written informed consent for participation.

Consent for publication

The human subjects involved in this article agreed in writing, and we obtained approval to release the data and images.

Availability of data

The datasets generated during and analyzed during the current study are not publicly available due to patient privacy concerns but are available from the corresponding author upon reasonable request.

References

1. Hathi DK, Jones EF, 2019, 68Ga FAPI PET/CT: Tracer uptake in 28 different kinds of cancer. *Radiol Imaging Cancer*, 1: e194003.

   https://doi.org/10.1148/rycan.2019194003

2. Mona CE, Benz MR, Hikmat F, *et al*., 2022, Correlation of 68Ga-FAPi-46 PET biodistribution with FAP expression by immunohistochemistry in patients with solid cancers: Interim analysis of a prospective translational exploratory study. *J Nucl Med*, 63: 1021–1026.

   https://doi.org/10.2967/jnumed.121.262426

3. Giesel FL, Kratochwil C, Schlittenhardt J, *et al*., 2021, Head-to-head intra-individual comparison of biodistribution and tumor uptake of 68Ga-FAPI and 18F-FDG PET/CT in cancer patients. *Eur J Nucl Med Mol Imaging*, 48: 4377–4385.

   https://doi.org/10.1007/s00259-021-05307-1

4. Gundogan C, Guzel Y, Komek H, *et al*., 2022, 68Ga-FAPI-04 PET/CT versus 18F-FDG PET/CT in malignant peritoneal mesothelioma. *Clin Nucl Med*, 47: e113–e115.

   https://doi.org/10.1097/RLU.0000000000003858

5. Kessler L, Ferdinandus J, Hirmas N, *et al*., 2022, 68Ga-FAPI as a diagnostic tool in sarcoma: Data from the 68Ga-FAPI PET prospective observational trial. *J Nucl Med*, 63: 89–95.

   https://doi.org/10.2967/jnumed.121.262096

6. Treglia G, Muoio B, Roustaei H, *et al*., 2021, Head-to-head comparison of fibroblast activation protein inhibitors (FAPI) radiotracers versus [18F]F-FDG in oncology: A systematic review. *Int J Mol Sci*, 22: 11192.

https://doi.org/10.3390/ijms222011192

7. Armato SG 3rd, Labby ZE, Coolen J, *et al*., 2013, Imaging in pleural mesothelioma: A review of the 11th International Conference of the International Mesothelioma Interest Group. *Lung Cancer*, 82: 190–196.

   https://doi.org/10.1016/j.lungcan.2013.08.005

8. Armato SG 3rd, Ogarek JL, Starkey A, *et al*., 2006, Variability in mesothelioma tumor response classification. *AJR Am J Roentgenol*, 186: 1000–1006.

   https://doi.org/10.2214/AJR.05.0076

9. Oxnard GR, Armato SG 3rd, Kindler HL, 2006, Modeling of mesothelioma growth demonstrates weaknesses of current response criteria. *Lung Cancer*, 52: 141–148.

   https://doi.org/10.1016/j.lungcan.2005.12.013

10. Ceresoli GL, Chiti A, Zucali PA, *et al*., 2007, Assessment of tumor response in malignant pleural mesothelioma. *Cancer Treat Rev*, 33: 533–541.

    https://doi.org/10.1016/j.ctrv.2007.07.012

11. Lopci E, Zucali PA, Ceresoli GL, *et al*., 2015, Quantitative analyses at baseline and interim PET evaluation for response assessment and outcome definition in patients with malignant pleural mesothelioma. *Eur J Nucl Med Mol Imaging*, 42: 667–675.

    https://doi.org/10.1007/s00259-014-2960-y

12. Spitilli MG, Treglia G, Calcagni ML, *et al*., 2007, Malignant pleural mesothelioma: Utility of 18 F-FDG PET. *Ann Ital Chir*, 78: 393–396.

13. Sandach P, Seifert R, Fendler WP, *et al*., 2022, A role for PET/CT in response assessment of malignant pleural mesothelioma. *Semin Nucl Med*, 52: 816–823.

    https://doi.org/10.1053/j.semnuclmed.2022.04.008

14. Kitajima K, Doi H, Kuribayashi K, 2016, Present and future roles of FDG-PET/CT imaging in the management of malignant pleural mesothelioma. *Jpn J Radiol*, 34: 537–547.

    https://doi.org/10.1007/s11604-016-0555-1

15. Dong A, Zhao B, Cheng C, *et al*., 2022, 68 Ga-FAPI-04 versus 18 F-FDG PET/CT in detection of epithelioid malignant pleural mesothelioma. *Clin Nucl Med*, 47: 980–981.

    https://doi.org/10.1097/RLU.0000000000004269

16. Li J, Yang J, Hu S, 2023, Malignant peritoneal mesothelioma with butterfly-shaped muscle metastasis: 68Ga-FAPI PET/CT versus 18F-FDG PET/CT. *Clin Nucl Med*, 48: 348–350.

    https://doi.org/10.1097/RLU.0000000000004575

17. Guzel Y, Komek H, Can C, *et al*., 2023, Comparison of the role of 18 F-fluorodeoxyglucose PET/computed tomography and 68 Ga-labeled FAP inhibitor-04 PET/CT in patients with malignant mesothelioma. *Nucl Med Commun*, 44: 631–639.

    https://doi.org/10.1097/MNM.0000000000001702

18. Hu K, Wang L, Wu H, *et al*., 2022, [18F]FAPI-42 PET imaging in cancer patients: Optimal acquisition time, biodistribution, and comparison with [68Ga]Ga-FAPI-04. *Eur J Nucl Med Mol Imaging*, 49: 2833–2843.

    https://doi.org/10.1007/s00259-021-05646-z

19. Shu Q, Deng M, Hu M, *et al*., 2023, The additional role of [68Ga]Ga-FAPI-04 PET/CT in patients with unknown primary lesion with a negative or equivocal [18F]FDG. *Eur J Nucl Med Mol Imaging*, 50: 1442–1452.

    https://doi.org/10.1007/s00259-022-06095-y

Our Journals

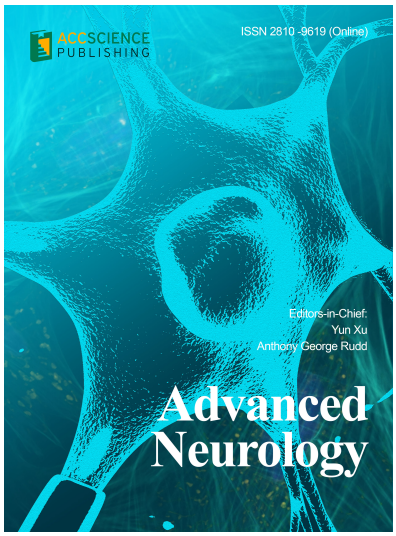

Advanced Neurology is a peer-reviewed and open-access journal that aims to publish and disseminate novel research in the breadth of neurology and neuroscience. The journal aims to advance our understanding in the nervous system and provide a platform to neuroscientists and physicians to showcase their findings in original fundamental and clinical research as well as to present new ideas that highlight the changes in the neurological clinical practice.

Advanced Neurology covers subject areas, including but not limited to the following:

- Neurological disorders
- Neurodegenerative disease
- Cerebrovascular disease
- Epilepsy and movement disorders
- Neuroimmune disease
- Neurological infections
- Muscle disease
- Molecular and cellular neuroscience
- Systems neuroscience
- Cognitive neuroscience
- Computational modeling of nervous system

Global Translational Medicine is a quarterly journal that focuses on medicine, biological sciences, and biomaterials engineering. The goal of *Global Translational Medicine* is to provide a platform to researchers for showcasing their latest research works in translational medicine so as to advance the field towards the betterment of human health. Despite the advancement of omics and new technologies, the process of transforming these technologies and scientific research results into effective therapies and putting them into clinical use still has a long way to go. *Global Translational Medicine* provides a platform to fill the gaps in preclinical and inter-disciplinary research, to promote clinical translation of scientific research results, and to contribute to the conception of new and improved preventive measures as well as diagnostic and therapeutic techniques of diseases.

Global Translational Medicine covers the following themes: cardiovascular disease, metabolism/diabetes/obesity, neuroscience/neurology, cancer, biomaterials and their applications in medicine, proteomics/metabolomics, pharmacogenomics, biomarkers, bioinformatics and data mining, animal and clinical research, and medical methods arising from interdisciplinary crossover.

Start a new journal

Write to us via email if you are interested to start a new journal with AccScience Publishing. Please attach your CV, professional profile page and a brief pitch proposal in your email. We shall inform you of our decision whether we are interested to collaborate in starting a new journal.

Contact: info@accscience.com

https://accscience.com/journal/ARNM

Contact
www.accscience.com
8 Burn Road, #15-03 Trivex, Singapore 369977
Email: editorial@accscience.com
Phone: +65 8182 1586